Unified Gas-kinetic Wave-particle Method for Multiscale Flow Modeling and Computation

by

Yipei CHEN

A Thesis Submitted to
The Hong Kong University of Science and Technology
in Partial Fulfillment of the Requirements for
the Degree of Doctor of Philosophy
in Mathematics

20 December 2021, Hong Kong

Authorization

I hereby declare that I am the sole author of the thesis.

I authorize the University of Science and Technology to lend this thesis to other institutions or individuals for the purpose of scholarly research.

I further authorize the University of Science and Technology to reproduce the thesis by photocopying or by other means, in total or in part, at the request of other institutions or individuals for the purpose of scholarly research.

Yipei CHEN

20 December 2021

Unified Gas-kinetic Wave-particle Method for Multiscale Flow Modeling and Computation

by

Yipei CHEN

This is to certify that I have examined the above PhD thesis
and have found that it is complete and satisfactory in all respects,
and that any and all revisions required by
the thesis examination committee have been made.

Prof. Kun XU, Thesis Supervisor

Prof. Kun XU, Head of Department

Department of Mathematics

20 December 2021

Acknowledgment

First and foremost, I would like to express my deep gratitude to my supervisor, Prof. Kun XU, for his valuable discussion, patient guidance, and constant encouragement in the course of this work. His exceptional taste and pioneer thinking in numerical modeling always inspire me to re-examine the physical compatibility under numerical scheme. In addition, he gives me great freedom to explore the topics I am interested in. It is my fortune to have him being my PhD mentor.

Secondly, I gratefully acknowledge Prof. Yang XIANG, Prof. Tiezheng QIAN, Prof. Wenjing YE, and Prof. Yang LIU to serve in my thesis examination committee and their constructive comments on my thesis. I would also like to thank the Department of Mathematics for providing me with the postgraduate studentship to study here.

Besides, I wish to offer my appreciation to our GKS family and visitors for their stimulating discussion, kindly suggestions throughout my graduate study: Prof. Wenjun SUN, Prof. Jiequan LI, Prof. Zhaoli GUO, Dr. Ruijie WANG, Dr. Weiming LI, Dr. Chang LIU, Dr. Yajun ZHU, Dr. Tianbai XIAO, Dr. Xing JI, Dr. Guiyu CAO, Dr. Ruifeng YUAN, Qing XIE, Fengxiang ZHAO, Wenjin ZHAO, Xiaocong XU, Lu YANG, Xiaojian YANG, Chengxiang LI, Yufeng WEI, Kai HAN, and Yue ZHANG. They aided me in gaining a more comprehensive and in-depth understanding of CFD.

Furthermore, it is my pleasure to thank my fantastic fellow students, who have given me a lot of help in different ways. My thanks also extend to Dr. Dong LIN and Dr. Jiancheng YE, two of my industry colleagues. Their expertise and insight into the world of industrial design substantially enlarged my perspective.

I owe my gratitude to my parents for their educating and unconditional love. I'm

also grateful for my sister's support and care.

Last but not least, I would like to express my heartfelt gratitude to my beloved fiancée Jingming, for her consistent dedication and understanding. Without her, my life would be monochromatic.

Contents

List of Figures

List of Tables

Unified Gas-kinetic Wave-particle Method for Multiscale Flow Modeling and Computation

Yipei CHEN

Department of Mathematics

Abstract

In this thesis, the unified gas-kinetic wave-particle (UGKWP) method for monatomic and diatomic gas flow simulations has been constructed on three-dimensional unstructured mesh with parallel computing capability. The time evolution in the UGKWP method is composed of analytical wave and stochastic particles, where the accumulating effect from particle transport and collision is modeled on the mesh size scale within a time step. With the dynamic wave-particle decomposition, the UGKWP method is able to capture the continuum wave interaction and rarefied particle transport without resolving down to the kinetic scale. Moreover, in UGKWP modeling, translational and rotational non-equilibrium has been taken into consideration.

In addition, UGKWP achieves high efficiency in different flow regimes. With the variation of local cell's Knudsen number, the UGKWP becomes a particle method in the highly rarefied flow regime; in the continuum flow regime, it automatically gets back to macroscopic variables-based flow solver without particles, i.e., the so-called the gas-kinetic scheme (GKS) for the Navier-Stokes solutions. In comparison with the discrete velocity method (DVM)-based unified gas-kinetic scheme (UGKS), the computational cost and memory requirements

in UGKWP could be reduced by several orders of magnitude for high-speed and high-temperature flow simulation.

In the highly rarefied regime, particle transport and collision play a dominant role. Due to the single relaxation time modeling in particle collision term, there is a noticeable discrepancy between the UGKWP solution and the full Boltzmann or DSMC result, especially in the high Mach number and Knudsen number flow. To go beyond the single relaxation model and benefit from the wave-particle decomposition, a heuristic modeling can be directly developed and implemented in UGKWP on the determination of individual particle's collision time according to its velocity. As a result, this direct modeling dramatically improves the accuracy of UGKWP in capturing non-equilibrium transport for both monatomic and diatomic gas flow. There is a perfect agreement between UGKWP and reference solutions in the highly rarefied regime, while the accuracy of UGKWP in the continuum regime is still maintained.

In summary, the UGKWP method has been validated with the reference results and experimental measurements in various cases, from one-dimensional shock structure to three-dimensional flows at different Mach and Knudsen numbers. Thanks to wave-particle formulation, even with a personal workstation, the UGKWP method can be used in simulating three-dimensional multiscale transport with the coexistence of continuum and rarefied flow regimes, particularly for high-speed non-equilibrium flow around a spacecraft in near-space flight.

Chapter 1

Introduction

1.1 Motivation

In the aerospace industry, non-equilibrium gas flow appears in a wide range of applications. For instance, as the space vehicle adjusts its orbit in the outer space, non-equilibrium phenomenon is presented with the large density variation in the thruster plume from the high density gas around the nozzle exit to the near vacuum at far field region [1]. In the re-entry of the vehicle through the upper planetary atmosphere, the high speed of the vehicle generates complicated non-equilibrium aerothermodynamic flow field through the high temperature and highly compressed air at the windward side to the highly expanded region in the leeward side [2]. Another example would be the hypersonic vehicle flying between 20 km and 100 km altitude. Because of the huge altitude change and geometric effect, the localized flow structures surrounding the vehicle, such as shock, rarefaction wave, and wake turbulence, are non-equilibrium in nature during the hypersonic flight [3].

The non-equilibrium flows behave substantially different from the flows in near equilibrium. According to the Knudsen number $\mathrm{Kn} = \ell/L$, which is defined as

the ratio of the particle mean free path ℓ over a characteristic length scale L of the system, the flow regime can be classified into continuum ($\mathrm{Kn} < 0.001$), slip ($0.001 < \mathrm{Kn} < 0.1$), transition ($0.1 < \mathrm{Kn} < 10$), and rarefied ($10 < \mathrm{Kn}$) one [4].

In the continuum regime, the Euler and Navier-Stokes-Fourier (NSF) equations are hydrodynamic equations that are applicable for the description of continuum flow. However, they become less accurate in the near continuum and inaccurate in the transition regimes. On the other hand, the Boltzmann equation [5] models the evolution of the gas distribution function in the kinetic scale of particle mean free path and mean collision time. With the resolution of kinetic scale, the Boltzmann equation is theoretically valid in all flow regimes.

The conventional numerical schemes for non-equilibrium flow simulations target to solve specific governing equations. However, in many engineering applications, multiple flow regimes can co-exist in a single computation, which is either inaccurate or inefficient in the description by single governing equations. For example, for a vehicle in a near-space flight at Mach number 6 (hypersonic) and Reynolds number 5000, the local Knudsen number defined by $\mathrm{Kn}_{local} = \ell|\nabla\rho|/\rho$ can cover a wide range of values with five orders of magnitude difference [6]. Specifically, the multiple flow regimes around the vehicle, such as the high density leading edge and rarefied trailing edge, can co-exist under a single flying condition. To capture such a flow structure, the development of multiscale numerical method for both equilibrium and non-equilibrium flow is required.

1.2 Numerical Methods for Non-equilibrium Gas Dynamics

In general, there are three categories of numerical methods for the simulation of non-equilibrium gas dynamics: deterministic, stochastic and hybrid approaches.

1.2.1 Deterministic Methods

Moment methods are one class of deterministic approaches. Grad's 13 moments (G13) equations [7] are the most famous ones beyond the Navier–Stokes–Fourier equations with Grad closure. By adding terms from higher moments, regularization of Grad's 13 moments (R13) [8] has been conducted. On the basis of Eu's generalized hydrodynamics, Myong et al. adopted nonlinearly coupled constitutive relation (NCCR)[9]. However, the validity of these moment equations is mostly limited to the near continuum flow regime.

On the other hand, the most prevalent deterministic methods are the so-called discrete velocity method (DVM) for the Boltzmann and kinetic equations [10, 11, 12, 13, 14, 15, 16, 17]. Apart from the aforementioned discrete velocity methods developed within finite volume framework, semi-Lagrangian [18, 19] schemes were also developed. Based on the DVM framework, many kinetic solvers are constructed for monatomic and diatomic gases [20, 21]. A comprehensive review can be found in [22].

Theoretically, the non-equilibrium single-species monatomic gas dynamics can be described by the Boltzmann equation. To obtain the numerical solution in all flow regimes, one can always resolve the kinetic scale solution by solving the Boltzmann equation numerically using fast spectral method [23]. However, the high-dimensionality of the equation, nonlinearity of collision term, and its integro-differential nature make the deterministic Boltzmann solver extremely expensive in memory requirement and computational cost.

Apart from the deterministic numerical scheme for the Boltzmann equation, DVM-type schemes for the kinetic model equations have been extensively studied in the last several decades [24, 25, 26, 27, 28, 29, 30]. Due to the complicated collision term in the Boltzmann equation, many kinetic relaxation models have been proposed to simplify the collisional operator of the Boltzmann equation in

the study of rarefied flow, such as the Bhatnagar-Gross-Krook (BGK) model [31], the ellipsoidal statistical BGK (ES-BGK) model [32], and the Shakhov BGK (S-BGK) model [33]. These kinetic equations have been used to develop multiscale methods in all flow regimes.

In terms of numerical software, Nesvetay-3D [24] is an implicit solver on unstructured mesh developed by Titarev et al. with both physical and velocity space decomposed parallelization. Recently, Zhu et al. have implemented discrete unified gas kinetic scheme (DUGKS) [25, 26] for 3D flow computation with the Shakhov collision model [33] in the dugksFoam [34]. Unlike the traditional DVM method, DUGKS is a multiscale scheme, and the time step is not restricted by the particle collision time due to the coupled treatment of particle transport and collision. In addition to the traditional parallel strategy in physical space decomposition, dugksFoam features a parallel computing capability based on velocity space decomposition.

However, many DVM solvers were designed utilizing the operator splitting technique that separate the particle transport and collision. This numerical treatment requires an implicit enforcement that the numerical cell size and time step should be on the physical kinetic scale. To get an accurate solution in the continuum regime, such as the boundary layer solution, the mesh size and time step must be refined and tuned to scale of the particle mean free path and particle collision time, which are particularly expensive in terms of computing cost at a Knudsen number. Also, because the collision operator is stiff in the continuum flow, the time step will be severely constrained [35]. To enhance the computational efficiency, the development of multiscale method for all flow regimes becomes necessary and asymptotic preserving (AP) scheme [36] was proposed with a focus on the hydrodynamic behaviors of a kinetic scheme at the Euler limit. Recently, the concept of unified preserving (UP) [37, 38] has recently been introduced as a generalization of AP that is capable of estimating the higher

order asymptotics, such as the Navier-Stokes limit in the continuum flow regime.

1.2.2 Stochastic Methods

In stochastic methods, discrete particles are employed to model the evolution of the gas distribution function. The stochastic particle approaches, like other Lagrangian-type schemes, can easily maintain the positivity and conservation properties with super stability.

The direct simulation Monte Carlo (DSMC) method [39, 40, 41, 42] is one of the most representative stochastic methods, in which it directly models the particle transport and collision as in the derivation of Boltzmann equation. Instead of solving the complicated collision term in the Boltzmann equation, the direct simulation Monte Carlo (DSMC) mimics the transport and collision process of real gas molecules and achieves great success in the study of high speed and rarefied non-equilibrium gas flow. However, same as many direct Boltzmann solvers, the cell size and time step in DSMC simulation are confined to be less than the particle mean free path and collision time due to the splitting treatment of particle transport and collision. Under such a constraint, the cell size and time step must be diminished,and the computational cost of simulating near continuum flow will rapidly rise. To alleviate the stiffness of the Boltzmann collision term, asymptotic-preserving Monte Carlo methods (AP-DSMC) [43, 44, 45] have recently been presented. AP-DSMC permits the time step to be independent of the mean collision time by mixing sampling from Maxwellian distribution, but it can only recover the Euler limit.

For the low-speed flow simulation, the DSMC method is hampered by statistical noise. Many variants of DSMC, such as information preservation method (IP-DSMC) [46], low-variance deviational simulation Monte Carlo (LVDSMC) method [47], moment-guided Monte Carlo method (MG-DSMC) [48], have been

proposed to attack the noise issue.

Apart from the stochastic particle methods targetting on the solution of full Boltzmann equation, other stochastic particle methods were developed as well for kinetic model equations, such as the stochastic particle method for the Bhatnagar–Gross–Krook (BGK) relaxation model [49, 50], the ellipsoidal statistical BGK (ES-BGK) model [51], and the Fokker-Planck (FP) model [52, 53].

Despite the difficulties encountered by particle methods with the decrease of Knudsen number, the DSMC method is still the mainstream for practical high-speed non-equilibrium flow computation due to its high efficiency. Developed at Sandia National Laboratories, stochastic parallel rarefied-gas time-accurate analyzer (SPARTA) [54] is an open source 2 & 3D DSMC simulator optimized for exascale parallel computing and integrated with both static and dynamic load balancing across processors. Particles in SPARTA advect through a hierarchical oct-tree based Cartesian grid that overlays the simulation box. Additionally, dsmcFoam [55] and its upgrade release dsmcFoam+ [56] have been developed within the framework of OpenFOAM [57, 58, 59], which notably supports dynamic load balancing on arbitrary 2D/3D polyhedron mesh, molecular vibrational and electronic energy modes, chemical reactions, and gravitational force. Other DSMC programs, such as MONACO [60], SMILE [61], DAC [62] with different mesh topologies and collision treatments, can be found in the literature.

1.2.3 Hybrid Methods

In continuum regime, the Navier–Stokes (NS) solver, like GKS [63], is a highly efficient methid because only a few conservative flow variables, like density, momentum, energy, are updated in calculation. In contrast, the particle based direct simulation Monte Carlo method (DSMC) and DVM-type solver may be used for the non-equilibrium flows simulation but its computational cost becomes

unaffordable as the decrease of Knudsen number. Therefore, over the last two decades, hybrid method that can combine the merits of both the efficiency of classical CFD solver and accuracy of kinetic approaches in calculating aerodynamic force and heat under flow conditions with a mixture both continuum and rarefied regimes has attracted much attention.

The hybrid methods can be further classify as Particle-Fluid hybrid methods[64, 65] and Kinetic-Fluid hybrid methods[66, 67]. However, the foregoing hybrid methods required buffer zone to match up kinetic and hydrodynamic solutions, but the information exchange mechanism is artificial and the accuracy inside buffer zone is unclear. As a result, the validity of hybrid methods is closed to the success of buffer zone.

1.3 Direct Modeling and Computation for Multiscale Flow

From previous discussion, it is noticeable that designing numerical algorithms for non-equilibrium flow simulation is typically a tough task due to its multiscale nature. When designing a multiscale scheme, one aims to reach a reasonable compromise between the accuracy in describing the physical reality and computational efficiency, and the following mismatches must be effectively resolved through appropriate modeling with scale variation.

Scale of modeling Mismatch of the physical scale (modeling scale of PDE) and discretized scale (mesh/time scale in numerical simulation)

Degrees of freedom Mismatch between tremendous physical Degrees of freedom (e.g., Loschmidt number $n_0 = 2.687 \times 10^{19}\text{cm}^3$ is the number of gas molecules in cm^3 under standard state) and only a few flow variables in the

macroscopic governing equations, e.g., density, bulk velocity, temperature, etc.

Scale-dependent dynamics/evolution Mismatch of dynamics in the modeling scale, e.g., the transport and collision in mean free path scale, and discretized scale in computation, e.g., a scale with enormous amount of particle collision and free streaming.

The multiscale method has to resolve the above issues with the variation of scales.

1.3.1 Unified Gas-kinetic Scheme (UGKS)

The unified gas-kinetic scheme (UGKS) [16, 68, 69] is a multiscale scheme that has been developed for both rarefied and continuum flow simulation. It adopts the integral solution of the kinetic model equation for the modeling of gas evolution in discretized scale directly. Under the UGKS framework, the numerical flux is constructed by aggregating the effects of particle transport and collision matching to mesh size and time step scale.

After a decade of research and advancement, the UGKS has been successfully extended for the modelings of various multiscale transport phenomena, such as radiative transfer [70], neutron transport [71, 72], multicomponent and multiphase flow [73, 74, 75], and plasma physics [76, 77]. The real gas effects in diatomic gases with rotation and vibration mode were considered in UGKS [78, 79] for the flow study in all regimes.

In the continuum flow regime, the UGKS has an asymptotic limit to the Navier-Stokes (NS) equations without kinetic scale restrictions on time step and cell size, known as the unified preserving (UP) property with order $n = 2$ [37]. Moreover, the adaptive mesh [80, 81], memory reduction [82, 83], implicit and multi-grid [84, 85, 86] techniques have also been incorporated into the UGKS to accelerate

convergence and enhance computational efficiency. A more recent review article can be found in [87].

1.3.2 Unified Gas-kinetic Wave-particle (UGKWP) Method

Deterministic methods like UGKS and DUGKS are accurate in all flow regimes, but almost impractical for aerospace engineering owing to its high memory and computational cost. Stochastic particle methods are highly efficient for high-speed rarefied 3D flow computations, but are difficult to preserve Euler and NS solutions. Therefore, it is attractive to develop a physical-consistent numerical scheme that can have both the advantages of deterministic UGKS and stochastic particle methods.

In order to further increase efficiency and minimize memory cost, the DVM-based gas distribution function in UGKS is replaced by an adaptive formulation of stochastic particle and analytical wave in the newly developed unified gas-kinetic wave-particle (UGKWP) method [88, 89, 90] for monatomic and diatomic gases. UGKWP is extended to other multiscale transport simulations as well, such as radiation [91] and plasma physics [92].

The essential dynamics of UGKWP, like UGKS, is characterized by the integral solution, which is composed of the hydrodynamic wave evolution regulated by the integration of equilibrium state and the kinetic particle free transport emerged from the initial non-equilibrium gas distribution. In UGKWP, the gas particles are divided into hydro-particle, collisional particle, and collisionless particle. Physically, the collisionless particles are mainly employed to represent the non-equilibrium transport, whereas hydro-particles are utilized for equilibration. In UGKWP, the macroscopic flow variables will be updated under a finite volume framework, with both analytical wave and stochastic particles contributing to the cell interface flux.

The computing cost of the UGKWP method is comparable to particle methods in the rarefied regime and hydrodynamic flow solver in the continuum regime, which is one of the distinguishable features of UGKWP method. Specifically, the fraction of particles in UGKWP is proportional to $\exp\left(-1/\mathrm{Kn}_c\right)$, which is a function of the cell Knudsen number. In the continuum flow regime, due to the small cell Knudsen number, the number of particles will be significantly reduced and the UGKWP method automatically converges to the gas-kinetic scheme (GKS) for the Navier-Stokes solutions [63], which has the similar efficiency as a conventional NS solver. In the highly rarefied regime, similar to DSMC, the particle will play a dominant role in the flow evolution with the association of statistical noise.

The UGKWP method can present numerical solution in all flow regimes from the kinetic scale particle free transport to the Navier-Stokes wave propagation without the constraint on the numerical cell size and time step being smaller than the particle mean free path and collision time. Due to the adaptive wave-particle decomposition, the hydrodynamic equilibrium wave evolution and the kinetic non-equilibrium particle free transport within a time step are coupled in the flux evaluation and solution update, which release the numerical cell size and time step in UGKWP from the kinetic scale resolution [35].

In contrast, because particle transport and collision are treated separately, DSMC requires a cell size to be a fraction of the particle mean free path and becomes particularly expensive in the transition and near continuum flow regimes. Moreover, the DSMC method handles the collision process by selecting particle collision pairs. In the low Knudsen number case, intensive collisions have to be dealt with, which makes DSMC impractical in the near continuum flow simulation, such as the flying vehicle at an altitude below 80km. On the other hand, in the continuum flow regime at high Reynolds number, the UGKWP method reverts to the standard Navier-Stokes flow solver with a numerical time step significant

larger than the particle collision time.

In conclusion, the UGKWP is well suited to multiscale flow computations, especially those with the coexistence of both continuum and rarefied flow regimes. For the simulation of hypersonic flow, the steady-state solution can be obtained by averaging the time-accurate evolution solution. The UGKWP method is significantly more efficient than the original DVM-based UGKS due to the use of stochastic particle instead of regular grid discretization in velocity space. Furthermore, with the deployment of particles in UGKWP, the ray effect [93] observed in DVM-type schemes in the highly non-equilibrium zone owing to the inadequate numerical resolution in the particle velocity space can be completely eliminated.

1.4 Objectives and Organization of the Thesis

The main objectives of the current research are the followings:

- Construct UGKWP method in 3D unstructured mesh and validate the scheme for monatomic gas flows;
- Extend the UGKWP method to diatomic molecular flows;
- Improve the accuracy of UGKWP in rarefied flow regime through the construction of particle-velocity dependent collision time.

The thesis is organized as follows:

Chapter 2 starts with a brief introduction of the Boltzmann equation and relaxation model equations. Then, the unified gas-kinetic wave-particle method for single-component monatomic gas is presented on three-dimensional unstructured

mesh. Some numerical examples are provided to validate the multiscale property and efficiency of the method.

Chapter 3 first briefly introduces the properties of diatomic gas and the Rykov relaxation model equation. Next, the UGKWP method is extended to diatomic gas with rotational mode. The asymptotic property of the UGKWP method is investigated and several numerical experiments are conducted to validate the scheme.

Chapter 4 presents a simple comparison between relaxation model equation and Boltzmann equation. Then, the direct modeling on particle collision time in UGKWP framework is conducted. Numerical test cases in rarefied regimes are shown to demonstrate the effectiveness of the new modeling.

Chapter 5 summaries the thesis and discusses the future research directions.

Chapter 2

Unified Gas-kinetic Wave-particle Method for Monatomic Gas Flow

In this chapter, the unified gas-kinetic wave-particle method for monatomic gas flows will be constructed on 3D unstructured mesh with spatial decomposition based parallel computation. The UGKWP program is applicable to 3D flow simulation with complex geometry in all flow regimes.

The organization of the chapter is as follows. The Boltzmann equation and relaxation models are introduced in Section 2.1. In Section 2.2, the numerical procedure of the UGKWP method on unstructured mesh is presented. Section 2.3 covers the construction of 3D UGKWP on parallel framework. In Section 2.4, several numerical examples, including the 3D Sod shock tube inside a square-column, Lid-driven cubic cavity flow, and the high-speed flow around a cube and space vehicle, will be computed to demonstrate the performance of the current algorithm in multiscale flow simulation. Conclusion is given in the last section.

2.1 Boltzmann Equation and Relaxation Models

In the classical kinetic theory [94], the Boltzmann equation for a single-species, monatomic gas without external forces can be written as

$$\frac{\partial f}{\partial t} + \mathbf{u} \cdot \nabla_{\mathbf{x}} f = Q(f, f), \tag{2.1}$$

where $f(t, \mathbf{x}, \mathbf{u})$ is the one-particle gas distribution function of time $t \in \mathbb{R}^+$, physical position $\mathbf{x} \in \mathbb{R}^3$, and particle velocity $\mathbf{u} \in \mathbb{R}^3$.

$Q(f, f)$ is the nonlinear Boltzmann collision operator describing the binary collisions among particles.

$$Q(f, f) = \int_{\mathbb{R}^3} \int_{\mathcal{S}^2} \mathcal{B}(|\mathbf{g}|, \mathbf{\Omega})[f(\mathbf{u}')f(\mathbf{u}'_*) - f(\mathbf{u})f(\mathbf{u}_*)] \, \mathrm{d}\mathbf{\Omega} \, \mathrm{d}\mathbf{u}_*, \tag{2.2}$$

where $\mathcal{B}(|\mathbf{g}|, \mathbf{\Omega}) = |\mathbf{g}|\sigma(|\mathbf{g}|, \mathbf{\Omega}) \geq 0$ is the collision kernel depending on the differential cross-section $\sigma(|\mathbf{g}|, \mathbf{\Omega})$ and the relative velocity of the second particle to the first particle $\mathbf{g} = \mathbf{u}_* - \mathbf{u}$, before encounter in the pre-collision. $\mathbf{\Omega}$ is the direction vector of the post-collision relative velocity $\mathbf{g}' = \mathbf{u}'_* - \mathbf{u}'$ that varying over the unit sphere $\mathcal{S}^2$.

Since the elastic intermolecular collisions conserved the momentum and energy, the pre- and post- collision velocity pairs $(\mathbf{u}, \mathbf{u}_*)$ and $(\mathbf{u}', \mathbf{u}'_*)$ can be expressed as

$$\mathbf{u}' = \frac{\mathbf{u} + \mathbf{u}_*}{2} + \frac{|\mathbf{g}|}{2}\mathbf{\Omega}, \quad \mathbf{u}'_* = \frac{\mathbf{u} + \mathbf{u}_*}{2} - \frac{|\mathbf{g}|}{2}\mathbf{\Omega}. \tag{2.3}$$

From classical scattering theory [95], the differential cross section $\sigma(|\mathbf{g}|, \mathbf{\Omega})$ is defined as

$$\sigma(|\mathbf{g}|, \mathbf{\Omega}) \, \mathrm{d}\mathbf{\Omega} = \sigma(|\mathbf{g}|, \cos\chi) \sin\chi \, \mathrm{d}\chi \, \mathrm{d}\epsilon = -b \, \mathrm{d}b \, \mathrm{d}\epsilon \tag{2.4}$$

where ϵ is the angle that between the collision plane and a reference plane. b called impact parameter is the distance of closest approach of the undisturbed

trajectories.

The scattering angle χ (angle between $\mathbf{g}$ and $\mathbf{g}'$) can be expressed as

$$\cos\chi = \frac{\mathbf{\Omega}\cdot\mathbf{g}}{|\mathbf{g}|}. \tag{2.5}$$

Therefore, given the interaction potential between particles, the specific form of collision kernel $B(|\mathbf{g}|,\mathbf{\Omega}) = B(|\mathbf{g}|,\cos\chi) = |\mathbf{g}|\sigma(|\mathbf{g}|,\cos\chi)$ can be determined from the differential cross-section $\sigma(|\mathbf{g}|,\cos\chi)$

$$\sigma(|\mathbf{g}|,\cos\chi) = \frac{b}{\sin\chi}\left|\frac{\mathrm{d}b}{\mathrm{d}\chi}\right|. \tag{2.6}$$

Due to the difficulty of incorporating inelastic collision such as rotational and vibrational energy exchange, and other non-equilibrium flow physics into the complete collision integral term, which is nonlinear and involve high-dimensional integral, the collision term $Q(f,f)$ is usually simplified by other relaxation-type collision models $S(f)$, such as Bhatnagar-Gross-Krook (BGK) [31], the ellipsoidal statistical BGK (ES-BGK) [96], and the Shakhov model [33]. In general, the kinetic model can be written as

$$\frac{\partial f}{\partial t} + \mathbf{u}\cdot\nabla_{\mathbf{x}} f = S(f). \tag{2.7}$$

Throughout this chapter, the BGK relaxation model

$$f_t + \mathbf{u}\cdot\nabla_{\mathbf{x}} f = \frac{g_{eq} - f}{\tau} \tag{2.8}$$

will be used to construct the UGKWP method. Here τ denotes the relaxation time, which is related to the dynamic viscosity coefficient μ and the pressure p, i.e., $\tau = \mu/p$.

The local equilibrium state g_{eq} is the Maxwellian distribution

$$g_{eq} = \rho\left(\frac{\lambda}{\pi}\right)^{\frac{3+K}{2}} \exp[-\lambda((\mathbf{u}-\mathbf{U})^2 + \boldsymbol{\xi}^2)], \tag{2.9}$$

with density ρ, macroscopic velocity $\mathbf{U}$, internal degree of freedom K ($K = 0$ for monatomic gases), and the internal variable $\boldsymbol{\xi} = (\xi_1, \ldots, \xi_K)$. λ is related to the temperature T by $\lambda = m/(2k_BT) = 1/(2RT)$. Here, m and k_B represent the molecular mass and the Boltzmann constant, respectively. $R = k_B/m$ is the specific gas constant.

Although the BGK model retains all the features of the Boltzmann equation which describes the gas evolution from free molecular motion to the hydrodynamic equilibrium in a statistical way, it yields a unit Prandtl number $\mathrm{Pr} = 1$, while the exact value for a monammic gas is $2/3$. To fix the Prandtl number, the Shakhov model is used when necessary

$$f_t + \mathbf{u} \cdot \nabla_{\mathbf{x}} f = \frac{\tilde{g}_{eq} - f}{\tau}, \tag{2.10}$$

where a modified equilibrium distribution function $\tilde{g}_{eq}$ is obtained through the expansion of g_{eq} in a series of Hermitian polynomials,

$$\tilde{g}_{eq} = g_{eq}\left[1 + \frac{(1-\mathrm{Pr})}{5}\frac{\mathbf{q}\cdot\mathbf{c}}{pRT}\left(\frac{\mathbf{c}^2}{2RT} - \frac{5}{2}\right)\right], \tag{2.11}$$

where $\mathbf{c} = \mathbf{u} - \mathbf{U}$ is the peculiar velocity and $\mathbf{q}$ is the heat flux.

The relaxation parameter in the kinetic model can be calculated through

$$\tau = \frac{\mu}{p} = \frac{\mu_{ref}}{p}\left(\frac{T}{T_{ref}}\right)^{\omega}, \tag{2.12}$$

where μ_{ref}, T_{ref} are the reference viscosity coefficient and temperature, and ω is power index, which is used for recovering the scattering model like Variable Hard Sphere (VHS) or Variable Soft Sphere (VSS) Models [97].

2.2 Unified Gas-kinetic Wave-particle Method for Monoatomic Gas

In this section, the unified gas-kinetic wave-particle (UGKWP) method for monatomic gas will be introduced.

2.2.1 Unified Gas-kinetic Framework

The unified scheme is a direct modeling in the discretized space $\sum_i \Omega_i \subset \mathbb{R}^3$ and time $t^n \in \mathbb{R}^+$ [35]. The cell averaged conservative flow variables $\mathbf{W}_i = (\rho_i, (\rho\mathbf{U})_i, (\rho E)_i)$ on a physical cell Ω_i is defined as

$$\mathbf{W}_i = \frac{1}{|\Omega_i|} \int_{\Omega_i} \mathbf{W}(\mathbf{x})\, \mathrm{d}\mathbf{x}, \tag{2.13}$$

and the cell averaged distribution function f_i on physical cell Ω_i is defined as

$$f_i = \frac{1}{|\Omega_i|} \int_{\Omega_i} f(\mathbf{x})\, \mathrm{d}\mathbf{x}. \tag{2.14}$$

In terms of conservative flow variables, from t^n to t^{n+1} on cell Ω_i, the discretized conservation laws for $\mathbf{W}_i$ and f_i are

$$\mathbf{W}_i^{n+1} = \mathbf{W}_i^n - \frac{1}{|\Omega_i|} \sum_{j \in N(i)} \mathbf{F}_{ij} |S_{ij}|, \tag{2.15}$$

and

$$f_i^{n+1} = f_i^n - \frac{1}{|\Omega_i|} \sum_{j \in N(i)} \mathcal{F}_{ij} |S_{ij}| + \int_{t^n}^{t^{n+1}} S(f_i)\, \mathrm{d}t, \tag{2.16}$$

where $|\Omega_i|$ is the volume of cell i and set $N(i)$ contains all the interface-adjacent neighboring cells' index of cell i. $\mathbf{F}_{ij}$ and $\mathcal{F}_{ij}$ denote the macroscopic and microscopic fluxes across the interface ij between cells i and j, respectively. $|S_{ij}|$ is referred to the area of the interface ij. $\Delta t = t^{n+1} - t^n$ is the discretized time step.

It should be noted that Eqs. (2.15) and (2.16) are the fundamental conservation laws on the scale of mesh size and time step. Its physical evolution of macroscopic flow variables and microscopic gas distribution function are determined by the macroscopic and microscopic fluxes $\mathbf{F}_{ij}$ and $\mathcal{F}_{ij}$, respectively. The macroscopic conservative flow variables, their fluxes, and the flux for the particle transport are related to the moments of the gas distribution function through

$$\mathbf{W}_i = \int f_i \boldsymbol{\psi} \, \mathrm{d}\Xi, \tag{2.17}$$

$$\mathbf{F}_{ij} = \int_{t^n}^{t^{n+1}} \int \mathbf{u} \cdot \mathbf{n}_{ij} f_{ij}(t) \boldsymbol{\psi} \, \mathrm{d}\Xi \, \mathrm{d}t, \tag{2.18}$$

and

$$\mathcal{F}_{ij} = \int_{t^n}^{t^{n+1}} \mathbf{u} \cdot \mathbf{n}_{ij} f_{ij}(t) \, \mathrm{d}t, \tag{2.19}$$

where $\mathbf{n}_{ij}$ is the unit normal vector of the interface ij pointing from cell i to cell j and $f_{ij}(t)$ is the time-dependent distribution function on the cell interface. $\boldsymbol{\psi} = (1, \mathbf{u}, \frac{1}{2}(\mathbf{u}^2 + \boldsymbol{\xi}^2))$ is the collision invariants and $\mathrm{d}\Xi = \mathrm{d}\mathbf{u} \, \mathrm{d}\boldsymbol{\xi}$, $\mathrm{d}\mathbf{u} = \mathrm{d}u \, \mathrm{d}v \, \mathrm{d}w$, and $\mathrm{d}\boldsymbol{\xi} = \mathrm{d}\xi_1 \, \mathrm{d}\xi_2 \cdots \mathrm{d}\xi_K$.

The BGK/Shakhov relaxation term satisfies the compatibility condition

$$\int S(f) \boldsymbol{\psi} \, \mathrm{d}\Xi = \int \frac{g_{eq} - f}{\tau} \boldsymbol{\psi} \, \mathrm{d}\Xi = \int \frac{\tilde{g}_{eq} - f}{\tau} \boldsymbol{\psi} \, \mathrm{d}\Xi = \mathbf{0} \tag{2.20}$$

for the mass, momentum, and energy conservations during the particle collision process.

2.2.2 Interface Flux Evalutaion

The multiscale flow evolution in the unified algorithm relies on the construction of the flux function at the cell interfaces. The time-dependent gas distribution function $f_{ij}(t)$ with coupled particle free streaming and collision determines the flow physics in different regime. The integral solution of the BGK model is

$$f(t, \mathbf{x}_0, \mathbf{u}) = \frac{1}{\tau} \int_{t_0}^{t} g(t, \mathbf{x}', \mathbf{u}) e^{-(t-t')/\tau} \, \mathrm{d}t' + e^{-(t-t_0)/\tau} f_0(\mathbf{x}_0 - \mathbf{u}(t - t_0), \mathbf{u}), \tag{2.21}$$

where $\mathbf{x}_0$ is the point for the evaluation of the local gas distribution function, $\mathbf{x}' = \mathbf{x}_0 - \mathbf{u}(t - t')$ is the particle trajectory. Typically, $\mathbf{x}_0$ is denoted as the center of a cell interface $\mathbf{x}_{ij}$ for flux evaluation. $g(t, \mathbf{x}, \mathbf{u})$ is the equilibrium state distributed ($g = g_{eq}$ for BGK model, $g = \tilde{g}_{eq}$ for Shakhov model) and $f_0(\mathbf{x})$ is the initial distribution function around $\mathbf{x}_0$ at the beginning of each step $t_0 = t^n$.

Specifically, for second-order accuracy, without loss of generality, we can set $t_0 = 0$, $\mathbf{x} = \mathbf{0}$ and the local expansions of the gas distribution functions are

$$g(t, \mathbf{x}, \mathbf{u}) = g + \nabla_{\mathbf{x}} g \cdot \mathbf{x} + \partial_t g \, t, \tag{2.22}$$

and

$$f_0(\mathbf{x}, \mathbf{u}) = f_0 + \nabla_{\mathbf{x}} f \cdot \mathbf{x}. \tag{2.23}$$

The time-dependent distribution function at $\mathbf{x}_{ij}$ can be obtained as

$$f_{ij}(t) = \underbrace{c_1 g + c_2 \nabla_{\mathbf{x}} g \cdot \mathbf{u} + c_3 \partial_t g}_{f_{ij}^{eq}(t)} + \underbrace{c_4 f_0 + c_5 \nabla_{\mathbf{x}} f \cdot \mathbf{u}}_{f_{ij}^{fr}(t)}, \tag{2.24}$$

with the coefficients

$$\begin{aligned} c_1 &= 1 - e^{-t/\tau}, \\ c_2 &= t e^{-t/\tau} - \tau(1 - e^{-t/\tau}), \\ c_3 &= t - \tau(1 - e^{-t/\tau}), \\ c_4 &= e^{-t/\tau}, \\ c_5 &= -t e^{-t/\tau}. \end{aligned} \tag{2.25}$$

Note that $f_{ij}^{eq}(t)$ and $f_{ij}^{fr}(t)$ are the terms related to the evolution of the local equilibrium state $g(\mathbf{x}, t)$ and the initial distribution function $f_0(\mathbf{x})$, respectively.

The initial gas distribution function f_0 at a cell interface in Eq. (2.24) is reconstructed from the updated gas distribution function at t^n, which has the form

$$f_0(\mathbf{x}_{ij}) = \begin{cases} f_i^n + (\nabla_{\mathbf{x}} f)_i^n \cdot (\mathbf{x}_{ij} - \mathbf{x}_i), & \mathbf{n}_{ij} \cdot \mathbf{u} \geq 0, \\ f_j^n + (\nabla_{\mathbf{x}} f)_j^n \cdot (\mathbf{x}_{ij} - \mathbf{x}_j), & \mathbf{n}_{ij} \cdot \mathbf{u} < 0, \end{cases} \tag{2.26}$$

where f_i^n and f_j^n are the initial distribution functions at neighboring cells around the cell interface ij. Here $(\nabla_{\mathbf{x}} f)_i^n$ is the spatial gradient of the initial distribution function inside the cell i and can be reconstructed via least square with Venkatakrishnan's limiter [98] or Barth and Jespersen limiter [99].

The local equilibrium state g in Eq. (2.24) is computed from the compatibility condition

$$\mathbf{W} = \int g\boldsymbol{\psi}\,\mathrm{d}\Xi = \int f_0\boldsymbol{\psi}\,\mathrm{d}\Xi, \tag{2.27}$$

and the gradient of conservative variables can be obtained through the micro-macro relationship

$$\nabla_{\mathbf{x}}\mathbf{W} = \int \nabla_{\mathbf{x}} g \otimes \boldsymbol{\psi}\,\mathrm{d}\Xi = \int \nabla_{\mathbf{x}} f \otimes \boldsymbol{\psi}\,\mathrm{d}\Xi, \tag{2.28}$$

and the temporal derivatives of conservative variables are determined by the conservative requirements on the first order Chapman-Enskog expansion [5],

$$\mathbf{W}_t = \int \partial_t g\boldsymbol{\psi}\,\mathrm{d}\Xi = -\int \mathbf{u}\cdot\nabla_{\mathbf{x}} g\boldsymbol{\psi}\,\mathrm{d}\Xi. \tag{2.29}$$

Equations (2.21) and (2.24) present a transition from the initial non-equilibrium to the equilibrium state with the increment of particle collision. It shows an evolution process from the kinetic to the hydrodynamic scale, and the real solution depends on the local parameter $\tau/\Delta t$, i.e., the local cell Knudsen number.

Specifically, the microscopic flux transport over a time step gives

$$\begin{aligned}\mathcal{F}_{ij} &= \int_0^{\Delta t} \mathbf{u}\cdot\mathbf{n}_{ij} f_{ij}(t)\,\mathrm{d}t \\ &= \underbrace{\mathbf{u}\cdot\mathbf{n}_{ij}(q_1 g + q_2\nabla_{\mathbf{x}} g\cdot\mathbf{u} + q_3\partial_t g)}_{\mathcal{F}_{ij}^{eq}} + \underbrace{\mathbf{u}\cdot\mathbf{n}_{ij}(q_4 f_0 + q_5\nabla_{\mathbf{x}} f\cdot\mathbf{u})}_{\mathcal{F}_{ij}^{fr}},\end{aligned} \tag{2.30}$$

where $\mathcal{F}_{ij}^{eq}$ and $\mathcal{F}_{ij}^{fr}$ are the equilibrium microscopic flux and the free transport microscopic flux, respectively. Similarly, the macroscopic fluxes for conservative variables are splitting into the equilibrium macroscopic flux $\mathbf{F}_{ij}^{eq}$ and the free

streaming macroscopic flux $\mathbf{F}_{ij}^{fr}$

$$\mathbf{F}_{ij} = \int_0^{\Delta t} \int \mathbf{u} \cdot \mathbf{n}_{ij} f_{ij}(t) \boldsymbol{\psi} \, \mathrm{d}\Xi \, \mathrm{d}t = \underbrace{\int \mathcal{F}_{ij}^{eq} \boldsymbol{\psi} \, \mathrm{d}\Xi}_{\mathbf{F}_{ij}^{eq}} + \underbrace{\int \mathcal{F}_{ij}^{fr} \boldsymbol{\psi} \, \mathrm{d}\Xi}_{\mathbf{F}_{ij}^{fr}}, \tag{2.31}$$

with the coefficients

$$\begin{aligned} q_1 &= \Delta t - \tau(1 - e^{-\Delta t/\tau}), \\ q_2 &= 2\tau^2(1 - e^{-\Delta t/\tau}) - \tau\Delta t - \tau\Delta t e^{-\Delta t/\tau}, \\ q_3 &= \frac{\Delta t^2}{2} - \tau\Delta t + \tau^2(1 - e^{-\Delta t/\tau}), \\ q_4 &= \tau(1 - e^{-\Delta t/\tau}), \\ q_5 &= \tau\Delta t e^{-\Delta t/\tau} - \tau^2(1 - e^{-\Delta t/\tau}). \end{aligned} \tag{2.32}$$

With the variation of $\tau/\Delta t$, Eqs. (2.30) and (2.31) can provide multiscale flow evolution solution. When $\Delta t \gg \tau$, only the terms $\mathcal{F}_{ij}^{eq}$ with $q_1 \approx \Delta t$ and $q_3 \approx \Delta t^2/2$ are remained on account of intensive particle collisions; when $\Delta t \ll \tau$, only the terms related to non-equilibrium particle free transport $\mathcal{F}_{ij}^{fr}$ with $q_4 \approx \Delta t$ and $q_5 \approx -\Delta t^2/2$ are kept.

In deterministic UGKS [16], the cell averaged distribution function f_i is further discretized in the particle velocity space with discrete velocity points $\mathbf{u}_k$ to capture the non-equilibrium distribution function. Compared with many other DVM with separate particle free-streaming and collision, the mesh size and time step in UGKS are not limited by the particle mean free path and collision time due to their coupled evolution solution for the flux evaluation. Moreover, the NS solutions can be obtained automatically by UGKS in the continuum regime even with $\Delta t \gg \tau$, such as in the laminar boundary layer solution resolved by a few grid points at high Reynolds number.

For UGKWP, instead of discretizing the particle velocity space with discrited velocity points, both kinetic particles and hydrodynamic wave will be coupled together to represent the non-equilibrium gas distribution function.

2.2.3 Particle Evolution

The particle dynamics in UGKWP method is to track particle trajectory until the collision happens. Once the particle collides with other particles, it will be merged into the macroscopic flow quantities, and get re-sampled from the updated macroscopic flow variables at the beginning of the next time step.

The integral solution of the kinetic model equation (2.21) can be rewritten as

$$f(t,\mathbf{x},\mathbf{u}) = (1-e^{-t/\tau})g^h(t,\mathbf{x},\mathbf{u}) + e^{-t/\tau}f_0(\mathbf{x}-\mathbf{u}t,\mathbf{u}), \tag{2.33}$$

where

$$g^h = g + \left(\frac{te^{-t/\tau}}{1-e^{-t/\tau}} - \tau\right)\mathbf{u}\cdot\nabla_{\mathbf{x}}g + \left(\frac{t}{1-e^{-t/\tau}} - \tau\right)\partial_t g. \tag{2.34}$$

Equation (2.33) states that the distribution function at time t is a combination of the initial distribution function f_0 and the modified equilibrium state g^h. In the perspective of particles' dynamics, it means that the simulation particle has a probability of $e^{-t/\tau}$ to free stream, and has a probability of $(1-e^{-t/\tau})$ to collide with other particle and the post-collision particle distribution follows the **hydrodynamic distribution** g^h.

The time for the free streaming to stop and follow the distribution g^h is called the first collision time or particle free streaming time t^f. Its cumulative distribution function is

$$\mathscr{F}(t) = \mathbb{P}(t^f \le t) = 1 - e^{-t/\tau}. \tag{2.35}$$

A particle $P_k(m_k, \mathbf{x}_k, \mathbf{u}_k, e_k, t_k^f)$ can be represented by its mass m_k, position $\mathbf{x}_k$, velocity $\mathbf{u}_k$, and internal energy e_k. Its free transport time is

$$t^f = \min(-\tau\ln(\eta), \Delta t), \tag{2.36}$$

where η is a random number generated from a uniform distribution on the interval $(0,1)$, i.e., $\eta \sim U(0,1)$. Remind that the min in Eq. (2.36) is to ensure t^f is the

free streaming time of the particle within the current time step, but not the total free stream time of the particle.

Moreover, the particle P_k keeps free transport for a time period of t^f and its location $\mathbf{x}^*$ right before its first collision can be accurately tracked,

$$\mathbf{x}_k^* = \mathbf{x}_k^n + \mathbf{u}_k t^f, \tag{2.37}$$

where the particle velocity $\mathbf{u}_k$ keeps the same value.

In a numerical time step from t^n to t^{n+1}, all simulating particles can be categorized into two groups according to the time t^f assigned to each particle. The particles with $t^f = \Delta t$ are called **collisionless particles** P^f, and the particles with $t^f < \Delta t$ are called **collisional particles** P^c.

- For the collisionless particle P_k^f, its trajectory is fully tracked during the whole time step.
- For collisional particle P_k^c, the particle trajectory is tracked till t^f. Then the particle's mass, momentum, and energy are merged into the macroscopic quantities in that cell and the simulation particle gets eliminated.

Those eliminated particles will get re-sampled from hydrodynamic distribution g^h once the updated macroscopic quantities $\mathbf{W}^{n+1}$ are obtained. i.e.,

$$\mathbf{u}_k^{n+1} \sim g^h(\mathbf{W}_i^{n+1}). \tag{2.38}$$

And the re-sampled particles are defined as **hydro-particle** P^h. The macroscopic quantities corresponding to the hydro-particles are defined as **hydrodynamic wave** $\mathbf{W}^h$.

The position of the re-sampled particle $\mathbf{x}_k^{n+1}$ is uniformly distributed inside the cell Ω_i where the collision happens.

$$\mathbf{x}_k^{n+1} \sim U(\Omega_i) \tag{2.39}$$

Similarly to the DSMC method, the internal energy e_k^{n+1} is sampled according to the temperature and internal degree of freedom K. The particles mass m_k can be prescribed and will be discussed later.

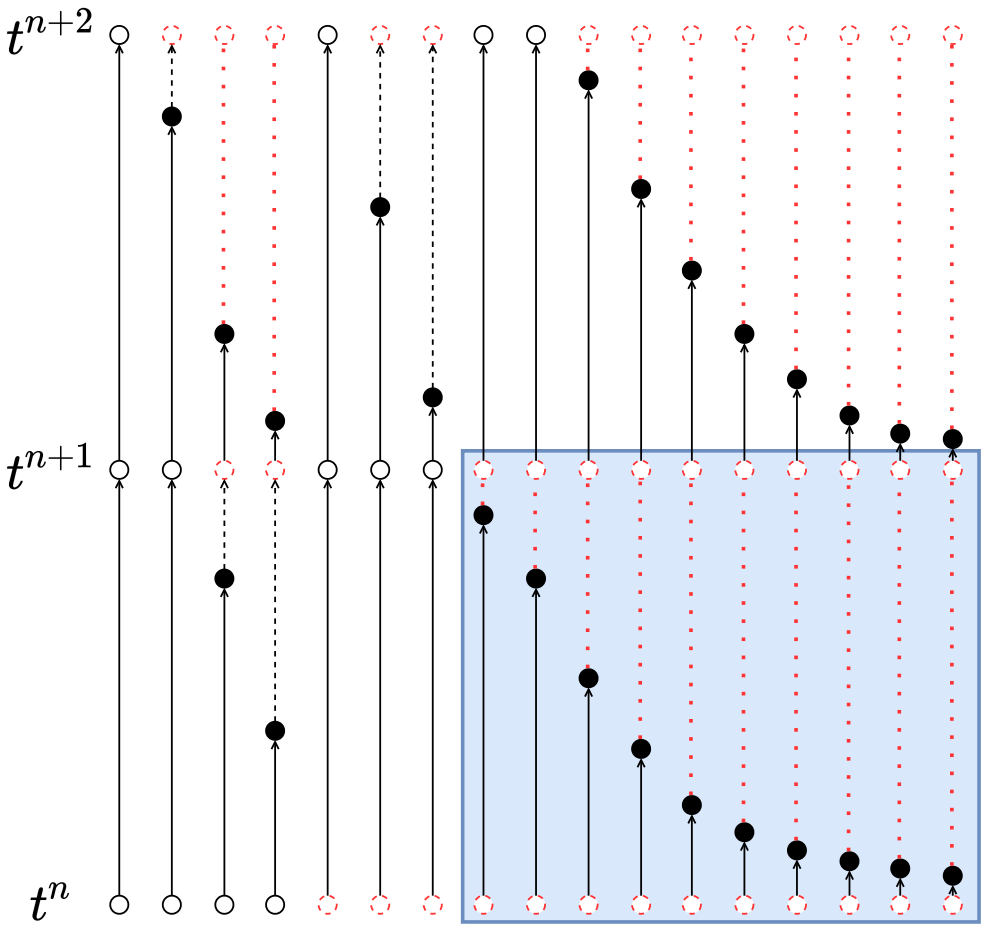

Figure 2.1: The diagram illustrates the classification and evolution of particles from t^n to t^{n+2}. Collisionless particles (black hollow circle), collisional particles (black solid circle), hydro-particle (red dash circle). Solid line means particle keeps free streaming within the time step while dash/dot line mean the particle is merged into hydrodynamic wave after collision.

As shown in Fig. 2.1, the hydro-particles (red dash circle) will be sampled at the beginning of each time step and become the candidates for collisionless/collisional

particles (black hollow/solid circle) again in the next time step evolution according to their newly-sampled t^f. The new initial distribution f_0 in cell i is represented by the newly sampled particles and remaining particles from the previous time step.

The above particle evolution strategy is called the unified gas-kinetic particle (UGKP) method. However, the UGKP can be simplified and further developed.

Note that not all particles from $\mathbf{W}_i^{h,n+1}$ need to be sampled, because some sampled particles will become collisional hydro-particles from t^{n+1} to t^{n+2} and merge into wave by collision. Therefore, the collisional hydro-particles can be represented by wave (as shown inside the blue shadow rectangle of Fig. 2.1), and only the collisionless hydro-particles need to be sampled and retained at the end of the next time step.

Therefore, only collisionless hydro-particles from the hydrodynamic wave $\mathbf{W}_i^h = \mathbf{W}_i - \mathbf{W}_i^p$ need to be re-sampled with $t_k^f = \Delta t$ at the beginning of each time step. And the dynamic impact of collisional hydro-particles, such as the contribution to the flux, can be calculated analytically. This is the basic idea of the unified gas-kinetic wave-particle (UGKWP) method.

Here, $\mathbf{W}_i^p$ is the total conservative quantities of collisionless particles remained in cell Ω_i at the end of each time step,

$$\mathbf{W}_i^p = \frac{1}{|\Omega_i|} \sum_{\mathbf{x}_k \in \Omega_i} \boldsymbol{\phi}_k, \tag{2.40}$$

where the vector $\boldsymbol{\phi}_k = m_k(1, \mathbf{u}_k, \frac{1}{2}(\mathbf{u}_k^2 + e_k))$ denotes the mass, momentum, and energy carried by the particle P_k.

Based on the cumulative distribution function of the particles' free streaming time in Eq. (2.35), the collisionless hydro-particles sampled from $g^h(\mathbf{W}_i^{n+1})$ takes only a portion of the updated hydrodynamic wave density ρ^h from the previous

time step, i.e.

$$\rho^{hp} = e^{-\Delta t/\tau}\rho^{h}. \tag{2.41}$$

Based on this observation, the noise variance in near continuum regime can be reduced because we can avoid re-sampling collisional particles repeatedly.

The interplay of waves and particles in the UGKWP method is illustrated through a series of figures in Fig. 2.2 and the particle evolution procedure in the UGKWP method can be summarized as

1. Obtain free streaming time t_k^f for the remaining particles $P_k^{f,n}$.

2. Sample the collisionless particles $P_k^{f,n}$ from hydrodynamic wave with distribution $g^h(\mathbf{W}^n)$. Note that the collisionless particles with total mass density $\rho^{hp,n} = e^{-\Delta t/\tau}\rho^{h,n}$ have the free streaming time $t^f = \Delta t$.

3. Stream all particles and evolve into two categories, i,e, collisionless particles $P_k^{f,n+1}$ and collisional particles $P_k^{c,*}$.

4. Remove collisional particles $P_k^{c,*}$ and keep collisionless particles $P_k^{f,n+1}$. The total conservative quantities of collisionless particles $\mathbf{W}^{p,n+1}$ remained can be calculated according to Eq. (2.40). The quantity of hydrodynamic wave $\mathbf{W}^{h,n+1}$ is obtained from the updated total conservative quantities $\mathbf{W}^{n+1}$ as $\mathbf{W}^{h,n+1} = \mathbf{W}^{n+1} - \mathbf{W}^{p,n+1}$. The detailed formulation in Eq. (2.15) for the update of $\mathbf{W}^{n+1}$ will be presented in the next subsection.

From Fig. 2.2c, the multi-efficiency property of UGKWP [88] is clearly indicated, i.e., the computational efficiency of UGKWP goes to the highest efficient approach in the corresponding regime. For example, in near continuum regime, i.e., $\tau \to 0$, the proportion of collisionless particle decreases exponentially and the wave becomes dominant (gray region in Fig. 2.2c). The UGKWP becomes

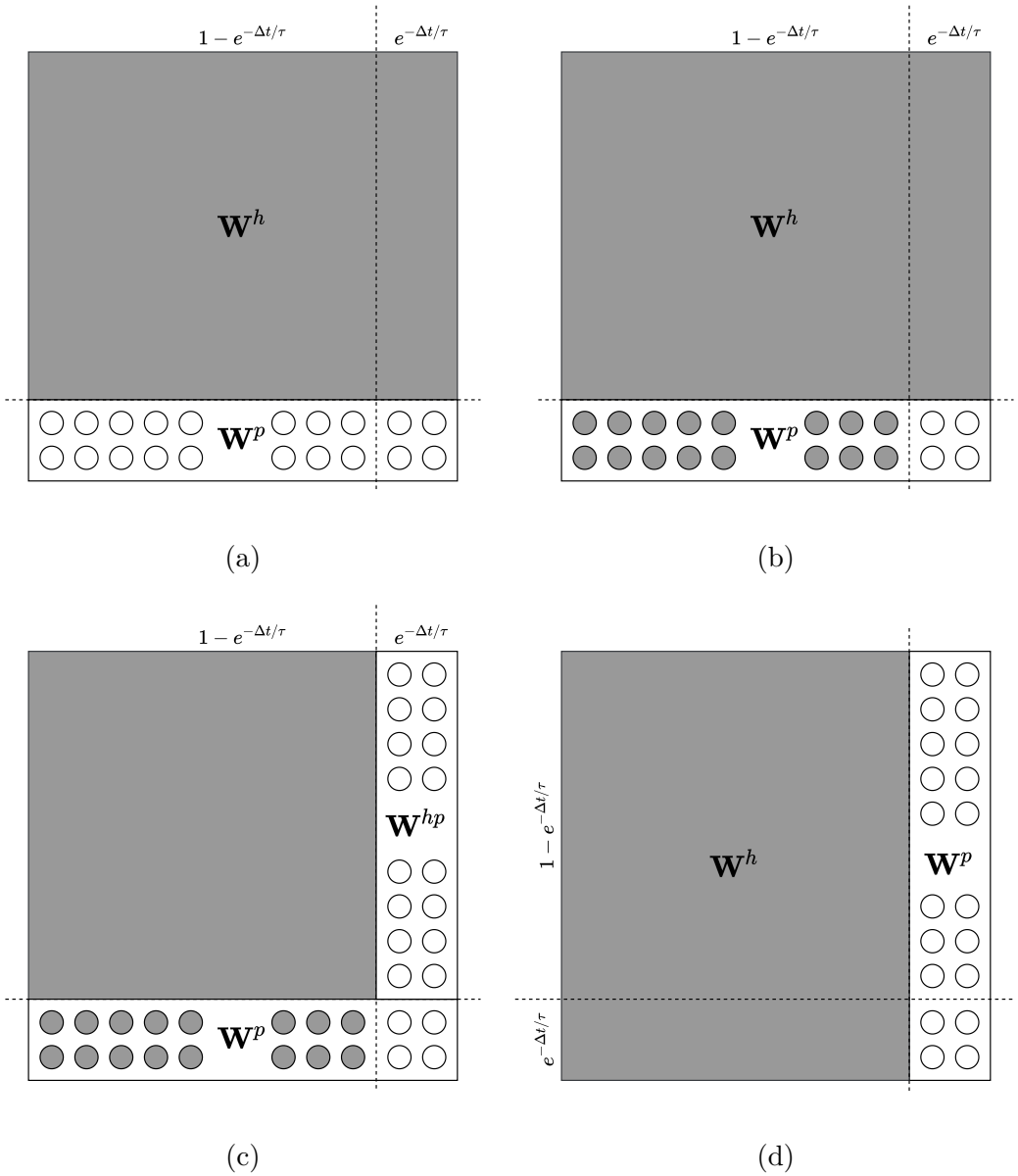

Figure 2.2: The diagram illustrates the interplay of wave and particles in the UGKWP method. Wave (gray block), collisional particle (solid circle), collisionless particle (hollow circle). (a) Initial field; (b) Classification of the collisionless particles and collisional particles for the part of $\mathbf{W}^p$ according to the free transport time t^f; (c) Sample collisionless particles $\mathbf{W}^{hp}$ from hydrodynamic waves $\mathbf{W}^h$; (d) Update solution on both macroscopic and microscopic level.

a scheme without particles, and its computational cost is comparable to a traditional NS solver. On the other hand, for rarefied gas flow with $\tau \gg \Delta t$, such as highly non-equilibrium hypersonic flow, the particles will play a dominant role to capture the non-equilibrium transport (circle in Fig. 2.2c), and the efficiency of the scheme will go to the stochastic particle method, such as DSMC.

It has been shown in [88] that the UGKWP method is a kinetic equation solver in the rarefied regime and preserves the Navier-Stokes solution in the continuum regime as the particles are re-sampled from the first-order approximation of g^h. Even though the particles are sampled uniformly inside the control volume, the spatial accuracy can be still kept in the near continuum regime, because in the update of $\mathbf{W}$, the portion of particles $e^{-\Delta t/\tau}$ is minimal while the hydrodynamic wave evolution is dominant and is computed analytically with second-order accuracy.

Compared with the DSMC method, which requires free streaming time $t^f = \Delta t$ to be less than the particle mean collision time, the free transport time $t^f \leq \Delta t$ in UGKWP method is obtained by the sampling process in Eq. (2.36). Moreover, the particle collisional effect, such as evolving to the equilibrium distribution g^h, has been modeled in UGKWP method through the evolution solution in Eq. (2.33). Without using this evolution solution with time accumulating particle collision effect, or any other equivalent form, it is impossible to design a multiscale method, which can recover the NS solution in the continuum flow regime.

2.2.4 Update of Macroscopic Variables

The UGKWP updates the macroscopic variables in each control volume from Eq. (2.15). The equilibrium part flux $\mathbf{F}_{ij}^{eq}$ is directly calculated from the macroscopic flow field as given by Eq. (2.31).

In UGKWP, the free streaming flux $\mathbf{F}_{ij}^{fr}$ in Eq. (2.31) is divided into two parts and computed partially by particles free steaming and partially by the contribution of $g^h(\mathbf{W}^h)$ analytically. The free streaming flux from collisional hydrodynamic waves of $(1-e^{-\Delta t/\tau})\mathbf{W}^h$ can be calculated analytically. The other free streaming flux from collisionless particles $e^{-\Delta t/\tau}\mathbf{W}^h$ in the hydrodynamic wave and the remained particles of $\mathbf{W}^p$ can be evaluated by counting the particles going in and out the cell during a time step.

The free streaming flux contributed from the collisional hydro-particles of $(1-e^{-\Delta t/\tau})\mathbf{W}^h$ on the cell interface ij is

$$\begin{aligned}\mathbf{F}_{ij}^{fr,h} &= \mathbf{F}_{ij}^{fr,UGKS}(\mathbf{W}^h) - \mathbf{F}_{ij}^{fr,DVM}(\mathbf{W}^{hp}) \\ &= \int \mathbf{u}\cdot\mathbf{n}_{ij}\left[(q_4 g^h + q_5\mathbf{u}\cdot\nabla_{\mathbf{x}} g^h) - e^{-\Delta t/\tau}\int_0^{\Delta t}(g^h - t\mathbf{u}\cdot\nabla_{\mathbf{x}} g^h)\,\mathrm{d}t\right]\boldsymbol{\psi}\,\mathrm{d}\Xi \\ &= \int \mathbf{u}\cdot\mathbf{n}_{ij}\left[(q_4 - \Delta t e^{-\Delta t/\tau})g^h + (q_5 + \frac{\Delta t^2}{2}e^{-\Delta t/\tau})\mathbf{u}\cdot\nabla_{\mathbf{x}} g^h\right]\boldsymbol{\psi}\,\mathrm{d}\Xi,\end{aligned} \tag{2.42}$$

where g^h is the Maxwellian distribution with temperature and bulk velocity determined by macroscopic variables $\mathbf{W}$, except the density is same as $\mathbf{W}^h$. $g_{\mathbf{x}}^h$ is the gradient of the Maxwellian distribution, which can be obtained from the reconstruction of $\mathbf{W}$ and $\mathbf{W}^h$.

Statistically, the subtraction of $\mathbf{F}_{ij}^{fr,DVM}(\mathbf{W}^{hp})$ from $\mathbf{F}_{ij}^{fr,UGKS}(\mathbf{W}^h)$ aims to remove the accumulating free transport fluxes from the collisionless hydro-particle sampled from $\mathbf{W}^h$.

The total non-equilibrium free streaming flux $\mathbf{F}_{ij}^{fr}$ also includes the contribution from the remaining particles P_k from the previous time step. During the free transport process, the contribution of particles to the microscopic flux of cell i can be obtained by counting the particles across the cell interfaces during a time step,

$$\mathbf{F}_i^{fr,p} = \sum_{\mathbf{x}_k^{n+1},\mathbf{x}_k^*\in\Omega_i}\boldsymbol{\phi}_k - \sum_{\mathbf{x}_k^n\in\Omega_i}\boldsymbol{\phi}_k. \tag{2.43}$$

Finally, the updates of the conservative flow variables in the UGKWP method are

$$\begin{aligned}\mathbf{W}_i^{n+1} &= \mathbf{W}_i^n - \frac{1}{|\Omega_i|}\sum_{j\in N(i)}\mathbf{F}_{ij}^{eq}|S_{ij}| - \frac{1}{|\Omega_i|}\sum_{j\in N(i)}\mathbf{F}_{ij}^{fr}|S_{ij}|, \\ &= \mathbf{W}_i^n - \frac{1}{|\Omega_i|}\sum_{j\in N(i)}\mathbf{F}_{ij}^{eq}|S_{ij}| - \frac{1}{|\Omega_i|}\sum_{j\in N(i)}\mathbf{F}_{ij}^{fr,h}|S_{ij}| + \frac{\mathbf{F}_i^{fr,p}}{|\Omega_i|}.\end{aligned} \tag{2.44}$$

In conclusion, the UGKWP method improves UGKP method mainly in the following two aspects:

- The free transport terms in numerical flux contributed by the collisional hydro-particles are evaluated analytically as $\mathbf{F}^{fr,h}$;
- Only collisionless hydro-particles are sampled.

2.2.5 Boundary Conditions

The proper treatment of boundary condition is crucial for a numerical scheme. For a diffusive wall condition with normal direction $\mathbf{n}$ pointing toward the computational domain, the incoming distribution function $f_{in}(t)$ at boundary is given by Eq. (2.24). The distribution function of emitted particles from the wall has a Maxwellian distribution

$$g_w = \rho_w\left(\frac{1}{2\pi RT_w}\right)^{\frac{3+K}{2}}\exp\left[-\frac{(\mathbf{u}-\mathbf{U}_w)^2+\boldsymbol{\xi}^2}{2RT_w}\right], \tag{2.45}$$

where T_w and $\mathbf{U}_w$ are prescribed wall temperature and velocity. Based on the non-penetration condition, ρ_w in the above Maxwellian is given by

$$\int_0^{\Delta t}\int_{\mathbf{n}\cdot(\mathbf{u}-\mathbf{u}_w)<0}\mathbf{n}\cdot(\mathbf{u}-\mathbf{u}_w)f_{in}(t)\,\mathrm{d}\Xi\,\mathrm{d}t = \Delta t\int_{\mathbf{n}\cdot(\mathbf{u}-\mathbf{u}_w)\geq 0}\mathbf{n}\cdot(\mathbf{u}-\mathbf{u}_w)g_w\,\mathrm{d}\Xi. \tag{2.46}$$

In UGKWP method, the boundary treatment involves macroscopic fluxes evaluation and particle reflection. The evaluation of macroscopic fluxes $\mathbf{F}_{ij}^{eq}$ and

$\mathbf{F}_{ij}^{fr,h}$ are straightforward by assuring mass flux equal to zero, from which ρ_w is obtained.

As for particle reflection, the procedure is the same as the diffuse reflection in DSMC simulation. Without loss of generality, let $\mathbf{U}_w = \mathbf{0}$ and (u, v, w) be the reflected velocity, where u is normal to the surface oriented toward the computational domain, v, w are the tangential components. Given an incident particle, once it hits the wall, the scattered velocity follows

$$ug_w \,\mathrm{d}u \,\mathrm{d}v \,\mathrm{d}w = \rho_w \left(\frac{\lambda_w}{\pi}\right)^{1/2} u \exp(-\lambda_w u^2) \,\mathrm{d}u f(v) f(w) \,\mathrm{d}v \,\mathrm{d}w, \tag{2.47}$$

where

$$f(v)f(w) \,\mathrm{d}v \,\mathrm{d}w = \frac{\lambda_w}{\pi} \exp[-\lambda_w(v^2 + w^2)] \,\mathrm{d}v \,\mathrm{d}w. \tag{2.48}$$

With polar coordinates transformation, $v = r\cos\theta$ and $w = r\sin\theta$, one will have

$$f(v)f(w) \,\mathrm{d}v \,\mathrm{d}w = \frac{\lambda_w}{\pi} \exp(-\lambda_w r^2) r \,\mathrm{d}r \,\mathrm{d}\theta = \exp(-\lambda_w r^2) \,\mathrm{d}(\lambda_w r^2) \,\mathrm{d}\frac{\theta}{2\pi}. \tag{2.49}$$

Hence, the cumulative distribution function of $\lambda_w r^2$ is

$$\mathscr{F}(\lambda_w r^2) = 1 - \exp(-\lambda_w r^2), \tag{2.50}$$

and $\theta/(2\pi)$ is uniformaly distributed between 0 and 1.

The normal component u of the particle is scattered off the surface diffusely and has a distribution function of the form

$$f(u) \,\mathrm{d}u = Cu \exp(-\lambda_w u^2) \,\mathrm{d}u = C/(2\lambda_w) \exp(-\lambda_w u^2) \,\mathrm{d}(\lambda_w u^2), \tag{2.51}$$

and its cumulative distribution function is the same as Eq. (2.50).

Finally, given $\eta_1, \eta_2, \eta_3 \sim U(0, 1)$ are random numbers generated from a uniform distribution on the interval $(0, 1)$, we can sample the velocity of reflected particle

as following,

$$
\begin{aligned}
u &= (-\ln \eta_1/\lambda_w)^{1/2}, \\
r &= (-\ln \eta_2/\lambda_w)^{1/2}, \quad \theta = 2\pi\eta_3 \\
v &= r\cos\theta, \quad w = r\sin\theta.
\end{aligned} \tag{2.52}
$$

2.2.6 Miscellaneous Details

(a) Time Step on Unstructured Mesh

Follow the implementation in [100], the time step for unsteady flow simulation is obtained from

$$\Delta t = C \min_i \frac{\Omega_i}{\Lambda_i^x + \Lambda_i^y + \Lambda_i^z}, \tag{2.53}$$

with Courant number C typically satisfied by $0 < C < 1$ and convective spectral radii of cell i

$$
\begin{aligned}
\Lambda_i^x &= (|U_i| + c)\Delta S_i^x, \\
\Lambda_i^y &= (|V_i| + c)\Delta S_i^y, \\
\Lambda_i^z &= (|W_i| + c)\Delta S_i^z,
\end{aligned} \tag{2.54}
$$

where $c = 3\sigma_i = 3\sqrt{RT_i}$ is approximately the sound speed, $\mathbf{u}_i = (U_i, V_i, W_i)$ is the macroscopic velocity. The variables ΔS_i^x, ΔS_i^y, and ΔS_i^z, respectively, represent projections of the control volume on the y-z-, x-z-, and x-y-plane, which are given by

$$
\begin{aligned}
\Delta S_i^x &= \frac{1}{2}\sum_{j\in N(i)} |S_{ij}^x|, \\
\Delta S_i^y &= \frac{1}{2}\sum_{j\in N(i)} |S_{ij}^y|, \\
\Delta S_i^z &= \frac{1}{2}\sum_{j\in N(i)} |S_{ij}^z|,
\end{aligned} \tag{2.55}
$$

where S_{ij}^x, S_{ij}^y, and S_{ij}^z denote the x-, y-, and the z-component of the face vector $\mathbf{S}_{ij} = |S_{ij}|\mathbf{n}_{ij}$.

(b) Particle Sampling

At the beginning of each time step, the velocity of collisionless particles associated with hydrodynamic waves will be sampled in pairs from Maxwellian distribution function $g(\mathbf{W}^n)$. Specifically, given with the macroscopic velocity $\mathbf{U} = (U, V, W)$, temperature T, and vector $\boldsymbol{\eta}$ that sampled from the normal distribution using the Marsaglia polar method [101], a pair of particles with microscopic velocities $\mathbf{u} = \mathbf{U} + \sqrt{RT}\boldsymbol{\eta}$ and $\mathbf{u}' = \mathbf{U} - \sqrt{RT}\boldsymbol{\eta}$ will be sampled.

To determine the sampling particle number N_{sam} in the cell, a prescribed preference number N_{ref} is required. Further, the reference mass m_{ref} can be determined from the total particle mass and the reference number N_{ref}

$$m_{ref} = \frac{(\rho^p + \rho^{hp})|\Omega|}{N_{ref}} = \frac{(\rho^p + e^{-\Delta t/\tau}\rho^h)|\Omega|}{N_{ref}}. \tag{2.56}$$

Once the reference mass m_{ref} is available, the number of particles to be sampled symmetrically (antithetic variates method for variance reduction [102]) is determined by

$$N_{sam} = 2\left\lceil \frac{\rho^{hp}|\Omega|}{2m_{ref}} \right\rceil = 2\left\lceil \frac{e^{-\Delta t/\tau}\rho^h|\Omega|}{2m_{ref}} \right\rceil. \tag{2.57}$$

If the reference mass m_{ref} is the same for all cells, then the total number of particles per cell would be exactly equal to N_{ref}. By this means, the total number of particles in each cell can be controlled around the given reference number N_{ref} in near continuum regime regardless of mesh distribution. Moreover, the minimum number of particles N_{min} per cell can be prescribed to adjust the sampled particles' number such that

$$N_{sam} = \max\{N_{sam}, N_{min} - N_{left}\}, \tag{2.58}$$

where N_{left} is the collisionless particles left at the beginning of each time step.

Finally, the sampled mass weight m_{sam} for each sampled particle is

$$m_{sam} = \frac{\rho^{hp}|\Omega|}{N_{sam}} = \frac{e^{-\Delta t/\tau}\rho^h|\Omega|}{N_{sam}}, \tag{2.59}$$

which guarantees that the total sampled mass is exactly equal to $\rho^{hp}|\Omega|$.

For Shakhov model, following the importance sampling strategy [102], we only need to modify the sampling weight m_k by multiplying a factor

$$m_k \left[1 + \frac{(1-\mathrm{Pr})}{5} \frac{\mathbf{q}\cdot\mathbf{c}}{pRT}\left(\frac{\mathbf{c}^2}{2RT} - \frac{5}{2}\right)\right].$$

As for the determination of the simulation parameter N_{ref}, it depends on the Knudsen number Kn and the desired accuracy. As pointed out in [102], the root mean square error (RMSE) in Monte Carlo integration is $E[\epsilon_N[f]^2]^{1/2} = \sigma N^{-1/2}$, that is of size $\mathcal{O}(N^{1/2})$ with a constant σ as the variance of the integrand f. In the UGKWP method, under the same numerical setup, the noise reduces as the square root of the increasing number of particles.

Furthermore, the variance in the RMSE is no longer constant. It decrease as $e^{-\Delta t/\tau}$ since the portion of particle decrease as $e^{-\Delta t/\tau}$ in UGKWP method, which distinguishes UGKWP method from other stochastic particle methods based on kinetic model equations [50, 51].

Generally speaking, for a three-dimensional steady-state problem, the N_{ref} can range from a few hundred to a few thousand simulated particles per cell. If the quantities of second-order moments like temperature are not emphasized, dozens of particles per cell are enough.

(c) Time Averaging

For steady-state solution, the flow field $\bar{\mathbf{W}}$ starts to be averaged after a given time step N_{avg},

$$\bar{\mathbf{W}} = \frac{\sum\limits_{n>N_{avg}} \Delta t^n \mathbf{W}^n}{\sum\limits_{n>N_{avg}} \Delta t^n} \tag{2.60}$$

where $\Delta t^n = t^n - t^{n-1}$.

The averaged flow field $\bar{\mathbf{W}}$ is assumed to be convergent if the relative change in two-successive steps is less than a given tolerance, such as $\varepsilon = 10^{-8}$. Then, the flow variables, such as the temperature $\bar{T}$ and macroscopic velocity $\bar{\mathbf{U}}$, can be obtained from the averaged conservative flow variables $\bar{\mathbf{W}}$.

(d) Numerical Dissipation

The UGKWP targets the continuum and rarefied flow. In the continuum flow regime, the strong shock structure is usually unresolved by the mesh size. Therefore, numerical dissipation is added through relaxation time to enlarge the shock thickness to the mesh size scale,

$$\tau_{num} = \frac{\mu}{P} + C_2 \frac{|P_l - P_r|}{|P_l + P_r|} \Delta t, \tag{2.61}$$

where P_l and P_r are the reconstructed pressures at the left and right side of the cell interface and C_2 is a constant, such as $C_2 = 10$ for strong shock in the continuum regime.

2.3 Implementation Details

UGKWP solver is constructed under a finite volume framework on 3D unstructured mesh. It includes not only the reconstruction and flux evaluation module as in the traditional finite volume solver, but also the particle sampling and tracking module as in pure particle method.

2.3.1 Structure of the Solver

The main components of UGKWP solver are sketched in Fig. 2.3. As shown in the diagram, the program starts with the pre- and post-processor module, where

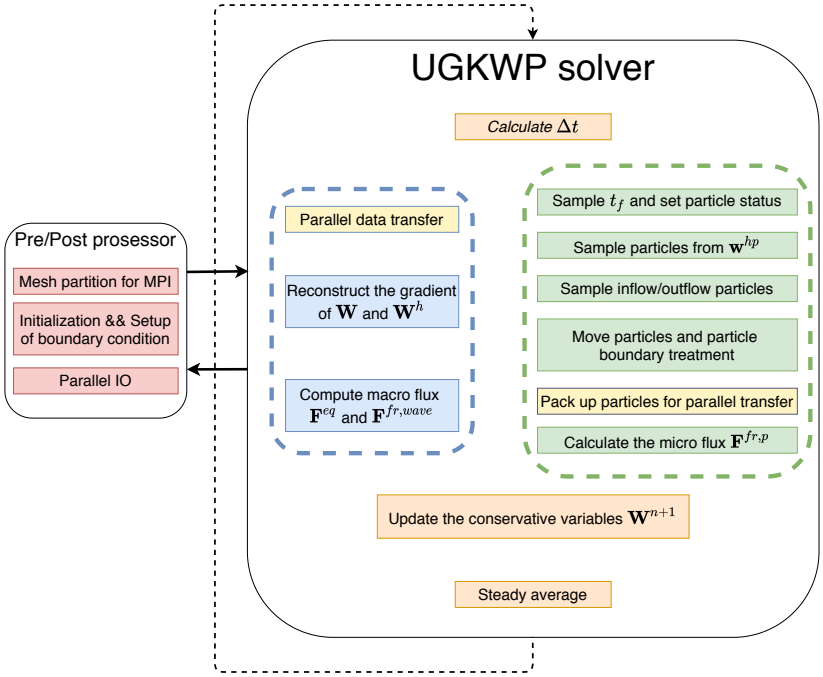

Figure 2.3: The structure and main components of the UGKWP solver

the mesh partition, initialization, setup of boundary condition, and parallel IO are handled inside. In UGKWP solver, the numerical procedures are organized into a macroscopic field level and a microscopic particle level. Accordingly, the macroscopic components surrounded by the blue dash line consist of the parallel data transfer, reconstruction of the macroscopic gradient, and macroscopic flux calculation with boundary treatment. The green dash block contains the components for microscopic particles which are stored in the doubly-linked list. There are frequent operations, such as tracking particles and calculating the macroscopic fluxes. The insert/delete operation is efficient in the scenario of parallel transfer and sampling/elimination of the particles.

2.3.2 Parallelization

The parallelization of the current code adopts Message Passing Interface (MPI) on the physical mesh decomposition. Every MPI process deals with a non-

overlapping sub-domain, and the information like conservative variables and particles are communicated with the neighboring domain through corresponding boundaries. Since the macroscopic solver has second-order accuracy, no padding area of sub-domain is required.

The code was evaluated on Tianhe-2, a supercomputer at China's National Supercomputer Center in Guangzhou. Tianhe-2 has 16,000 nodes, each with an Intel Xeon E5-2692 CPU with 12 cores running at 2.2 GHz and 88 gigabytes of memory (64 used by the Ivy Bridge processors, and 8 gigabytes for each of the Xeon Phi processors). The computing nodes of Tianhe-2 are interconnected by TH Express-2 network.

To test the parallel efficiency and scalability of the UGKWP, the code is compiled using Intel C/C++ compiler of version 18.0.0 with -O3 optimization flag, and are linked to the MPICH2 with a customized GLEX channel. Since the scaling is problem-specific (depending on Knudsen number and preference number of particles per cells N_{ref}), multiple test cases and factors affecting the performance will be analyzed in a series of three-dimensional lid-driven cavity flow tests.

Macroscopic Field Computation

Firstly, only the parallel speedup of pure macroscopic field computation using different MPI processes is measured to eliminate the computation of particles and communication of particle parallel transfer. Without the involvement of particle generation and particle transportation, the UGKWP degenerates to the gas-kinetic scheme (GKS) for the continuum flow computation [103]. As it becomes a deterministic solver, for simplicity, the Knudsen number is fixed at 10^{-4} in the following parallel computation. The averaged running time (wall clock time) of a single iteration step is measured, and the measurement is ensured to be over 100 seconds, and no IO time is counted.

To investigate the Amdahl's law (strong scaling) at different fixed problem size, the physical domain is discretized as D^3, where D is the number of cells along each direction and D has the values $64, 128, 256$ cells. To test the Gustafson's law (weak scaling), we concern the speedup for a scaled problem size to the number of processors. Hence, $D = 64$ on one node with 24 cores is chosen as the baseline, i.e., keeping the number of cells per processors as $64^3/24$, and the grid size increased simultaneously as the increment of the number of processors P. The corresponding speedup is measured based on the averaged single-node simulation time, i.e., $S_P = 24T_p/T_{24}$.

Both strong and weak scaling analysis is plotted in Fig. 2.4. The solid red line represents the ideal linear speedup. From the diagram, the overall computational time of the various physical grid sizes scales well with the number of processing cores (or MPI processes). Although strong scaling is very sensitive towards the serial fraction of the program, the communication overhead (e.g., synchronization) could further degrade the performance. But the worst efficiency still has 73.8% for the case $D = 64$ with $P = 960$ number of processors. Moreover, it is observed that strong scaling performance increases considerably as the increase of grid size. The strong scaling parallel efficiency for the largest problem size $D = 256$ can reach 85.4% despite the usage of $P = 1536$ number of processing cores. Finally, the weak scaling is also verified by increasing both the job size and the number of processing cores, and a satisfactory weak scaling efficiency up to 92% has been achieved even with $P = 1536$ number of processing cores.

Involvement of Microscopic Particles

Next, the particles are included in the experiment to explore the scalability and parallel efficiency of the implementation. Problems with different numbers of cells D^3, Knudsen number Kn, and preference number of particles per cell N_{ref}

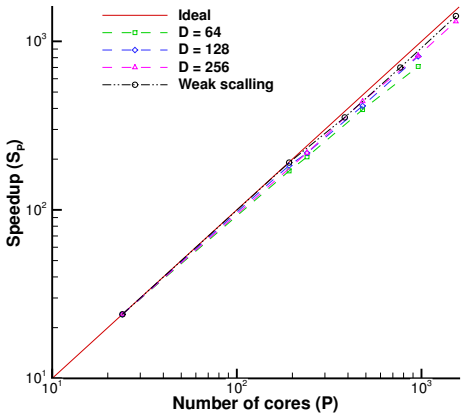

Figure 2.4: Strong and weak scaling analysis without the involvement of particles

are run across different nodes. The maximum problem size is limited by the total memory available on each node, and no IO time is recorded. The average computing time (wall clock time) for a single iteration step is averaged from 1001 to 1100 steps to ensure sufficient running time and reach a steady-state solution.

The averaged CPU time (second) per step against the number of cores is shown in Fig. 2.5. The results indicate that the scaling performance is good for all simulations because the CPU time decreases almost linearly as the increase in the number of processing cores. Actually, from Table 2.1 and Table 2.2, the parallel efficiency $E_P = S_P/P$ for cases with $D \geq 72$ is over 86% even with $P = 864$ number of processing cores.

Furthermore, several interesting patterns have been observed. Firstly, for the cases of both $N_{ref} = 50$ and $N_{ref} = 500$, we can observe that the absolute CPU time raises with not only the increment of grid size, but also the Knudsen number. The reason is that the mean free path of the particles becomes large at a high Knudsen number, which produces the unbalanced distribution of particles among different sub-domains as well as in the processing cores. Secondly, the scaling performance deteriorates as the shrinkage of grid size, especially in high-Knudsen number cases, because the proportion of communication time would

increase with the decrease of number of cells per core. The uneven effect of particles distributed among processing cores are amplified. Accordingly, the worst parallel efficiency $E_{864} = 68.7\%$ is observed for the case $D = 36$ at $\mathrm{Kn} = 1$ with respect to $P = 864$ number of cores. Lastly, the parallel efficiency would increase as the enlargement of the reference number of particles.

Another interesting phenomenon is that maximum parallel efficiency can be greater than one. For instance, the maximum parallel efficiency observed can be $E_{864} = 123.2\%$ in the cases of $D = 72, Kn = 10^{-2}$ and $N_{ref} = 500$ using $P = 864$ cores. Actually, the parallel efficiency in transition regime ($\mathrm{Kn} = 10^{-2}$) is even higher than that in the near continuum regime ($\mathrm{Kn} = 10^{-4}$) with the same grid size D and reference number of particles N_{ref}. Besides, the worst parallel efficiency is even larger than 86.3% for all cases at $\mathrm{Kn} = 10^{-4}, 10^{-2}$. This counterintuitive parallel efficiency in the transition regime is probably due to the doubly-linked list data structure for storing particles. In the transition or near continuum regime, the collision between particles is intensive, and the frequent elimination/resampling of particles involves frequent delete/insert operation in memory. Nonetheless, the bottleneck caused by the implemented data structure can be alleviated through the replacement of a sequence container, like the STL vector.

In summary, intensive parallel tests of cavity flow show satisfactory strong and weak scaling performance of the UGKWP code. The current implementation becomes a valuable tool for simulating complex flow problems across thousands of processing cores in parallel computation. However, the actual parallel efficiency might vary for particular simulation setup.

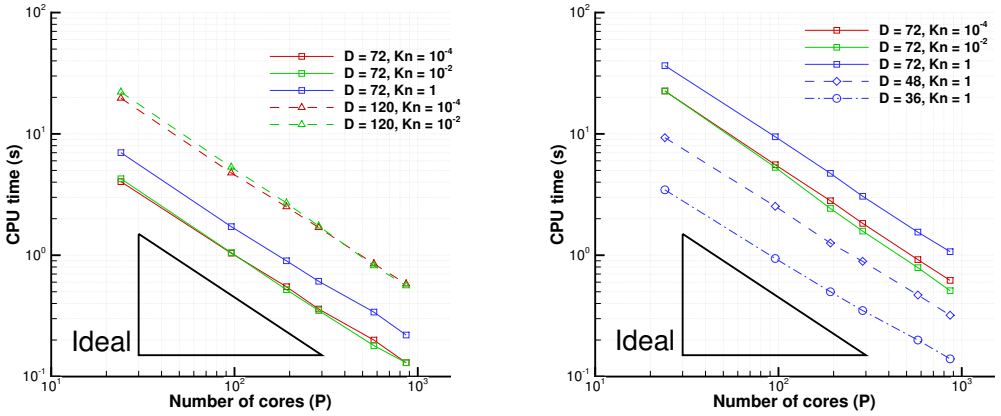

(a) (b)

Figure 2.5: Performance scaling on Tianhe-2 where each node has 24 cores (a) $N_{ref} = 50$ and (b) $N_{ref} = 500$

Nodes	Cores	$D = 72$			D = 120	
		Kn $= 10^{-4}$	Kn $= 10^{-2}$	Kn $= 1$	Kn $= 10^{-4}$	Kn $= 10^{-2}$
1	24	100%	100%	100%	100%	100%
4	96	97.1%	101.7%	101.9%	103.2%	103.9%
8	192	91.8%	102.6%	97.4%	98.1%	102.3%
12	288	93.5%	101.7%	95.8%	97.1%	105.8%
24	576	84.2%	98.8%	85.9%	96.6%	112.3%
36	864	86.3%	91.2%	88.5%	94.3%	109.6%

Table 2.1: Parallel efficiency for cases with $N_{ref} = 50$ on Tianhe-2

Nodes	Cores	$D = 72$			$D = 48$	$D = 36$
		$\mathrm{Kn} = 10^{-4}$	$\mathrm{Kn} = 10^{-2}$	$\mathrm{Kn} = 1$	$\mathrm{Kn} = 1$	$\mathrm{Kn} = 1$
1	24	100%	100%	100%	100%	100%
4	96	101.2%	106.7%	96.4%	92%	92%
8	192	100.3%	116.3%	96.5%	92.4%	86.5%
12	288	102.7%	119.3%	99.5%	87.2%	82.4%
24	576	102.1%	119.3%	98.2%	82.5%	72.1%
36	864	101%	123.2%	94.8%	80.8%	68.7%

Table 2.2: Parallel efficiency for cases with $N_{ref} = 500$ on Tianhe-2

2.4 Numerical Results

In this section, the accuracy and computational efficiency of the UGKWP solver will be evaluated through many test cases with a wide range of Knudsen and Mach numbers. The numerical Sod shock tube problem in 3D, lid-driven cubic cavity flow, high-speed flow passing through a cube, and the flow around a space vehicle, are tested. The results are compared with those from UGKS/DUGKS and DSMC. Without further statement, the fully diffusive boundary condition is applied on the isothermal wall boundary. The code is compiled with GCC version 7.5.0, and all computations are carried out on a workstation with [Dual CPU] Intel®Xeon(R) Platinum 8168 @ 2.70GHz with 48 cores and 270 GB memory unless indicated otherwise.

2.4.1 3D Sod Shock Tube

The Sod shock tube problem insides a square-column is simulated for diatomic gas at different Knudsen numbers to validate the current UGKWP method, and the result is compared with the 1D UGKS solution.

In this test case, the following non-dimensionalization is used

$$\hat{\rho} = \frac{\rho}{\rho_\infty},\ \hat{U} = \frac{U}{C_\infty},\ \hat{V} = \frac{V}{C_\infty},\ \hat{W} = \frac{W}{C_\infty},\ \hat{T} = \frac{T}{T_\infty},\ \hat{P} = \frac{P}{\rho_\infty C_\infty^2},$$
$$\hat{t} = \frac{t}{t_\infty},\ \hat{x} = \frac{x}{L},\ C_\infty = \sqrt{\frac{2k_B T_\infty}{m}},\ t_\infty = \frac{L}{C_\infty},$$

and the initial condition for the non-dimensional variables is

$$(\hat{\rho}, \hat{U}, \hat{V}, \hat{W}, \hat{P}) = \begin{cases} (1,0,0,0,1), & 0 < \hat{x} < 0.5, \\ (0.125,0,0,0,0.1), & 0.5 < \hat{x} < 1. \end{cases} \tag{2.62}$$

For UGKWP simulation, the physical domain is a $[0,1]\times[-0.1,0.1]\times[-0.1,0.1]$ square-column tube, which is discretized by $100\times5\times5$ uniform mesh points. The preset reference numbers of particles are $N_{ref} = 200, 400, 1000, 2000,\ 3200, 3200$ for the cases at $\mathrm{Kn} = 10^{-4}, 10^{-3}, 10^{-2}, 0.1, 1, 10$ respectively. Least square reconstruction with Venkatakrishnan limiter is utilized. For the UGKS simulation, the 1D physical domain $[0,1]$ is discretized uniformly with 100 cells. Composed Newton-Cotes quadrature with 101 velocity points in range $[-6,6]$ is fixed to discretize the one-dimensional velocity space. van Leer limiter is used for the reconstruction of both conservative variables and discrete distribution function. The left and right boundaries are treated as far-field, and the others are treated as symmetric planes. The CFL number for both UGKWP and UGKS simulation is 0.9, and the reference viscosity is given in Eq. (2.12) with $\omega = 0.74$. The results at the time $t = 0.12$ in all flow regimes are presented.

The density, velocity, and temperature obtained by the UGKS and the UGKWP method at different Knudsen numbers are plotted in Figures 2.6 to 2.11, where

the three-dimensional flow field computed by UGKWP is projected to the x-direction by taking ensemble average over the cells on y-z plane. No time averaging is applied, and the statistical noise is satisfactory for this unsteady flow simulation. For all the cases in different flow regimes, the 3D UGKWP solutions agree well with the 1D UGKS data. The slight difference is due to different limiters, i.e., van Leer limiter for UGKS and Venkatakrishnan limiter for UGKWP. The capability of the UGKWP method for numerical simulations in both continuum and rarefied regime is confirmed.

The distinguishable feature of multi-efficiency [88] can also be demonstrated here. For UGKS, the computational costs will be on the same order for all Knudsen number cases since the discretization in the particle velocity space is the same. While for the UGKWP method, the computational cost is reduced at small Knudsen number, e.g., Kn $= 10^{-4}$ in near continuum regime, where the hydrodynamic wave is dominant, and few particles are sampled and tracked. The computational cost of UGKWP for 3D simulation is admissible because only a few hundred or thousand particles are enough to adaptively discretize the velocity space, whereas it becomes possible that 101^3 mesh points in the velocity space may be required in DVM-based UGKS for high speed flow. For steady-state simulation, the number of particles can be reduced further since the statistical noise can be suppressed through the temporal ensemble.

2.4.2 Lid-driven Cubic Cavity Flow

For low-speed flow, the UGKWP method is applied to study the three-dimensional lid-driven cubic cavity flow in the transition regime, and the results are compared with the solution predicted by dugksFoam [34].

The side length of the cubic cavity is $L = 1$m with the computational domain $[0, 1] \times [0, 1] \times [0, 1]$, which is divided non-uniformly into 40^3 hexahedrons with

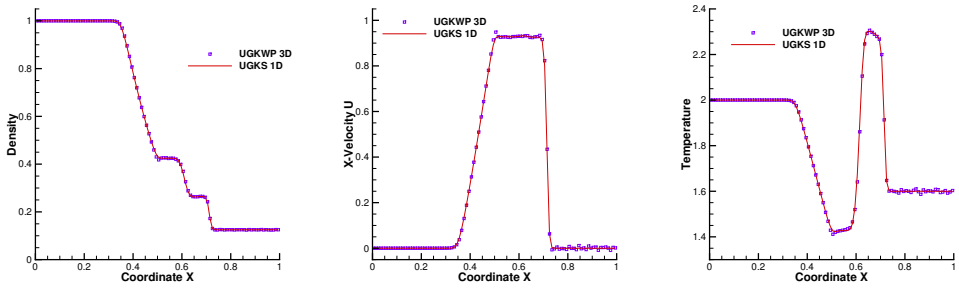

(a) (b) (c)

Figure 2.6: Sod shock tube at Kn = 10^{-4}. (a) Density, (b) X-Velocity U, and (c) Temperature.

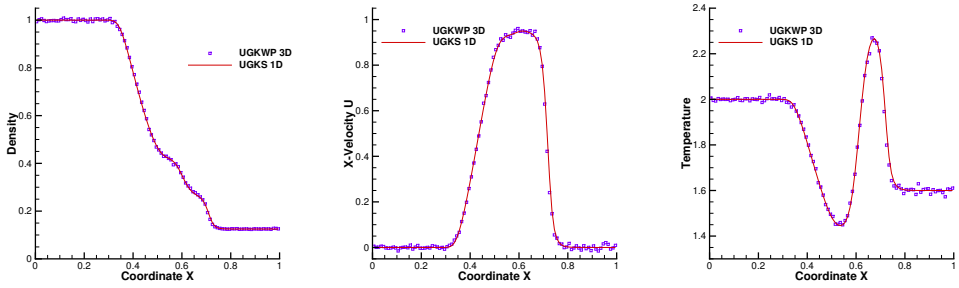

(a) (b) (c)

Figure 2.7: Sod shock tube at Kn = 10^{-3}. (a) Density, (b) X-Velocity U, and (c) Temperature.

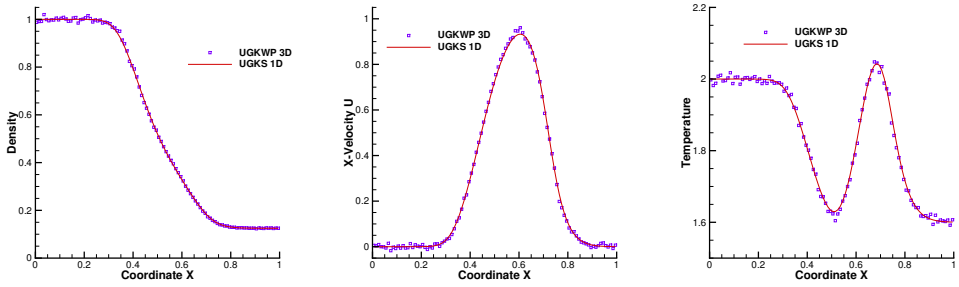

(a) (b) (c)

Figure 2.8: Sod shock tube at Kn = 10^{-2}. (a) Density, (b) X-Velocity U, and (c) Temperature.

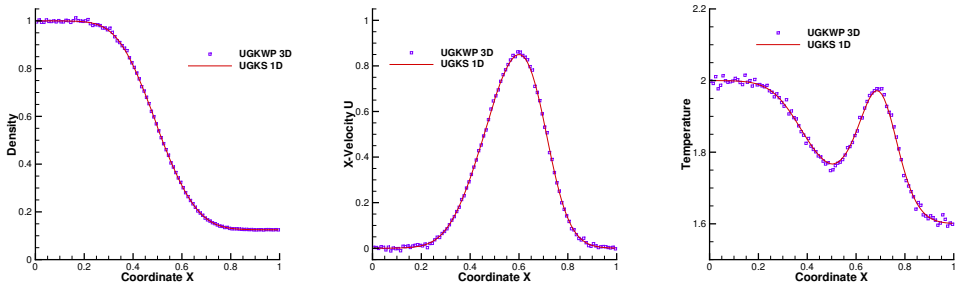

(a) (b) (c)

Figure 2.9: Sod shock tube at Kn = 0.1. (a) Density, (b) X-Velocity U, and (c) Temperature.

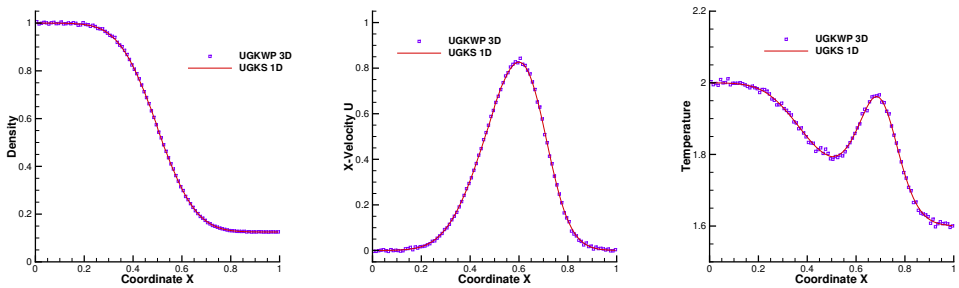

(a) (b) (c)

Figure 2.10: Sod shock tube at Kn = 1. (a) Density, (b) X-Velocity U, and (c) Temperature.

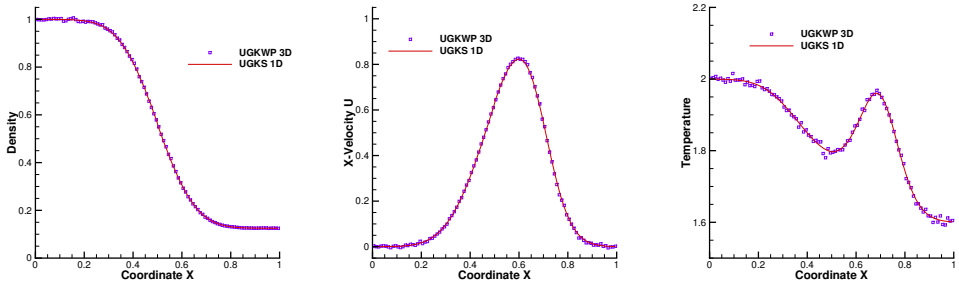

(a) (b) (c)

Figure 2.11: Sod shock tube at Kn = 10. (a) Density, (b) X-Velocity U, and (c) Temperature.

the cell size gradually increased towards to the cavity center. The ratio of the cell size in the center and the boundary is about 2. The lid (top boundary) of the cavity moves in the positive x-direction with a constant velocity U_w = 50m/s, while the other walls are kept fixed. All sidewalls have the diffusive boundary condition and keep a uniform temperature T_w = 273K. The cavity is composed of monatomic argon gas with molecular mass $m = 6.63 \times 10^{-26}$kg and diameter $d = 4.17 \times 10^{-10}$m. The Knudsen number is Kn = $\lambda/L = 0.075$, where the mean free path λ is calculated from the initial uniform gas density by $\lambda = m/(\sqrt{2}\pi d^2\rho)$. The gas viscosity depends on the temperature by Eq. (2.12) with reference temperature $T_{ref} = T_w = 273$K and reference viscosity μ_{ref} given by variable hard sphere (VHS) model with $\omega = 0.81$.

Since it is a low-speed flow with small temperature variance, N_{ref} = 5000 reference number of simulation particles is used. The time-averaging is starting from 1000 steps in order to reduce the statistical noises of high moments quantities, such as the temperature. The CFL number is set to be 0.95, and the least square reconstruction with Venkatakrishnan limiter is employed for the gradient calculation. Physical space parallelization with 48 cores is adopted for UGKWP.

In the dugksFoam simulation, the three-dimensional velocity space is discredited using 28 half-range Gauss-Hermit quadrature points in each direction. The CFL number is set to be 0.8. The gradients are calculated by least square method. The Prandtl number is fixed as Pr = 1.0 in DUGKS simulation to eliminate the model difference since the BGK model is used in the construction of UGKWP. The velocity space decomposition approach is adopted for dugksFoam with 48 cores on the same machine.

Figure 2.12 presented the temperature iso-surfaces predicted by UGKWP and dugksFoam. Even though the UGKWP solution exhibits strong fluctuation, the two results agree well in general. To compare the solutions more precisely, the

contours on the symmetric X-Z plane are shown in Figure 2.13, where the low order quantities between these two schemes, such as density, X and Y components of the velocity (U and V), match well. For the temperature, as a higher moment quantity, the UGKWP solutions generally agree with that of dugksFoam, but still exhibit relatively large statistical noise, although a long time averaging has been performed in UGKWP. It is also noteworthy that the noise incurred by three-dimensional particles in real three-dimensional simulation is larger than that in the two-dimensional simulation with particles without Z-direction velocity, e.g., 2D Cavity flow [89].

The computational time for dugksFoam is around 154.1 hours with 5000 iterations to reach a velocity residual of 2.4×10^{-7}. The UGKWP solution takes 93.2 hours, including 23000 steps of averaging. The total memory consumption of dugksFoam reaches 205 GB, whereas UGKWP is 70.1 GB. For the low-speed flow calculation in the transition regime, the UGKWP method is as expensive as the explicit DUGKS. However, as the Knudsen number decreases further to the continuum regime, the computational cost of UGKWP method approaches to the gas-kinetic scheme (GKS) [63] for the Navier-Stokes solutions, which has the similar efficiency as a standard NS solver and is much more efficient and less memory consumption than that of dugksFoam. What's more, the low variance technique used in DSMC [104, 47] can be adopted in the UGKWP method to improve its efficiency for the low speed flow simulations.

2.4.3 Flow Passing a Cube

Supersonic Flow in Rarefied Regime

The first case is a supersonic rarefied gas flow passing through a cube at Ma = 2 and Kn = 1. The cube center is located at $(0, 0, 0)$, and the cube volume is 1m^3.

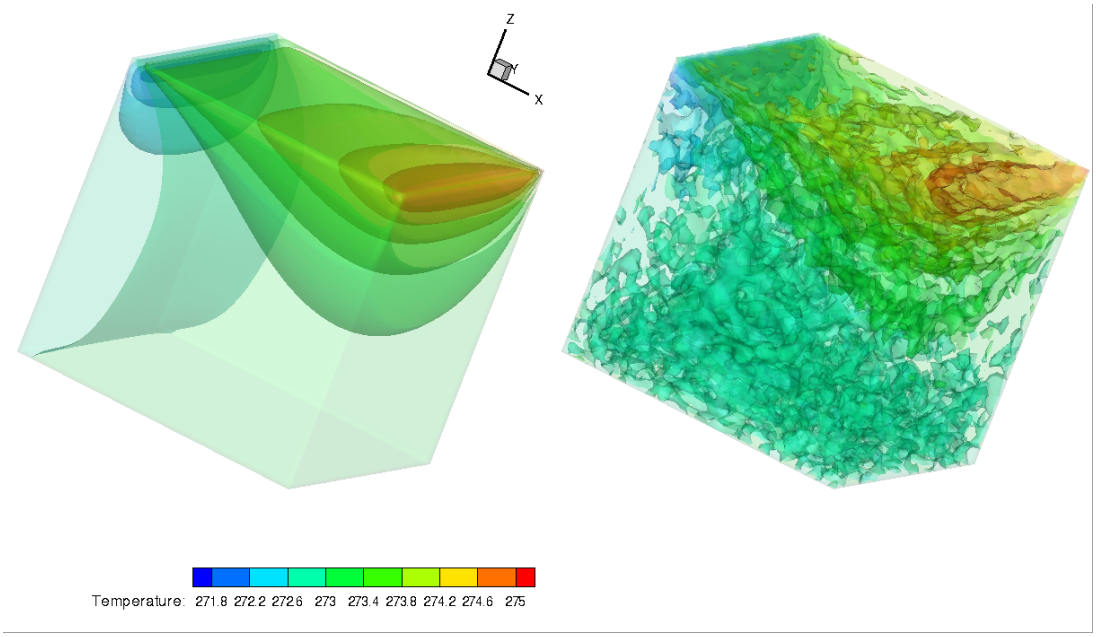

Figure 2.12: Comparison of the temperature iso-surfaces predicted by DUGKS (left) and UGKWP (right).

The surfaces of the cube are diffusive wall boundary condition with a constant temperature $T_w = 273$K. Due to the symmetry, only a quadrant of the cube is simulated by UGKWP. The computational domain $[-6, 8] \times [0, 8] \times [0, 8]$ is discretized by $(32 + 14 + 34) \times (7 + 34) \times (7 + 34) = 80 \times 41 \times 41$ cells with uniformly distributed grids on the surface of the cube. The cell size is stretched from the cube surface with a ratio of 1.0764 up to the front side and a ratio of 1.083 at the rear and lateral sides of the cube. The inflow is monatomic argon gas with molecular mass $m = 6.63 \times 10^{-26}$kg and diameter $d = 4.17 \times 10^{-10}$m. The CFL number for UGKWP simulation is 0.9, and the reference viscosity is given by the variable hard sphere (VHS) model with $\omega = 0.81$. To capture the lowest temperature that appears at the rear of the cube caused by the expanding flow, a large number of particles $N_{ref} = N_{min} = 5000$ is required. The simulation is carried out with first-order spatial accuracy to reduce the noises caused by unreliable wave reconstruction. The time-averaging starts from 1400 steps with an initial field computed by 1000 steps GKS. The simulation runs 120.8 hours

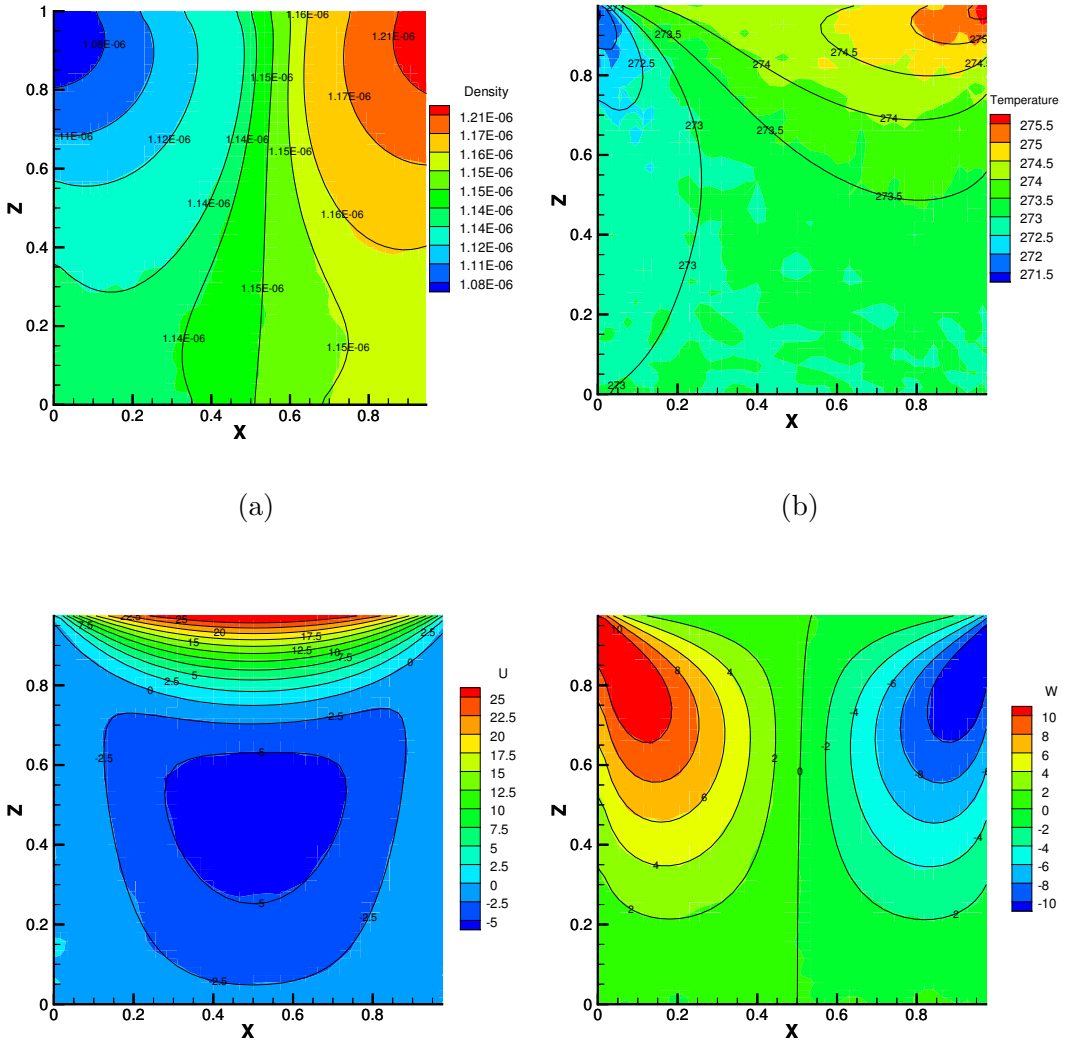

(a) (b)

(c) (d)

Figure 2.13: Symmetric X-Z cut-plane contour of cavity flow at Kn = 0.075. Background: UGKWP; Black lines with label: dugksFoam. (a) Density contour, (b) Temperature contour, (c) U-velocity contour, (d) W-velocity contour.

with 48 cores and consumes 183 GB memory, including 8600 steps of averaging.

Figure 2.14 presents the temperature, density, and velocities distributions on the X-Z symmetry plane [105] which are compared with the benchmark DSMC result of dsmcFoam [55]. Similar to UGKWP simulation, a quadrant of the cube is simulated in DSMC with a much finer physical grid of $191 \times 91 \times 91$. Each cell has 50 particles on average, and the time step is $2.0 \times 10^{-7}s$. The averaging begins from 1000 steps and continues for 68000 steps, which take 128.5 hours on 128 CPU cores (Xeon E5-2680v3 (Haswell) @2.5 GHz). The results have a satisfactory agreement overall, especially the flow field near the cube wall. However, regarding temperature contour, visible differences can be observed at the front of the bow shock and at the rear part of the cube. The differences come from different kinetic models in UGKWP and DSMC. The UGKWP uses the BGK model and the DSMC solves the full Boltzmann collision term.

Another notable point is that UGKWP requests at least 5000 particles per cell in the rear part of the cube to get the temperature field at such a low-density region. In contrast, to use roughly 500 particles per cell in UGKWP is enough to capture the nonequilibrium shock structure in front of the cube. The reason is that when $\tau \gg \Delta t$, the mass portion of collisionless particle increases, and the stochastic noise becomes significant. Instead of choosing collision pairs in DSMC, UGKWP re-sample the collisional particles according to the cell averaged temperature and macroscopic velocity. When the temperature has a small variance, such as in the low-speed cavity flow, the inadequate particle number could deteriorate the temperature with noise. Then, the re-sampled collisional particles inherit the inaccuracy and poison the low-temperature distribution at the rear part of the cube, where artificial heating with over-estimated temperature appears. Even with the above weakness, UGKWP can perform simulation on a coarse mesh than that used in the DSMC. Consequently, UGKWP and DSMC have comparable computational cost in the rarefied regime.

In DVM method [105], the implicit discretization with memory reduction technique on GPU is implemented. The full cube is simulated with a physical grid $191 \times 181 \times 181$ and a velocity grid 48^3. The velocity points are distributed uniformly to cover a range of $[-4\sqrt{2RT_w}, 4\sqrt{2RT_w}]^3$, and the trapezoidal rule is used to calculate the moments. The simulation takes approximately 20 hours, with 41 iteration steps on the Tesla K40 GPU. Figure 2.15 shows the detailed comparisons of the temperature, density, and velocities distributions on the X-Z symmetry plane with DVM solutions. Similar to the comparison with DSMC, the shock thickness and the separation distance between the density and temperature profiles have small variations between UGKWP and implicit DVM solutions, where the Shakhov model is used in DVM. Again, the UGKWP uses the BGK model. The differences in the shock structure solution between the BGK and Shakhov model have been presented in [106]. For computational time, owing to the implicit treatment and implementation of GPU acceleration, the DVM simulation is around an order faster than the current UGKWP simulation at such a low Mach number (Ma = 2) simulation.

Like UGKS [69], more realistic models, such as the Shakhov and the full Boltzmann collision term, can be used in the construction of the UGKWP method via importance sampling [102]. The research in this direction is under investigation. The preliminary result for incorporating the Shakhov model into the UGKWP method is shown in Fig. 2.16, which shows the temperature distributions on the X-Z symmetry plane at $\Pr = 2/3$ with the comparison of the benchmark DSMC result and the implicit DVM solution. Even though both UGKWP and DVM are based on an identical relaxation model, UGKWP solution matches much better with the result of DSMC than DVM. This surprising phenomenon is mainly due to the particle nature of the UGKWP method in the rarefied regime.

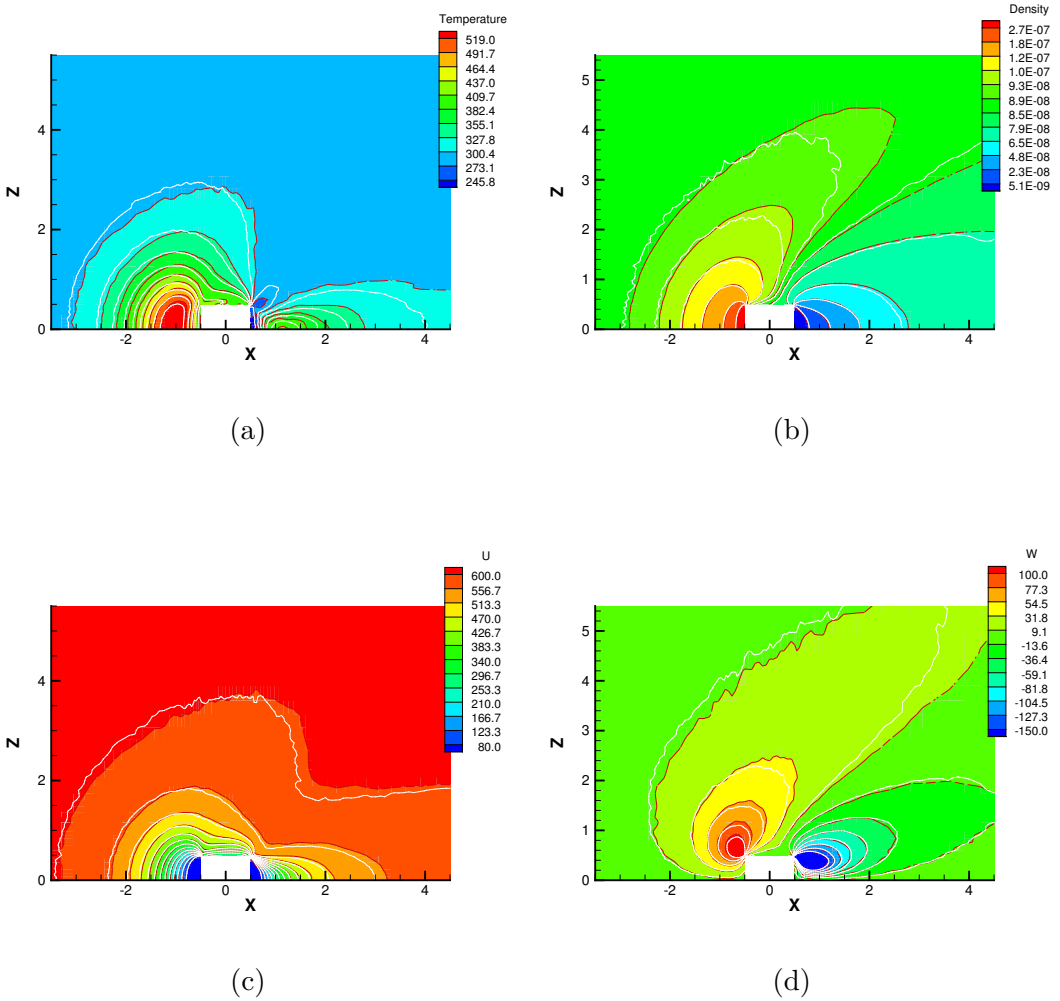

Figure 2.14: Comparison of distributions between UGKWP and DSMC on the X-Z symmetric cut-plane at Ma = 2 and Kn = 1. Dashed red lines with colored background represent the UGKWP result, and the solid white lines denote the DSMC solution. (a) temperature contour, (b) density contour, (c) contour of U (X-component velocity) and (d) contour of W (Z-component velocity).

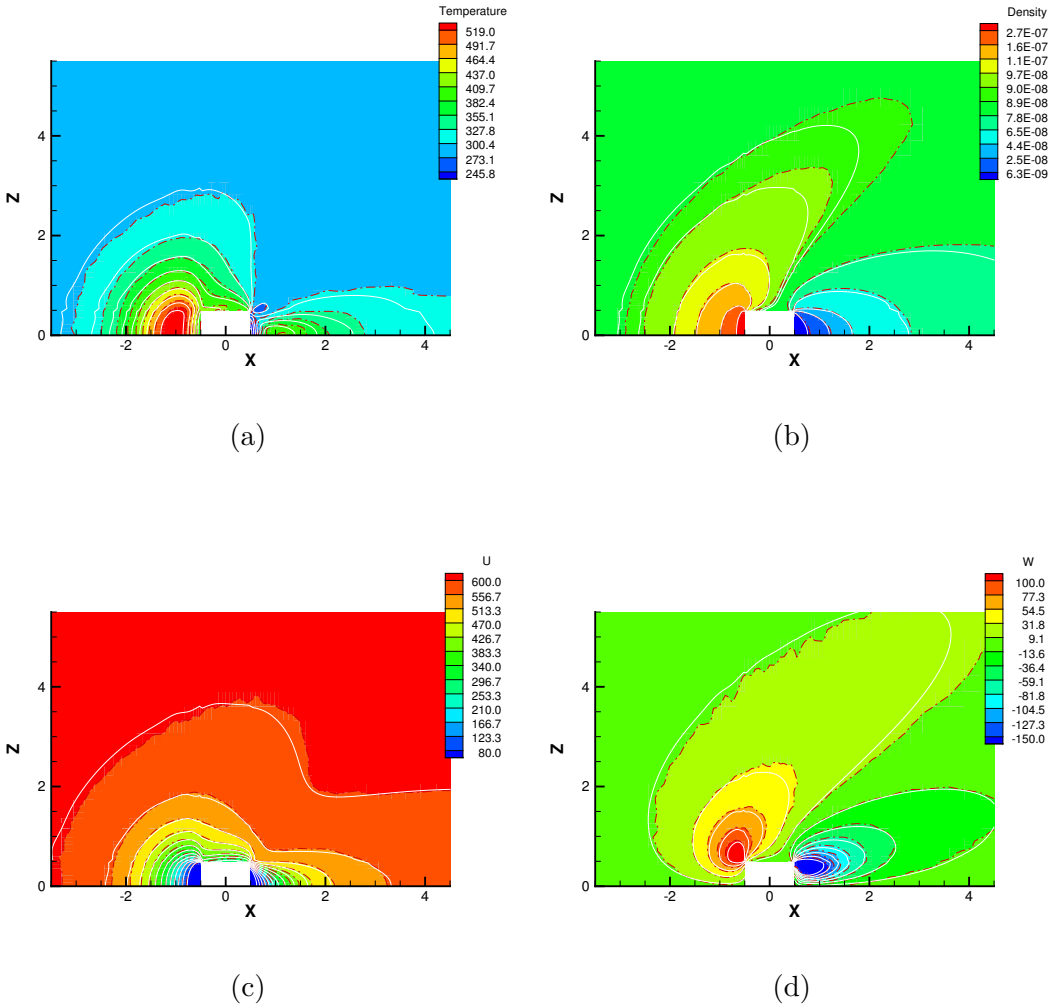

(a) (b)

(c) (d)

Figure 2.15: Comparison of distributions between UGKWP and DVM on the X-Z symmetric cut-plane at Ma = 2 and Kn = 1. Dashed red lines with colored background represent the UGKWP result, and the solid white lines denote the DVM solution. (a) temperature contour, (b) density contour, (c) contour of U (X-component velocity) and (d) contour of W (Z-component velocity).

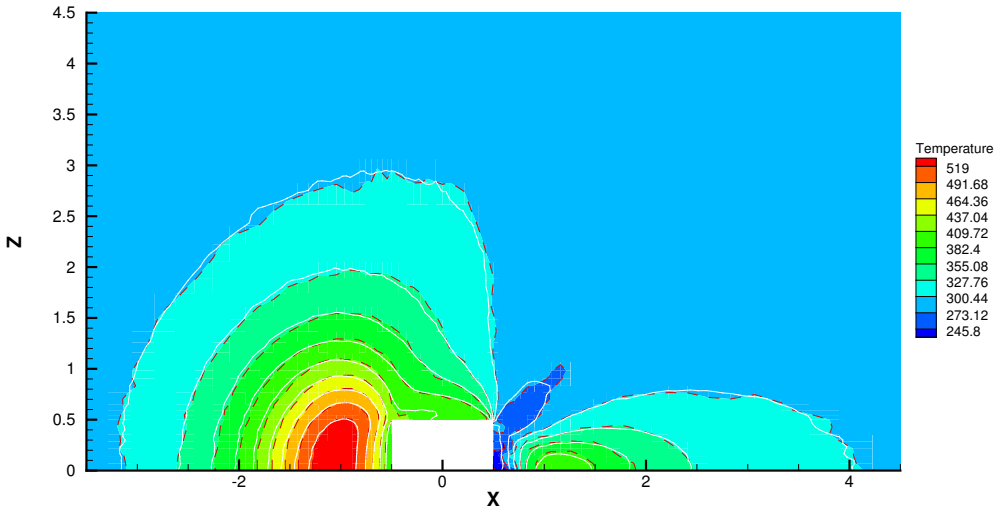

(a)

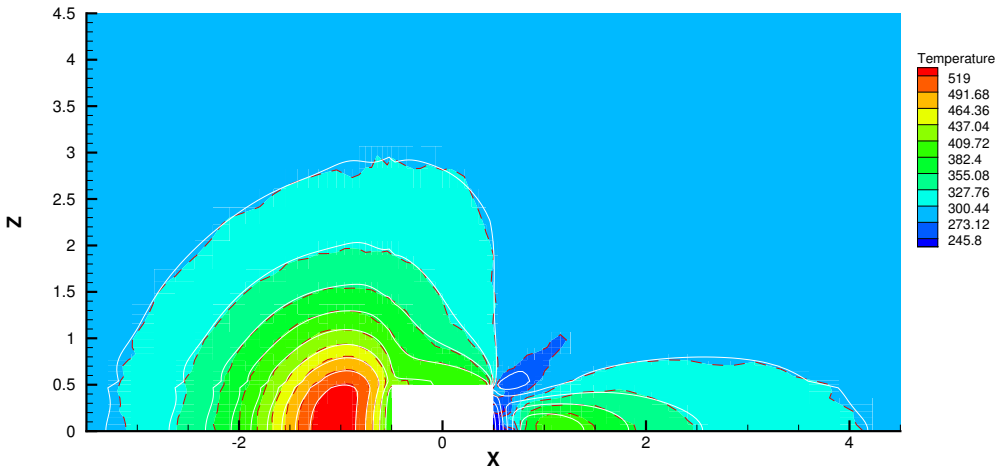

(b)

Figure 2.16: Temperature distribution on the X-Z symmetric cut-plane at Ma = 2 and Kn = 1 with Prandtl number Pr = 2/3. Dashed red lines with colored background represent the UGKWP result, and the solid white lines denote the (a) DSMC solution, (b) DVM solution.

Hypersonic Flow in Transition Regime

To highlight the efficiency and capability of UGKWP, hypersonic flow at Ma = 20 is simulated in the transition regime (Kn = 0.05). All the parameters are the same as the previous case except the inflow temperature 5K and the wall temperature 300K. The cube is contained in a volume with base and top side lengths of $a = 16\text{m}, b = 10\text{m}$, and height $h = 14\text{m}$.

As shown in Figure 2.17, a unstructured mesh with total 420702 cells is generated, which is composed of 8305 hexahedra, 52 prisms, 25030 pyramids and 387315 tetrahedra with a minimum cell height 0.0248m near the cube wall. Distinguishable from the rarefied case, the number of particles required drops dramatically. Here, the reference and minimum number of particles per cell $N_{ref} = N_{min} = 400$ are used. The simulation is conducted with the least square reconstruction and Barth and Jespersen limiter. An initial field is firstly computed with 5000 steps by GKS, and after 8000 steps of UGKWP calculation the time averaging of the flow field starts for the steady-state solution. The simulation runs 59.9 hours with 48 cores and consumes 68.1 GB memory, including 7000 steps of averaging.

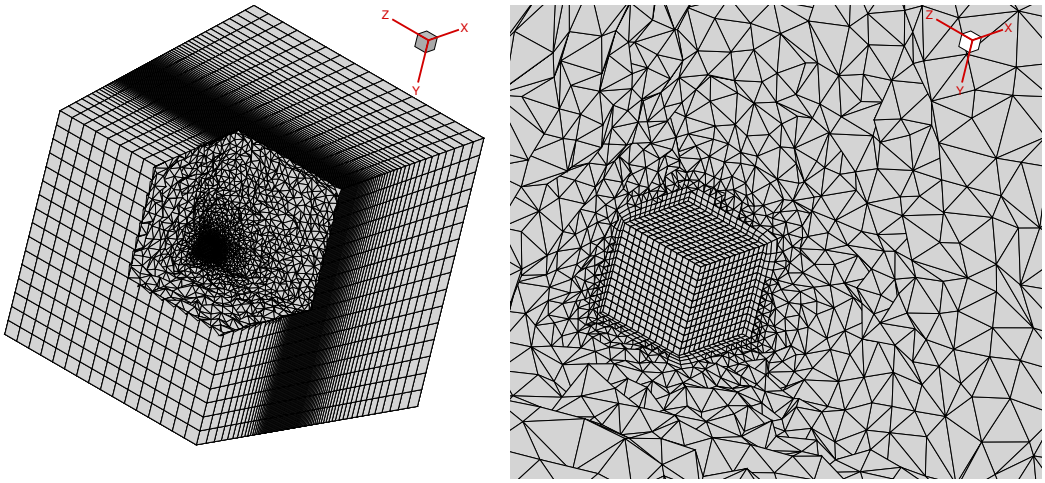

(a) (b)

Figure 2.17: Unstructured mesh configuration at Ma = 20 and Kn = 0.05 (a) Full view and (b) local enlargement

Figure 2.18 shows the distributions of temperature, density, and velocities on the X-Z symmetry plane. The hypersonic flow computation in the transition regime is a challenge for both stochastic and deterministic methods. For the DSMC, an extremely fine mesh in physical space is required. For the DVM-type deterministic solvers, a tremendous amount of discrete velocity points becomes necessary. The UGKWP is an idealized method for the hypersonic flow in all flow regimes. Due to the high Mach number, even with a low inflow temperature of 56K, the maximum temperature inside the shock region can get to 6500K and over. In the future, the physics associated with high temperature, such as ionization and chemical reaction, will be added in UGKWP.

To further illustrate the multiscale nature of the simulation, the local Knudsen number [107] based on the gradient $\mathrm{Kn}_{GLL} = l|\nabla\rho|/\rho$ for the above two cases are presented in Fig. 2.19, which presents five orders of magnitude difference.

The decline of parallel efficiency in the rarefied regime, as presented in Section 2.3.2, can be visualized through the averaged number of particles per cell in the simulation. Figure 2.20 shows the distribution of normalized particle number per cell N/N_{ref} on symmetric X-Z cut-plane at $\mathrm{Ma} = 2, Kn = 1$ and $\mathrm{Ma} = 20, Kn = 0.05$. The probability of particle collision in the cell becomes lower with the increment of $\tau/\Delta t$. Therefore, the particles tend to keep free streaming and concentrate in the rearward of the computational domain, especially in the cell with a large volume. This mechanism causes an imbalance in the distributions of particles across different CPU cores. Nevertheless, this problem can be mitigated by implementing dynamic load balancing as used in the DSMC implementation.

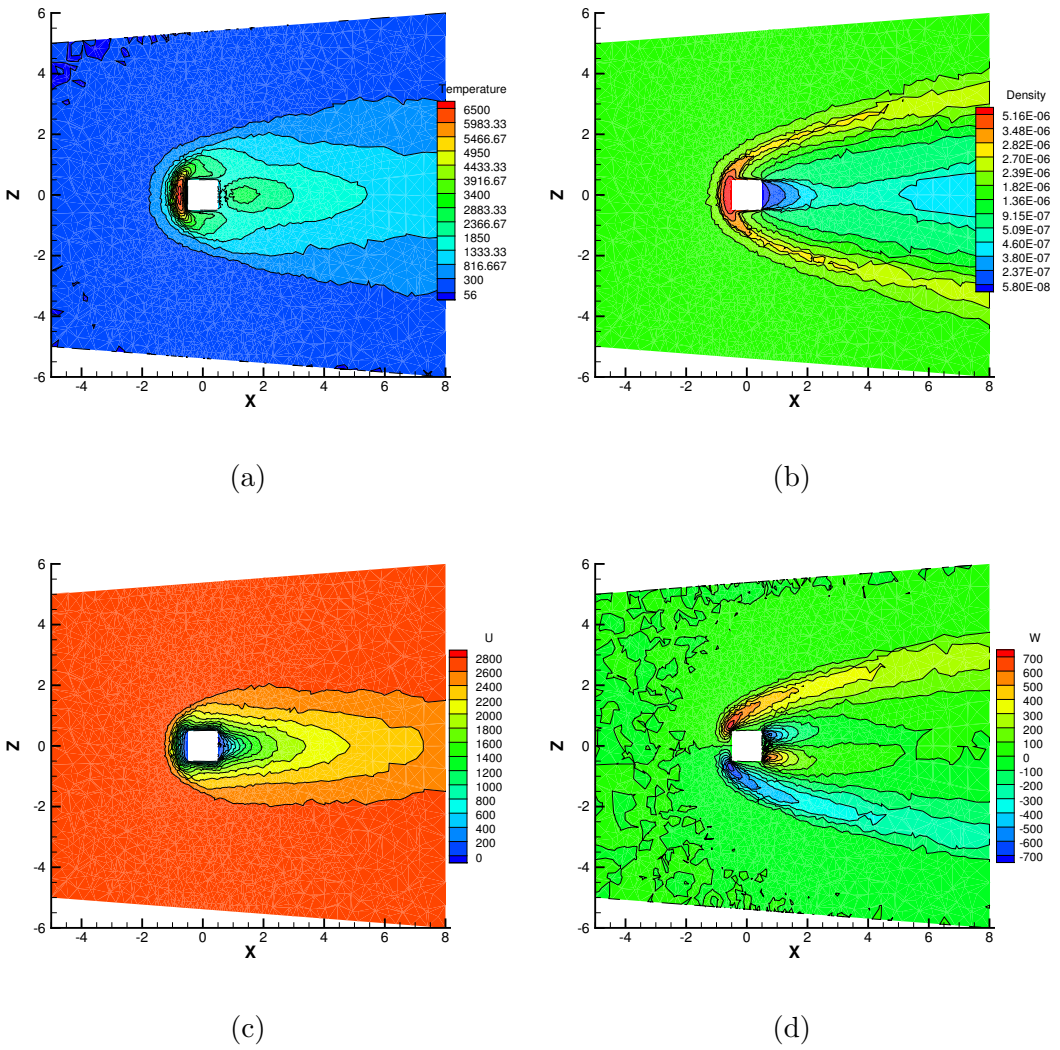

(a) (b)

(c) (d)

Figure 2.18: Symmetric X-Z cut-plane contour of various flow fields at at Ma = 20 and Kn = 0.05. (a) temperature contour, (b) density contour, (c) contour of U (X-component velocity) and (d) contour of W (Z-component velocity).

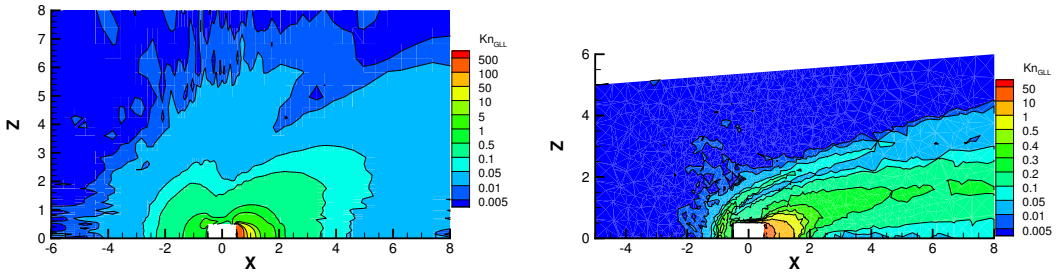

(a) (b)

Figure 2.19: Local Knudsen number contour on symmetric X-Z cut-plane at (a)Ma = 2 and Kn = 1 and (b)Ma = 20 and Kn = 0.05

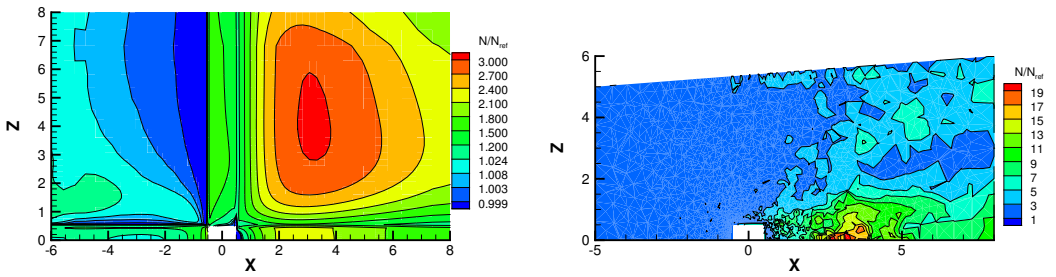

(a) (b)

Figure 2.20: Distribution of normalized particle number per cell on symmetric X-Z cut-plane at (a)Ma = 2 and Kn = 1 and (b)Ma = 20 and Kn = 0.05

2.4.4 Hypersonic Flow over a Space Vehicle

The last example is hypersonic flow at Mach numbers 6 and 10 over a space vehicle in the transition regimes Kn $= 10^{-3}$. This case shows the efficiency and capability of UGKWP for simulating three-dimension hypersonic flow over complex geometry configuration. The angle of attack is 20° degrees in this case. As seen in Fig. 2.21, the unstructured mesh of 560593 cells consists of 15277 pyramids and 545316 tetrahedra with minimum cell height $0.001L$ near the front of the vehicle surface. The reference length for the definition of Knudsen number is $L = 0.28$m. The boundary condition on the vehicle surface is a diffusive one, on which the temperature maintains at $T_w = 300$K. Due to the symmetry, only half of the vehicle is simulated. The inflow is monatomic argon gas with molecular mass $m = 6.63 \times 10^{-26}$kg and diameter $d = 4.17 \times 10^{-10}$m at $T_\infty = 300$K. The CFL number for the simulation is 0.95, and the reference viscosity is given by the variable hard sphere (VHS) model with $\omega = 0.81$. The least square reconstruction with Venkatakrishnan limiter is used in the simulation.

Figure 2.22 presents the distribution of temperature, heat flux, pressure, local Knudsen number, and streamlines around the vehicle at Mach number 6. Figure 2.23 shows the solutions at Mach number 10. Even the free-stream Knudsen number is relatively small, no vortex flow is observed in the rear part of the vehicle, see Figs. 2.22d and 2.23d, which is observed in the simulation of near continuum flow [6]. Meanwhile, from Figs. 2.22c and 2.23c, the density-based local Knudsen number Kn_{GLL} can cover a wide range of values with five orders of magnitude difference. Therefore, a multi-scale method, like UGKWP, is necessary to capture the flow physics in different regimes correctly. As presented in Figs. 2.22a and 2.23a, a high-temperature region is detected at the leeward side despite the low intensity of heat exchange upon vehicle surface. This is mainly caused by particle collisions in the strong recompression region with a relatively low free-stream Knudsen number.

As for the computational cost, for the Ma = 6 case, the initial field is obtained by GKS with 6000 local time stepping, and the time-averaging starts after 12000 steps of UGKWP computation. The simulation runs 24.87 hours with 48 cores and consumes 35 GB memory, including 8000 steps of averaging. For the case of Ma = 10, $N_{ref} = N_{min} = 400$ particles is used. The simulation is conducted on Tianhe-2 with 8 nodes or 192 cores, and it takes 22.8 hours, including 5000 steps GKS calculation with local time stepping for the initial field, and 9000 steps of time averaging after 10000 steps UGKWP calculation for the steady-state solution.

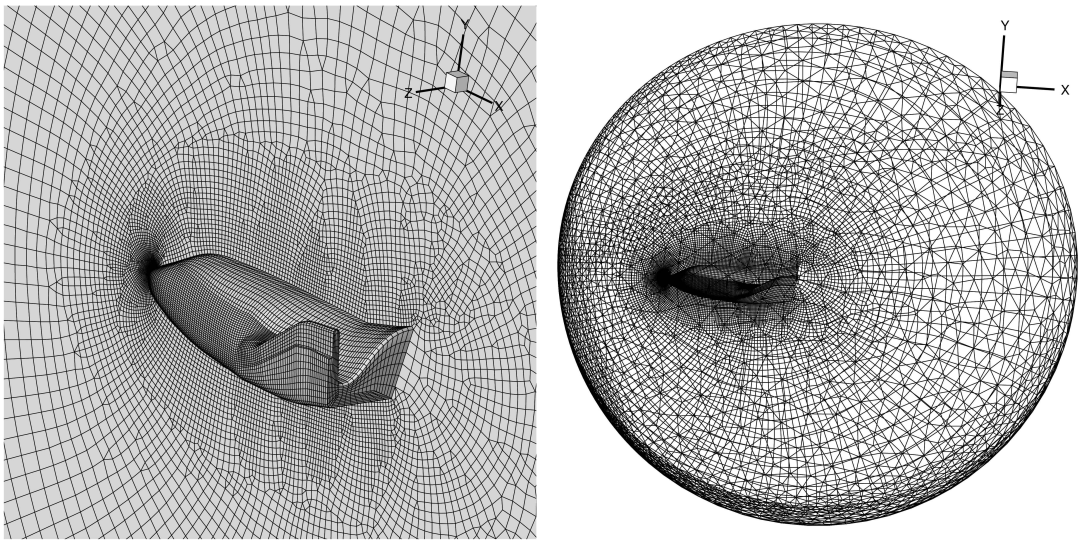

(a) (b)

Figure 2.21: Surface mesh of space vehicle (a) local enlargement, (b) global view

2.5 Conclusion

In this chapter, a unified gas-kinetic wave-particle (UGKWP) method is constructed on three-dimensional unstructured mesh with parallel computing on supercomputer. The scheme is validated for flow simulation of monatomic gas in both continuum and rarefied regimes at different flow speeds. Compared with

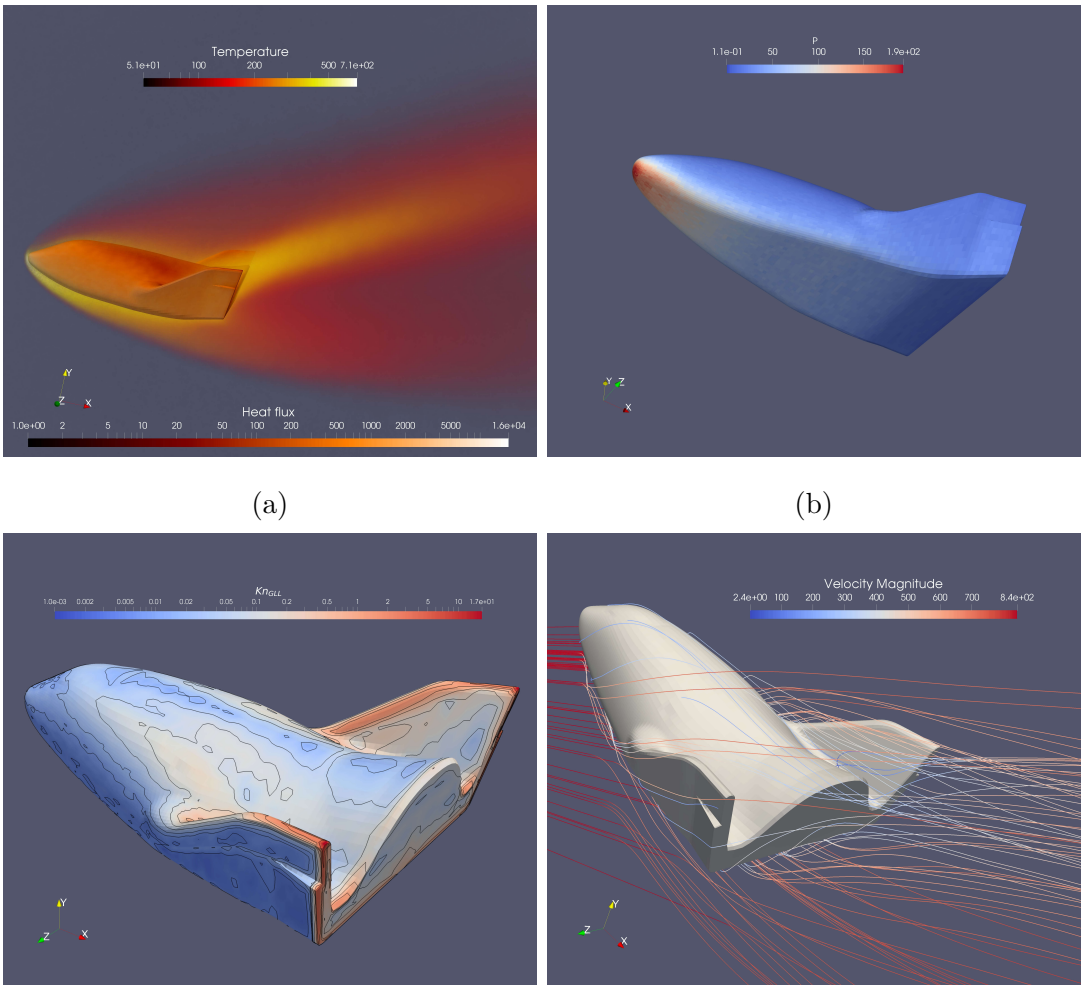

(a) (b)

(c) (d)

Figure 2.22: Space vehicle at Ma = 6 and Kn = 10^{-3}. (a) Temperature and surface distribution of heat flux, (b) Pressure distribution, (c) Kundsen number distribution, (d) Streamlines color by magnitude of velocity.

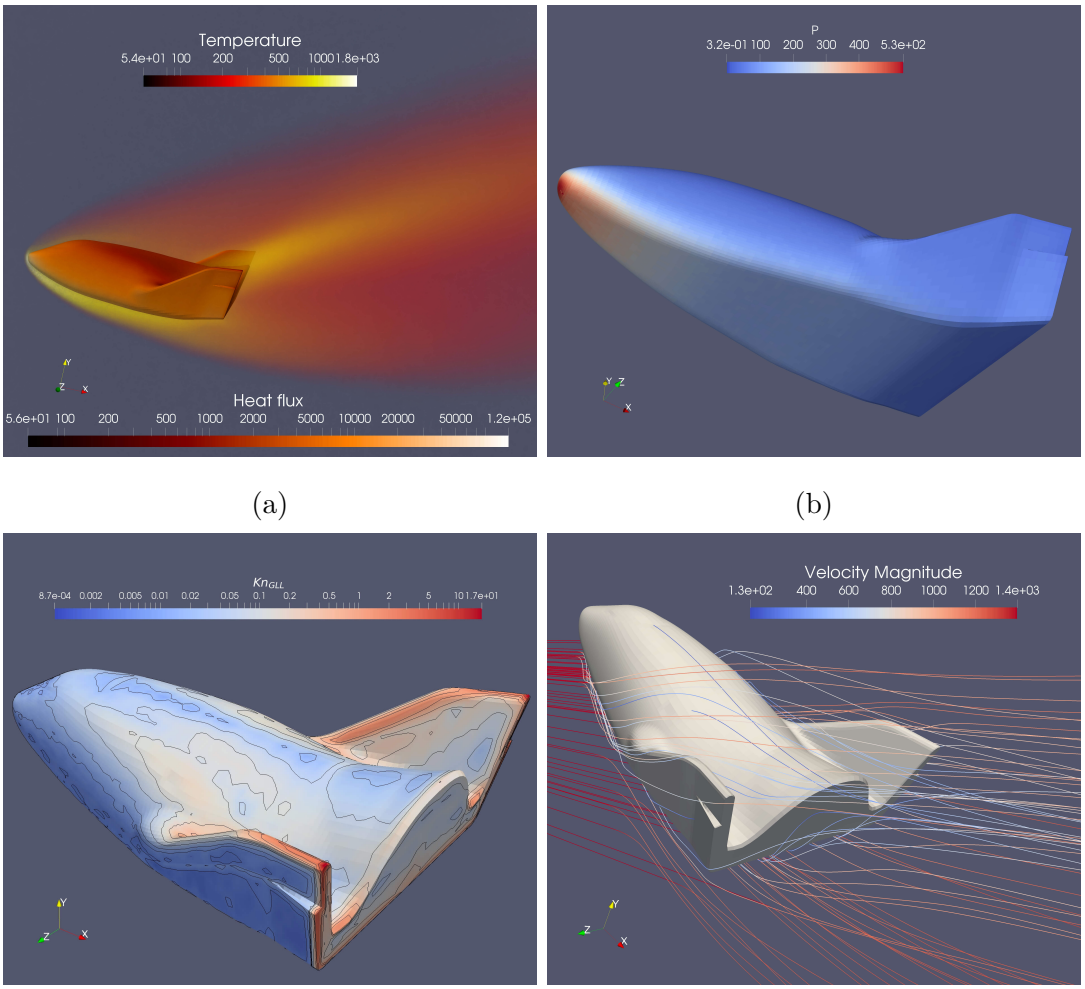

(a) (b)

(c) (d)

Figure 2.23: Space vehicle at Ma = 10 and Kn = 10^{-3}. (a) Temperature and surface distribution of heat flux, (b) Pressure distribution, (c) Kundsen number distribution, (d) Streamlines color by magnitude of velocity.

other popular flow solvers, such as the DSMC method and the deterministic DVM-based Boltzmann solver, the UGKWP has multiscale property and is efficient in simulating 3D supersonic/hypersonic flow, especially in the transition and near continuum flow regime.

Chapter 3

Unified Gas-kinetic Wave-particle Method for Diatomic Molecular Flow

This chapter is about to construct UGKWP method for diatomic gas. The Rykov kinetic model will be used in the construction of the evolution solution of the gas distribution function, which controls the distributions of particle and wave and the rate of energy exchange between translational and rotational modes. A simple and efficient way to set up the correct transport coefficients is presented in this chapter. A weighted method is applied to sample the particles from a modified distribution function of the Rykov model. The overall UGKWP method for diatomic gas is very efficient and has excellent performance for high speed flow simulation with the translational and rotational non-equilibrium.

The rest of the chapter is organised as follows. In Section 3.1, the Rykov kinetic model will be introduced first. Then, the unified gas-kinetic wave-particle method will be presented in Section 3.2. The asymptotic preserving property of the UGKWP method for diatomic gas in the continuum regime will be intro-

duced in Section 3.3. Section 3.4 includes various numerical tests to validate the scheme. Section 3.5 is the conclusion.

3.1 Diatomic Molecule and Rykov Model

As hypersonic spacecraft flying at a high altitude, the temperature at the stagnation point can over thousand Kelvin. At such high stagnation temperature, the non-equilibrium exchange of internal energy (transnational, rotational, vibrational and electronic energy) of diatomic molecule cannot be neglected. All of these energy modes affect the partition functions and hence the thermodynamic properties.

Proceed from the Schrodinger equation, for the simplest rigid rotator model and harmonic oscillator model representing the rotation and vibration of the molecule, the discrete energies $\varepsilon_{r,J}$ and $\varepsilon_{v,n}$ can be attained

$$\varepsilon_{r,J} = J(J+1)k_B\Theta_r,\ J = 0, 1, 2, \ldots \quad \text{Rigid rotator} \tag{3.1}$$

$$\varepsilon_{v,n} = (\frac{1}{n} + 1)k_B\Theta_v,\ n = 0, 1, 2, \ldots \quad \text{Harmonic oscillator} \tag{3.2}$$

where J and n are the quantum number of rotation and vibration, respectively. In the above equations, Θ_r and Θ_v are introduced as the characteristic temperature of rotation and vibration, respectively, which describe the quantum energy levels of molecules.

For N_2, NO and O_2, the characteristic temperatures of rotation have the values in the range of only several Kelvin: Θ_r = 2.88K, 2.44K, 2.07K; and their characteristic temperatures of vibration are: Θ_v = 3371K, 2719K, 2256K [108].

For these molecules, Θ_r is three orders of magnitude smaller than Θ_v. For most diatomic molecules at normal temperature, Θ_r is small enough and quantum effects can be ignored, although hydrogen, H_2 is an exceptional case[95].

Since Earth's atmosphere is composed mostly of diatomic molecules (about 78% nitrogen, 21% oxygen), and the temperatures range of aerospace applications is 300K $\leq T \leq$ 2000K, the effects of rotation are more important than those for vibrational energy modes. Moreover, for the temperature of a few thousand Kelvin at the most, for both oxygen and nitrogen atoms, almost all particles lie in their electronic ground state and the partition function is simply a constant. Thus, there is no participation in thermodynamics from the electronic mode.

In summary, at moderate temperature, both translational ($K_t = 3$) and rotational mode ($K_r = 2$) are fully excited and treated in classical statistical mechanics. The quantized vibrational mode ($0 \leq K_v \leq 2$) is forzen at low temperature and its contribution to the internal energy and specific heats can be neglected. Therefore, only the translational and rotational degrees of freedom will be considered for diatomic molecule in this chapter.

Similar to monatomic gas, the state of the diatomic gas can be described by the particle velocity distribution function $f(t, \mathbf{x}, \mathbf{u}, \epsilon_r)$, where $\mathbf{x}$ is the spatial coordinate, t is the time, $\mathbf{u}$ is the molecular translational velocity, and ϵ_r is the rotational energy of molecule. The relations between distribution function and macroscopic variables $\mathbf{W} = (\rho, \rho\mathbf{U}, \rho E, \rho E_r)$ are defined as

$$\mathbf{W} = \int \boldsymbol{\psi} f \, \mathrm{d}\Xi,$$

where $\boldsymbol{\psi} = \left(1, \mathbf{u}, \frac{1}{2}(\mathbf{u}^2 + \frac{2\epsilon_r}{m}), \frac{\epsilon_r}{m}\right)$ is the vector for the moments of distribution function and ρE_r is the rotational energy density.

Different from monatomic gas, the evolution of the diatomic gas distribution function f cannot be simply characterized by Boltzmann Equation (2.1) for monatomic gas due to the inelastic nature of collision. However, the phenomenological Rykov model [109] and its generalized model [110] with the inclusion of Boltzmann collision term can be served as a relaxation model for the description of energy exchange.

In this chapter, instead of using the Wang Chang-Uhlenbeck (WCU) equation [111] for the semiclassical treatment of internal energy with discrete values, the Rykov kinetic model is used

$$\frac{\partial f}{\partial t} + \mathbf{u} \cdot \nabla_{\mathbf{x}} f = \underbrace{\frac{\tilde{g}_t - f}{\tau_t}}_{\textbf{Elastic}} + \underbrace{\frac{\tilde{g}_r - f}{\tau_r}}_{\textbf{Inelastic}}, \tag{3.3}$$

where the collision operator on the right-hand side consists of two components, corresponding to elastic and inelastic collisions. τ_t and τ_r are relaxation times of translational and rotational mode, respectively, which are independent of the molecular rotational energy.

Therefore, the overall relaxation time τ

$$\frac{1}{\tau_t} + \frac{1}{\tau_r} = \frac{1}{\tau} = \frac{p_t}{\mu(T_t)} = \frac{\rho R T_t}{\mu(T_t)} \tag{3.4}$$

depends on the translational temperature T_t for colliding particles, not on the equilibrium temperature T_{eq}. $\mu(T_t)$ is the dynamic viscosity of diatomic gas. Moreover, the rotational collision number is defined as $Z_r = \tau_r/\tau$, which is a function of translational and rotational temperature and indicates the number of collisions needed for the full rational-translational energy exchange.

Hence, the collision term of Rykov model can be rewritten as

$$\frac{\partial f}{\partial t} + \mathbf{u} \cdot \nabla_{\mathbf{x}} f = \frac{\tilde{g}_t - f}{\tau} + \frac{\tilde{g}_r - \tilde{g}_t}{Z_r \tau}, \tag{3.5}$$

where $\tilde{g}_t$ is the modified equilibrium distribution function for the elastic collision.

Similar to the Shakhov model, we expand $\tilde{g}_t$ about the equilibrium state for translation mode in series of orthogonal polynomials in the peculiar velocity $\mathbf{c}$

$$\begin{aligned}
&\tilde{g}_t = g_t + g_t^+, \\
&g_t = \rho \left(\frac{\lambda_t}{\pi}\right)^{\frac{3}{2}} e^{-\lambda_t \mathbf{c}^2} \frac{2\lambda_r}{m} e^{-\lambda_r \frac{2\epsilon_r}{m}}, \\
&g_t^+ = g_t \left((1 - \mathrm{Pr}) \frac{4\lambda_t^2 \mathbf{q}_t \cdot \mathbf{c}}{5\rho} \left(2\lambda_t \mathbf{c}^2 - 5\right) + (1 - \delta) \frac{4\lambda_t \lambda_r \mathbf{q}_r \cdot \mathbf{c}}{\rho} \left(\lambda_r \frac{2\epsilon_r}{m} - 1\right) \right),
\end{aligned} \tag{3.6}$$

and in the absence of external electric and magnetic fields that capable of producing a significant dominant orientation of the angular momentum of the molecules, the modified equilibrium distribution function for inelastic collision $\tilde{g}_r$ has the form

$$\begin{aligned}
&\tilde{g}_r = g_r + g_r^+, \\
&g_r = \rho \left(\frac{\lambda_{eq}}{\pi}\right)^{\frac{3}{2}} e^{-\lambda_{eq}\mathbf{c}^2} \frac{2\lambda_{eq}}{m} e^{-\lambda_{eq}\frac{2\epsilon_r}{m}}, \\
&g_r^+ = g_r \left(\omega_0(1-\mathrm{Pr})\frac{4\lambda_{eq}^2 \mathbf{q}_t \cdot \mathbf{c}}{5\rho}\left(2\lambda_{eq}\mathbf{c}^2 - 5\right) + \omega_1(1-\delta)\frac{4\lambda_{eq}^2 \mathbf{q}_r \cdot \mathbf{c}}{\rho}\left(\lambda_{eq}\frac{2\epsilon_r}{m} - 1\right)\right),
\end{aligned} \tag{3.7}$$

where $\lambda_{t,r,eq} = 1/(2RT_{t,r,eq})$, the subscript t, r, eq in $T_{t,r,eq}$ represent translational, rotational and equilibrium temperature, respectively. The parameter $\delta = \mu(T_t)/(\rho D)$ depends on the molecular potential with D as gas self-diffusion coefficient. ω_0 and ω_1 are set to have proper relaxation of heat flux in Eq. (3.19). In this chapter, these coefficients adopt the values $\delta = 1/1.55$, $\omega_0 = 0.2354$, $\omega_1 = 0.3049$ for nitrogen [78].

The stress tensor $\mathbf{P}$, and the heat fluxes $\mathbf{q}_t$ and $\mathbf{q}_r$ for the transfer of random translational and rotational energies, can be calculated by f as,

$$\begin{aligned}
\mathbf{P} &= \int \mathbf{c} \otimes \mathbf{c} f \, \mathrm{d}\Xi, \\
\mathbf{q}_t &= \frac{1}{2}\int \mathbf{c}\mathbf{c}^2 f \, \mathrm{d}\Xi, \\
\mathbf{q}_r &= \frac{1}{2}\int \mathbf{c}\frac{2\epsilon_r}{m} f \, \mathrm{d}\Xi,
\end{aligned}$$

with $\mathrm{d}\Xi = \mathrm{d}\mathbf{u}\,\mathrm{d}\epsilon_r$.

The total heat flux $\mathbf{q}$ is the sum of $\mathbf{q}_t$ and $\mathbf{q}_r$,

$$\mathbf{q} = \int \frac{1}{2}\mathbf{c}\left(\mathbf{c}^2 + \frac{2\epsilon_r}{m}\right) f \, \mathrm{d}\Xi = \mathbf{q}_t + \mathbf{q}_r.$$

3.2 Unified Gas-kinetic Wave-particle Method for Diatomic Gas

3.2.1 General Framework of the UGKWP method

The Rykov model kinetic equation can be rewritten in a more convenient form,

$$\frac{\partial f}{\partial t} + \mathbf{u} \cdot \nabla_{\mathbf{x}} f = \frac{g^* - f}{\tau}, \tag{3.8}$$

where g^* is defined as the convex combination of two modified equilibrium distribution functions

$$g^* = (1 - \frac{1}{Z_r})\tilde{g}_t + \frac{1}{Z_r}\tilde{g}_r \tag{3.9}$$

Now the Rykov kinetic model has the relaxation form same as BGK model with a different equilibrium distribution function. Assuming a local constant relaxation time τ, the integral solution of Eq. (3.8) can be written as,

$$f(t, \mathbf{x}, \mathbf{u}, \epsilon_r) = \frac{1}{\tau}\int_0^t e^{-(t-t')/\tau} g^*(t', \mathbf{x}', \mathbf{u}, \epsilon_r)\, \mathrm{d}t' + e^{-t/\tau} f_0(\mathbf{x} - \mathbf{u}t, \mathbf{u}, \epsilon_r), \tag{3.10}$$

where the equilibrium distribution g^* is integrated along the characteristics $\mathbf{x}' = \mathbf{x} - \mathbf{u}(t - t')$ and f_0 is the initial distribution function at $t = 0$.

The equilibrium flux term $\mathbf{F}_{ij}^{eq}$ related to the Maxwellian distribution is

$$\mathbf{F}_{ij}^{eq} \overset{\text{def}}{=} \int_0^{\Delta t} \int \frac{1}{\tau}\int_0^t e^{-(t-t')/\tau} g^*(t', \mathbf{x}', \mathbf{u}, \epsilon_r)\, \mathrm{d}t' \mathbf{u} \cdot \mathbf{n}_{ij} \boldsymbol{\psi}\, \mathrm{d}\Xi\, \mathrm{d}t, \tag{3.11}$$

and the free streaming flux terms $\mathbf{F}_{ij}^{fr}$ related to the initial distribution is

$$\mathbf{F}_{ij}^{fr} \overset{\text{def}}{=} \int_0^{\Delta t} \int e^{-t/\tau} f_0(\mathbf{x}_{ij} - \mathbf{u}t, \mathbf{u}, \epsilon_r) \mathbf{u} \cdot \mathbf{n}_{ij} \boldsymbol{\psi}\, \mathrm{d}\Xi\, \mathrm{d}t. \tag{3.12}$$

Different from Eq. (2.15) for monatomic gas, the macroscopic governing equations of $\mathbf{W}_i$ include an extra source term

$$\mathbf{W}_i^{n+1} = \mathbf{W}_i^n - \frac{1}{|\Omega_i|}\sum_{j \in N(i)} \mathbf{F}_{ij}|S_{ij}| + \mathbf{S}_i, \tag{3.13}$$

and

$$\mathbf{S} = \int_0^{\Delta t} \int \frac{g^* - f}{\tau} \boldsymbol{\psi} \, \mathrm{d}\Xi \, \mathrm{d}t = \int_{t^n}^{t^{n+1}} \mathbf{s} \, \mathrm{d}t,$$

where $\mathbf{s}$ can be expressed as

$$\mathbf{s} = \left(0, \mathbf{0}, 0, \frac{\rho E_r^{eq} - \rho E_r}{Z_r \tau}\right)^T.$$

Note that while the elastic collision conserves the translational energy, the inelastic collision exchanges the translational and rotational energy. The equilibrium rotational energy ρE_r^{eq} is determined under the assumption $T_r = T_t = T_{eq}$ such that

$$\rho E_r^{eq} = \frac{K_r \rho}{4\lambda_{eq}} \quad \text{and} \quad \lambda_{eq} = \frac{K_r + 3}{4} \frac{\rho}{\rho E - \frac{1}{2}\rho(U^2 + V^2 + W^2)}. \tag{3.14}$$

with $K_r = 2$ is the rotational degrees of freedom.

3.2.2 The Construction of Equilibrium Flux

In this subsection, the construction of the equilibrium flux $\mathbf{F}_{ij}^{eq}$ will be presented.

Recall that

$$\begin{aligned} g^* &= \tilde{g}_t + \frac{\tilde{g}_r - \tilde{g}_t}{Z_r} \\ &= g_t + \frac{g_r - g_t}{Z_r} + g_q^+, \end{aligned} \tag{3.15}$$

and

$$g_q^+ = g_t^+ + \frac{g_r^+ - g_t^+}{Z_r} \tag{3.16}$$

as the term for the heat flux correction.

A straightforward method to construct the equilibrium flux is to expand the first two terms in Eq. (3.15) around the cell interface, and this was the construction method used in the diatomic UGKS [78].

However, based on the following lemma, the calculation of the equilibrium can be simplified.

Lemma 3.2.1. *If g_t and g_r are defined as that in Eqs.* (3.6) *and* (3.7) *then we have*

$$\frac{g_r - g_t}{Z_r} = \mathcal{O}(\tau) \quad or \quad \frac{g_r - g_t}{Z_r} \ll \tau, \quad as \quad \tau \to 0.$$

Proof. Firstly, consider the case that $Z_r = \mathcal{O}(\tau^{-1})$ or $Z_r \gg \tau^{-1}$, we can obtain

$$\frac{g_r - g_t}{Z_r} = \mathcal{O}(\tau) \quad \text{or} \quad \frac{g_r - g_t}{Z_r} \ll \tau$$

Next, for the other case that $Z_r \ll \tau^{-1}$, we have $Z_r\tau^2 \ll \tau$. With the condition that $Z_r\tau \ll 1$, the leading order approximation in [112, 113] gives,

$$T_t - T_r = -\frac{2}{3} Z_r \tau T_{eq} \nabla_{\mathbf{x}} \cdot \mathbf{U} + \mathcal{O}(Z_r^2\tau^2), \tag{3.17}$$

from which $|T_{eq} - T_t|/Z_r = \mathcal{O}(\tau)$ can be estimated.

The linearized Maxwell distribution function g_t around the equilibrium temperature T_{eq} is

$$\begin{aligned} g_t =& g_r + \frac{T_t - T_{eq}}{T_{eq}} g_r \left[\left(\frac{\mathbf{c}^2}{2RT_{eq}} - \frac{3}{2} \right) - \frac{3}{K_r} \left(\frac{\epsilon_r}{k_B T_{eq}} - \frac{K_r}{2} \right) \right] + \mathcal{O}(|T_{eq} - T_t|^2) \\ =& g_r + \frac{T_t - T_{eq}}{T_{eq}} g_r \left[\left(\frac{\mathbf{c}^2}{2RT_{eq}} - \frac{3}{2} \right) - \frac{3}{K_r} \left(\frac{\epsilon_r}{k_B T_{eq}} - \frac{K_r}{2} \right) \right] + \mathcal{O}(Z_r^2\tau^2). \end{aligned}$$

Hence,

$$\frac{g_r - g_t}{Z_r} = \frac{T_t - T_{eq}}{Z_r} \frac{g_r}{T_{eq}} \left[\left(\frac{\mathbf{c}^2}{2RT_{eq}} - \frac{3}{2} \right) - \frac{3}{K_r} \left(\frac{\epsilon_r}{k_B T_{eq}} - \frac{K_r}{2} \right) \right] + \mathcal{O}(Z_r\tau^2) = \mathcal{O}(\tau)$$

□

Therefore, the second term $(g_r - g_t)/Z_r$ in Eq. (3.15) is of order τ. Since g_q^+ related to heat flux is also a high order term, only the first term of g^*, i.e., g_t, is expanded around $\mathbf{x}_{ij}$ in the calculation of the equilibrium flux.

$$\begin{aligned} g_t(t, \mathbf{x}, \mathbf{u}, \epsilon_r) =& g_t(t^n, \mathbf{x}_{ij}, \mathbf{u}, \epsilon_r) + \nabla_{\mathbf{x}} g_t(t^n, \mathbf{x}_{ij}, \mathbf{u}, \epsilon_r) \cdot \bar{\mathbf{x}} + \partial_t g_t(t^n, \mathbf{x}_{ij}, \mathbf{u}, \epsilon_r)(t - t^n) \\ =& g_t(t^n, \mathbf{x}_{ij}, \mathbf{u}, \epsilon_r) \left[1 + a\bar{x} + b\bar{y} + c\bar{z} + A(t - t^n) \right], \end{aligned} \tag{3.18}$$

where $\bar{\mathbf{x}} = (\bar{x}, \bar{y}, \bar{z})$, $\bar{x} = x - x_{ij}$, $\bar{y} = y - y_{ij}$, and $\bar{z} = z - z_{ij}$.

The derivative terms in g_t, denoted as a, b, c, and A, have the following form

$$a = a_1 + a_2 u + a_3 v + a_4 w + \frac{1}{2} a_5 \mathbf{u}^2 + \frac{1}{2} a_6 \frac{2\epsilon_r}{m},$$

$$\ldots$$

$$A = A_1 + A_2 u + A_3 v + A_4 w + \frac{1}{2} A_5 \mathbf{u}^2 + \frac{1}{2} A_6 \frac{2\epsilon_r}{m}.$$

with $\mathbf{u} = (u, v, w)$.

Taking a as an example, it is calculated from the x-direction derivatives of g_t.

$$a = \frac{1}{g_t} \left(\frac{\partial g_t}{\partial x} \right),$$

with

$$\begin{aligned}
a_6 &= \frac{4\lambda_r^2}{K_r} \frac{1}{\rho} \left(2 \frac{\partial \rho E_r}{\partial x} - \frac{1}{2} \frac{K_r}{\lambda_r} \frac{\partial \rho}{\partial x} \right), \\
a_5 &= \frac{4\lambda_t^2}{3} \left(B - 2UR_1 - 2VR_2 - 2WR_3 \right), \\
a_4 &= 2\lambda_t R_3 - a_5 W, \\
a_3 &= 2\lambda_t R_2 - a_5 V, \\
a_2 &= 2\lambda_t R_1 - a_5 U, \\
\rho a_1 &= \frac{1}{\rho} \frac{\partial \rho}{\partial x} - a_2 U - a_3 V - a_4 W - \frac{1}{2} a_5 (\mathbf{U}^2 + \frac{3}{2\lambda_t}) - \frac{1}{2} a_6 \frac{K_r}{2\lambda_r},
\end{aligned}$$

with the defined variables

$$\begin{aligned}
B &= \frac{1}{\rho} \left(2 \frac{\partial (\rho E - \rho E_r)}{\partial x} - (\mathbf{U}^2 + \frac{3}{2\lambda_t}) \frac{\partial \rho}{\partial x} \right), \\
R_1 &= \frac{\partial U}{\partial x} = \frac{1}{\rho} \left(\frac{\partial \rho U}{\partial x} - U \frac{\partial \rho}{\partial x} \right), \\
R_2 &= \frac{\partial V}{\partial x} = \frac{1}{\rho} \left(\frac{\partial \rho V}{\partial x} - V \frac{\partial \rho}{\partial x} \right), \\
R_3 &= \frac{\partial W}{\partial x} = \frac{1}{\rho} \left(\frac{\partial \rho W}{\partial x} - W \frac{\partial \rho}{\partial x} \right),
\end{aligned}$$

where $\mathbf{U} = (U, V, W)$ and the derivatives of macroscopic quantities are evaluated at $(\mathbf{x}_{ij}, t^n)$.

Theoretically, the modified term g_q^+ in Eq. (3.16) only contributes to the heat conduction coefficient in the energy flux. By following the treatment in [114], the calculation of equilibrium flux can be simplified. We can ignore the modified terms and correct the heat flux by modifying only the spatial derivatives of temperature.

Based on the Chapman-Enskog expansion and the linearisation around translation temperature T_t [112], the heat fluxes $\mathbf{q}_t$ and $\mathbf{q}_r$ become

$$\begin{aligned}\mathbf{q}_t &= -\frac{5R}{2}\mu(T_t)\left(\Pr + \frac{(1-\omega_0)(1-\Pr)}{Z_r}\right)^{-1}\nabla_{\mathbf{x}}T_t,\\ \mathbf{q}_r &= -R\mu(T_t)\left(\delta + \frac{(1-\omega_1)(1-\delta)}{Z_r}\right)^{-1}\nabla_{\mathbf{x}}T_r,\end{aligned} \tag{3.19}$$

where $\mu(T_t) = \tau p_t$ and the pressure p_t is related to the translational temperature only through $p_t = \rho R T_t$.

We can modify the computed coefficients in the expansion of Maxwellian to get the above heat fluxes by re-scaling the translational and rotational temperature gradients, such as changing $a_5 = -2\partial_x\lambda_t$ and $a_6 = -2\partial_x\lambda_r$ to

$$\begin{aligned}\tilde{a}_6 &= a_6 \Big/ \left(\delta + \frac{(1-\omega_1)(1-\delta)}{Z_r}\right)\\ \tilde{a}_5 &= a_5 \Big/ \left(\Pr + \frac{(1-\omega_0)(1-\Pr)}{Z_r}\right).\end{aligned}$$

Thus, only few additional floating point operations are needed for each spatial slope reconstruction to correct the heat flux, and the final form of $\mathbf{F}_{ij}^{eq}$ becomes

$$\begin{aligned}\mathbf{F}_{ij}^{eq} = \int \Bigg[& q_1\left(g_t(t^n, \mathbf{x}_{ij}, \mathbf{u}, \epsilon_r) + \frac{g_r(t^n, \mathbf{x}_{ij}, \mathbf{u}, \epsilon_r) - g_t(t^n, \mathbf{x}_{ij}, \mathbf{u}, \epsilon_r)}{Z_r}\right)\\ & + g_t(t^n, \mathbf{x}_{ij}, \mathbf{u}, \epsilon_r)(q_2(\tilde{a}u + \tilde{b}v + \tilde{c}w) + q_3 A)\Bigg]\mathbf{u}\cdot\mathbf{n}_{ij}\boldsymbol{\psi}\,\mathrm{d}\Xi,\end{aligned} \tag{3.20}$$

with the above scaled coefficients $\tilde{a}_5, \tilde{a}_6$ and q_1, q_2, q_3 defined in Eq. (2.32).

In the UGKWP method, the distribution of the hydro-quantities $\mathbf{W}^h$ is known as g^*, the flux contributed by the free transport of collisional hydro-particles can

be partially evaluated analytically,

$$\sum_{j\in N(i)} \mathbf{F}_{ij}^{fr}|S_{ij}| = \sum_{j\in N(i)} \mathbf{F}_{ij}^{fr,h}|S_{ij}| - \mathbf{F}_{i}^{fr,p}.$$

As in Eq. (2.42) for monatomic gas, $\mathbf{F}_{ij}^{fr,h}$ is the free transport flux contributed by the hydro-quantities [88],

$$\begin{aligned}\mathbf{F}_{ij}^{fr,h} = \int \Bigg[\tilde{q}_4\Bigg(g_t^h(t^n,\mathbf{x}_{ij},\mathbf{u},\epsilon_r) + \frac{g_r^h(t^n,\mathbf{x}_{ij},\mathbf{u},\epsilon_r) - g_t^h(t^n,\mathbf{x}_{ij},\mathbf{u},\epsilon_r)}{Z_r}\Bigg) \\ + \tilde{q}_5 g_t^h(t^n,\mathbf{x}_{ij},\mathbf{u},\epsilon_r)(\tilde{a}u+\tilde{b}v+\tilde{c}w)\Bigg]\mathbf{u}\cdot\mathbf{n}_{ij}\boldsymbol{\psi}\,\mathrm{d}\Xi,\end{aligned} \tag{3.21}$$

where

$$\begin{aligned}\tilde{q}_4 &= q_4 - \Delta t e^{-\Delta t/\tau}, \\ \tilde{q}_5 &= q_5 + \frac{\Delta t^2}{2}e^{-\Delta t/\tau}.\end{aligned} \tag{3.22}$$

3.2.3 The Evolution of Particles

The simulation particle $P_k(m_k,\mathbf{x}_k,\mathbf{u}_k,e_{r,k},t_k^f,\omega_k,\kappa_k)$ is represented by its mass m_k, position coordinate $\mathbf{x}_k$, velocity coordinate $\mathbf{u}_k$, free streaming time t_k^f and rotational energy $e_{r,k}$. ω_k and κ_k are the weights coming from the Rykov kinetic model.

Note that the evolution of particles follows the integral form of the Rykov model in Eq. (3.10)

$$f(t,\mathbf{x},\mathbf{u},\epsilon_r) = (1-e^{-t/\tau})M^*(t,\mathbf{x},\mathbf{u},\epsilon_r) + e^{-t/\tau}f_0(\mathbf{x}-\mathbf{u}t,\mathbf{u},\epsilon_r). \tag{3.23}$$

A first order approximation of M^* can be expressed as

$$M^*(t,\mathbf{x},\mathbf{u},\epsilon_r) = g^*(t,\mathbf{x},\mathbf{u},\epsilon_r), \tag{3.24}$$

and the second order expansion gives

$$M^*(t,\mathbf{x},\mathbf{u},\epsilon_r) = g^*(t,\mathbf{x},\mathbf{u},\epsilon_r) + \frac{e^{-t/\tau}(t+\tau)-\tau}{1-e^{-t/\tau}}(\partial_t g^*(t,\mathbf{x},\mathbf{u},\epsilon_r) + \mathbf{u}\cdot\nabla_{\mathbf{x}} g^*(t,\mathbf{x},\mathbf{u},\epsilon_r)). \tag{3.25}$$

Here M^* is named as the hydrodynamic distribution function with analytical formulation. In this chapter, the approximation (3.24) for M^+ is used for a simple particle-sampling algorithm [40].

At the beginning of each step, we need to sample particles from g^* defined in Eq. (3.9). For cell Ω_i with hydro quantities $\mathbf{W}_i^h = (\rho_i^h, (\rho\mathbf{U})_i^h, (\rho E)_i^h, (\rho E_{rot})_i^h)$, using the stratification for variance reduction [102], hydro-particles can be sampled from the modified Maxwellian distribution $\tilde{g}_t$ with a total mass of $(1 - 1/Z_r)\rho_i^h|\Omega_i|$ and the modified Maxwellian distribution $\tilde{g}_r$ with a total mass of $\rho_i^h|\Omega_i|/Z_r$, respectively.

Taking $\tilde{g}_t$ as an example, its reduced distribution function in rotational variable ϵ_r can be written as

$$G_t = \int \tilde{g}_t \, \mathrm{d}\epsilon_r = G_m(\lambda_t)\left[1 + (1 - \mathrm{Pr})\frac{4\lambda_t^2 \mathbf{q}_t \cdot \mathbf{c}}{5\rho}\left(2\lambda_t \mathbf{c}^2 - 5\right)\right],$$

$$R_t = \int \frac{2\epsilon_r}{m}\tilde{g}_t \, \mathrm{d}\epsilon_r = \frac{K_r}{2\lambda_r}G_m(\lambda_t)\left[1 + (1 - \mathrm{Pr})\frac{4\lambda_t^2 \mathbf{q}_t \cdot \mathbf{c}}{5\rho}\left(2\lambda_t \mathbf{c}^2 - 5\right) + (1 - \delta)\frac{4\lambda_t \lambda_r \mathbf{q}_r \cdot \mathbf{c}}{\rho}\right],$$

with

$$G_m(\lambda) = \rho\left(\frac{\lambda}{\pi}\right)^{\frac{3}{2}} e^{-\lambda \mathbf{c}^2}.$$

Observed that the hydro quantities $\mathbf{W}_i^h$ can be calculated from the moments of the above reduced distributions

$$\begin{aligned}\mathbf{W}_i^h &= \int \begin{pmatrix} G_t \\ \mathbf{u}G_t \\ \frac{\mathbf{u}^2}{2}G_t + \frac{1}{2}R_t \\ \frac{1}{2}R_t \end{pmatrix}_i \mathrm{d}\mathbf{u} = \int \begin{pmatrix} \frac{G_t}{G_m}G_m \\ \mathbf{u}\frac{G_t}{G_m}G_m \\ \left(\frac{\mathbf{u}^2}{2}\frac{G_t}{G_m} + \frac{1}{2}\frac{R_t}{G_m}\right)G_m \\ \frac{1}{2}\frac{R_t}{G_m}G_m \end{pmatrix}_i \mathrm{d}\mathbf{u} \\ &\approx \sum \begin{pmatrix} \omega_k \frac{m_k}{|\Omega|_i} \\ \omega_k \frac{m_k \mathbf{u}_k}{|\Omega|_i} \\ \omega_k \frac{m_k \mathbf{u}_k^2}{2|\Omega|_i} + \kappa_k \frac{m_k e_{r,k}}{2|\Omega|_i} \\ \kappa_k \frac{m_k e_{r,k}}{2|\Omega|_i} \end{pmatrix}.\end{aligned} \tag{3.26}$$

To sample the velocity efficiently and recover the hydro quantities $\mathbf{W}_i^h$ exactly

on the macroscopic level. The idea of importance sampling [102] is followed. The sampled particles P_k, $k = 1, ..., N_i$ follow

$$\mathbf{u}_k \sim G_m(\lambda_{t,i}) \quad \mathbf{x}_k \sim \mathrm{U}(\Omega_i), \quad e_{r,k} = \frac{mK_r}{4\lambda_{r,i}} \tag{3.27}$$

where the rotational energy $\epsilon_{r,k}$ of particle P_k is simply set as equal partition instead of sampled from distribution $\frac{2\lambda_r}{m} e^{-\lambda_r \frac{2\epsilon_r}{m}}$.

The addition weights ω_k and κ_k are required to ensure the consistency between the moment of the sampled particles P_k and the macro quantities $\mathbf{W}_i^h$. As shown in Eq. (3.26), ω_k and κ_k are determined by the coefficients G_t/G_m and R_t/G_m, respectively, i.e.

$$\begin{aligned} \omega_k &= 1 + (1 - \mathrm{Pr}) \frac{4\lambda_{t,i}^2 \mathbf{q}_{t,i} \cdot \mathbf{c}_k}{5\rho_i} \left(2\lambda_{t,i}\mathbf{c}_k^2 - 5\right), \\ \kappa_k &= 1 + (1 - \mathrm{Pr}) \frac{4\lambda_{t,i}^2 \mathbf{q}_{t,i} \cdot \mathbf{c}_k}{5\rho_i} \left(2\lambda_{t,i}\mathbf{c}_k^2 - 5\right) + (1 - \delta) \frac{4\lambda_{t,i}\lambda_{r,i} \mathbf{q}_{r,i} \cdot \mathbf{c}_k}{\rho_i}. \end{aligned} \tag{3.28}$$

Similar to monatomic gas, the symmetric sampling is adopted here to reduce the variance. Since the numerical flux contributed by the streaming of collisional particles can be evaluated by $\mathbf{F}_{ij}^{fr,h}$ analytically, only the collisionless hydro-particle will be sampled.

Based on the cumulative distribution function of the first collision time Eq. (2.35), the collisionless hydro-particles are sampled with the total mass of

$$m_k = \left(1 - \frac{1}{Z_r}\right) \frac{e^{-\Delta t/\tau_i} \rho_i^h |\Omega|_i}{N_i}. \tag{3.29}$$

Now all the quantities of P_k are determined.

The net free streaming flux contributed by the streaming of all left collisionless and collisional particles can be calculated by counting the particles passing through the cell interface, which can be written as,

$$\mathbf{F}_i^{fr,p} = \sum_{k \in P_{\partial\Omega_i^+}} \mathbf{W}_{P_k} - \sum_{k \in P_{\partial\Omega_i^-}} \mathbf{W}_{P_k}, \tag{3.30}$$

where $\mathbf{W}_{P_k} = (\omega_k m_k, \omega_k m_k \mathbf{u}_k, m_k(\frac{1}{2}\omega_k \mathbf{u}_k^2 + \kappa_k e_k), \kappa_k e_k)$, $P_{\partial\Omega_i^+}$ is the index set of the particles streaming into cell Ω_i during a time step, and $P_{\partial\Omega_i^-}$ is the index set of the particles streaming out of cell Ω_i.

3.2.4 The Update of Macroscopic Variables with Source Term

Therefore, the evolution of macroscopic flow variables in Eq. (2.44) now becomes

$$\mathbf{W}_i^* = \mathbf{W}_i^n + \frac{1}{|\Omega_i|}\bigg(- \sum_{j\in N(i)} \mathbf{F}_{ij}^{eq}|S_{ij}| - \sum_{j\in N(i)} \mathbf{F}_{ij}^{fr,h}|S_{ij}| + \mathbf{F}_i^{fr,p}\bigg). \tag{3.31}$$

from which $\rho^{n+1}, (\rho\mathbf{U})^{n+1}$ and $(\rho E)^{n+1}$ can be updated. Then, from Eq. (3.14), the equilibrium rotational energy $(\rho E_r^{eq})^{n+1}$ can be updated as well.

Due to existence of the source term in the update of rotational energy, a semi-implicit scheme is used to update ρE_r, and the source term for rotational energy can be approximated as

$$S = \frac{\Delta t}{2}\left(\frac{2(\rho E_r^{eq})^{n+1} - (\rho E_r)^* - (\rho E_r)^{n+1}}{Z_r^*\tau^*}\right), \tag{3.32}$$

and finally $(\rho E_r)^{n+1}$ can be updated

$$(\rho E_r)^{n+1} = \left(1 + \frac{\Delta t}{2Z_r^*\tau^*}\right)^{-1}\left((\rho E_r)^* + \frac{\Delta t}{2}\left(\frac{2(\rho E_r^{eq})^{n+1} - (\rho E_r)^*}{Z_r^*\tau^*}\right)\right). \tag{3.33}$$

The algorithm of UGKWP method for diatomic gases can be summarized as following:

1. Sample free streaming time t_k^f by Eq. (2.36) for particles P_k from W^p. These particles are classified into collisionless particles and collisional particles. Then, stream all the particles by Eq. (2.37). For the first step, $W^p = 0$.

2. Sample the particle quantities $(m_k, \mathbf{x}_k, \mathbf{u}_k, e_{r,k}, \omega_k, \kappa_k)$ by Eqs. (3.27) to (3.29) for each newly added collisionless hydro-particle P_k from the hydro-quantities

$\mathbf{W}^h$. These particles are all defined as collisionless particles which have $t^f = \Delta t$. For the first step, $W^h = W^{n=0}$.

3. Calculate the particle free streaming flux $\mathbf{F}^{fr,p}$ by Eq. (3.30), and evaluate the equilibrium flux $\mathbf{F}_{ij}^{eq}$ and hydrodynamic wave free transport flux $\mathbf{F}_{ij}^{fr,h}$ by Eqs. (3.20) and (3.21), respectively.

4. Update macroscopic flow variables $\mathbf{W}$ by Eqs. (3.31) and (3.33). Calculate the macro-quantities of collisionless particles $\mathbf{W}^p$ by collecting the macro-quantities of collisionless particles, from which the density of hydro-quantities $\mathbf{W}^h$ is obtained by $\rho^h = \rho - \rho^p$.

5. Keep collisionless particles and remove collisional particles. Then, go to step 1.

3.3 Analysis and Discussion

3.3.1 Collisionless Limit

Consider the collisionless limit when $\tau \to \infty$, the coefficients in Eqs. (2.32) and (3.22) become

$$\begin{aligned} \lim_{\tau\to\infty} q_i &= 0, \quad i \in \{1,2,3\} \\ \lim_{\tau\to\infty} \tilde{q}_i &= 0, \quad i \in \{4,5\} \end{aligned} \tag{3.34}$$

Therefore, the equilibrium flux $\mathbf{F}^{eq}$ and the analytical flux $\mathbf{F}^{fr,h}$ will be 0. The only contribution to the flux is the particle free streaming flux $\mathbf{F}^{fr,p}$.

The free streaming time for the particles becomes

$$\lim_{\tau\to\infty} t^f = \Delta t \tag{3.35}$$

which means that all particles will be streamed without collision. And hence the UGKWP method degenerates to a collisionless Boltzmann solver.

3.3.2 Asymptotic Behavior in Continuum Regime

In this section, we are going to analyze the asymptotic behavior of the UGKWP method with diatomic relaxation in continuum regime. For simplicity, the following analysis is based on two-dimensional case. Following the Chapman-Enskog procedure, one can show that the macro description of the Rykov model [112] can be written as,

$$
\begin{aligned}
&\frac{\partial \rho}{\partial t}+\frac{\partial(\rho U)}{\partial x}+\frac{\partial(\rho V)}{\partial y}=0,\\
&\frac{\partial(\rho U)}{\partial t}+\frac{\partial(\rho U^2+p_t)}{\partial x}+\frac{\partial(\rho UV)}{\partial y}=\frac{\partial \tau_{xx}}{\partial x}+\frac{\partial \tau_{yx}}{\partial y},\\
&\frac{\partial(\rho V)}{\partial t}+\frac{\partial \rho UV}{\partial x}+\frac{\partial(\rho V^2+p_t)}{\partial y}=\frac{\partial \tau_{xy}}{\partial x}+\frac{\partial \tau_{yy}}{\partial y},\\
&\frac{\partial(\rho E)}{\partial t}+\frac{\partial(\rho EU+p_tU)}{\partial x}+\frac{\partial(\rho EV+p_tV)}{\partial y}=\frac{\partial(U\tau_{xx}+V\tau_{xy}+q_x)}{\partial x}+\frac{\partial(U\tau_{yx}+V\tau_{yy}+q_y)}{\partial y},\\
&\frac{\partial(\rho E_r)}{\partial t}+\frac{\partial(\rho E_rU)}{\partial x}+\frac{\partial(\rho E_rV)}{\partial y}=\frac{\partial q_{rx}}{\partial x}+\frac{\partial q_{ry}}{\partial y}+\frac{\rho E_r^{eq}-\rho E_r}{Z_r\tau}.
\end{aligned}
\tag{3.36}
$$

Here the viscous and heat conduction terms are

$$
\begin{aligned}
&\tau_{xx}=\tau p_t\left[2\frac{\partial U}{\partial x}-\frac{2}{3}\left(\frac{\partial U}{\partial x}+\frac{\partial V}{\partial y}\right)\right],\\
&\tau_{yy}=\tau p_t\left[2\frac{\partial V}{\partial y}-\frac{2}{3}\left(\frac{\partial U}{\partial x}+\frac{\partial V}{\partial y}\right)\right],\\
&\tau_{xy}=\tau_{yx}=\tau p_t\left(\frac{\partial U}{\partial y}+\frac{\partial V}{\partial x}\right)\\
&(q_x,q_y)^T=\mathbf{q}_r+\mathbf{q}_t,\\
&(q_{rx},q_{ry})^T=\mathbf{q}_r,
\end{aligned}
\tag{3.37}
$$

where $\mathbf{q}_r$ and $\mathbf{q}_t$ are defined in Eq. (3.19). The pressure $p_t=\rho RT_t$ is only related to the translational temperature.

Proposition 3.3.1 (Asymptotic preserving property)**.** *Consider a well resolved flow region with $g_t^l=g_t^r$ and $\nabla_{\mathbf{x}}g_t^l=\nabla_{\mathbf{x}}g_t^r$ at cell interface, for fixed time Δt, and small τ, the scheme is asymptotically equivalent, up to $\mathcal{O}(\tau^2)$, to a first order scheme for the system* (3.36) *and* (3.37)*.*

Proof. For cell i, the total mass of the sampled collisionless hydro-particles is $m^h = e^{-\Delta t/\tau_i}|\Omega_i|\rho_i^h$, and the total mass of the collisionless and collisional particles m^p is proportional to m^h, i.e. $m^p \sim \mathcal{O}(e^{-\Delta t/\tau_i})$.

Therefore, the numerical flux contribution by collisionless and collisional particle streaming is $\mathbf{F}_i^{fr,p} \sim \mathcal{O}(e^{-\Delta t/\tau_i})$.

In the free transport flux of hydro-quantities $\mathbf{F}_{ij}^{fr,h}$ given by Eq. (3.21), the hydrodynamic distribution function $M^*(t,\mathbf{x},\mathbf{u},\epsilon_r)$ in Eq. (3.25) becomes

$$M^*(t,\mathbf{x},\mathbf{u},\epsilon_r) = g^* - \tau\left(\partial_t g_t + u\partial_x g_t + v\partial_y g_t\right) + \mathcal{O}(\tau^2). \tag{3.38}$$

Substituting Eq. (3.38) into Eq. (3.21), and assuming $\mathbf{n}$ point to x-direction, the total analytical flux $\mathbf{F}^{an}$ of the macroscopic variables becomes

$$\begin{aligned}
\mathbf{F}^{an} =& \mathbf{F}^{eq} + \mathbf{F}^{fr,h} \\
=& \int u\Big\{(q_1+\tilde{q}_4)g^* + (q_2-\tau\tilde{q}_4+\tilde{q}_5)(u\partial_x g_t + v\partial_y g_t) + (q_3-\tau\tilde{q}_4)\partial_t g_t\Big\}\boldsymbol{\psi}\,\mathrm{d}\Xi + \mathcal{O}(\tau^2) \\
=& \int u\Big\{g^* - \tau(u\partial_x g_t + v\partial_y g_t + \partial_t g_t) + \frac{1}{2}\Delta t\partial_t g_t\Big\}\boldsymbol{\psi}\,\mathrm{d}\Xi + \mathcal{O}(\tau^2).
\end{aligned} \tag{3.39}$$

If $\mathcal{O}(\tau^2)$ terms are neglected, Eq. (3.39) becomes

$$\begin{aligned}
\mathbf{F}^{an} =& \int u\Big\{g^* - \tau(u\partial_x g_t + v\partial_y g_t + \partial_t g_t) + \frac{1}{2}\Delta t\partial_t g_t\Big\}\boldsymbol{\psi}\,\mathrm{d}\Xi \\
=& \begin{pmatrix} \rho U \\ \rho U^2 + p_t - \tau_{xx} \\ \rho UV - \tau_{xy} \\ \rho E + p_t U - U\tau_{xx} - V\tau_{xy} - q_x \\ \rho E_r + \rho E_r U - q_{rx} \end{pmatrix} + \frac{1}{2}\Delta t \begin{pmatrix} \frac{\partial \rho U}{\partial t} \\ \frac{\partial \rho U^2}{\partial t} + \frac{\partial p_t}{\partial t} \\ \frac{\partial \rho UV}{\partial t} \\ \frac{\partial \rho E}{\partial t} + \frac{\partial p_t U}{\partial t} \\ \frac{\partial \rho E_r}{\partial t} + \frac{\partial \rho E_r U}{\partial t} \end{pmatrix}
\end{aligned} \tag{3.40}$$

It can be observed that the numerical flux is consistent with the flux in system (3.36) and (3.37). Therefore, in the continuum regime, the UGKWP method converges to Eq. (3.36), which is a first order scheme for the system (3.36) and (3.37). □

For the limiting Euler system with the absence of viscous and heat conduction terms, we can have the following proposition.

Proposition 3.3.2. *Consider a well resolved flow region with $g_t^l = g_t^r$ and $\nabla_{\mathbf{x}} g_t^l = \nabla_{\mathbf{x}} g_t^r$ at cell interface, for fixed time Δt, in the limit $\tau \to 0$, the scheme becomes a second order method for the limiting Euler system with the absence of viscous and heat conduction terms in system* (3.36) *and* (3.37).

Proof. As $\tau \to 0$, following directly from Eq. (3.40), we have

$$\mathbf{F}^{an} = \begin{pmatrix} \rho U \\ \rho U^2 + p_t \\ \rho UV \\ \rho E + p_t U \\ \rho E_r + \rho E_r U \end{pmatrix} + \frac{1}{2}\Delta t \begin{pmatrix} \frac{\partial \rho U}{\partial t} \\ \frac{\partial \rho U^2}{\partial t} + \frac{\partial p_t}{\partial t} \\ \frac{\partial \rho UV}{\partial t} \\ \frac{\partial \rho E}{\partial t} + \frac{\partial p_t U}{\partial t} \\ \frac{\partial \rho E_r}{\partial t} + \frac{\partial \rho E_r U}{\partial t} \end{pmatrix}.$$

Combining with the semi-implicit update of source term, it can be observed that this is exactly a second order scheme for the limiting Euler system. □

In the limit of total equilibrium state with $Z_r = 1$, both the translational temperature and the rotational temperature converge to the equilibrium temperature as $\tau \to 0$. From Eq. (3.17), the pressure p_t can be rewritten as,

$$p_t = p + p_t - p = p - \frac{4}{15} Z_r \tau p \left(\frac{\partial U}{\partial x} + \frac{\partial V}{\partial y} \right). \tag{3.41}$$

When $Z_r = 1$, the second term on the right hand side of Eq. (3.41) is exactly the bulk viscosity for rotational degrees of freedom in NS equations.

In the continuum regime with $\Delta t \gg \tau$, for a fixed particle mass m_k, the number of sampled collisionless hydro-particles in cell i is $e^{-\Delta t/\tau_i} |\Omega_i| \rho_i^h / m_k$, where the total simulation particle number N_p in such regime decreases exponentially, $N_p \sim \mathcal{O}(e^{-\Delta t/\tau})$. Therefore, the computational cost of UGKWP in continuum regime becomes comparable to hydrodynamic NS solvers, such as recovering GKS for the NS solution [63].

3.4 Numerical Results

3.4.1 Normal Shock

To demonstrate the accuracy of UGKWP method in capturing the highly non-equilibrium flow, one dimensional shock wave is studied. For the nitrogen gas, the viscous coefficient is given as

$$\mu = \mu_{ref} \left(\frac{T}{T_0} \right)^{\omega}, \tag{3.42}$$

with the temperature dependency index $\omega = 0.72$, and the reference viscosity

$$\mu_{ref} = \frac{15\sqrt{\pi}}{2(5-2\omega)(7-2\omega)} \text{Kn}. \tag{3.43}$$

In this calculation, the reference length is the upstream mean free path, and the computational domain is [-25,25] with 100 cells. The upstream ($x \leq 0$) and downstream ($x > 0$) flow variables are connected by the Rankine-Hugoniot condition. The collision rotation number used in the UGKWP is $Z_r = 2.4$. In order to reduce the statistical noise, 5×10^3 simulation particles are used in each cell. The normalized temperature and density from UGKWP and DSMC [78] at Ma $= 1.53, 4.0, 5.0, 7.0$ are plotted in Fig. 3.1. As analyzed before, since the Rykov model reduces to Shakhov model at large Z_r, the early rising of the temperature occurs at high Mach number.

The reason for the early rising of temperature is due to the use of the single relaxation time in these kinetic models, which is inconsistent with the physical reality that the high speed particles should have shorter relaxation time. In Chapter 4, by a simple control on the relaxation time of the high speed particles, one can get significant improvement on the problem of early temperature rising.

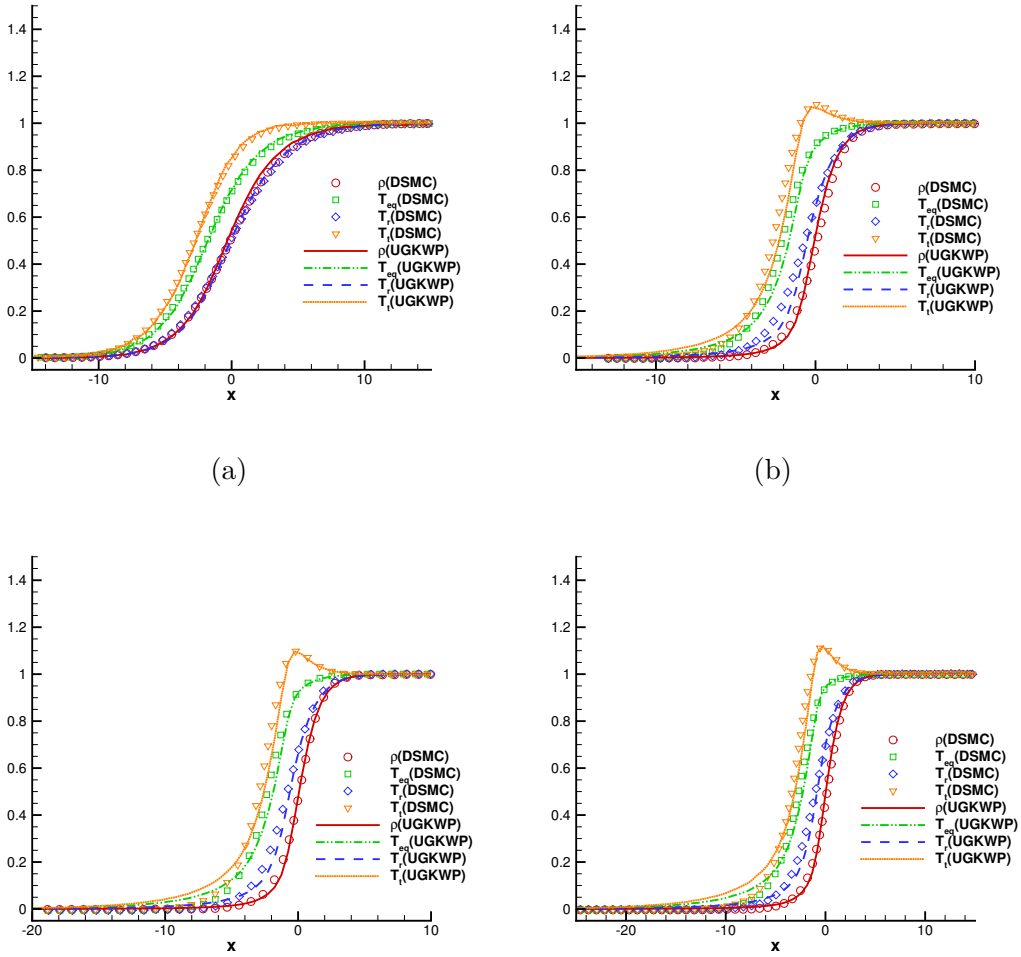

Figure 3.1: Comparison of UGKWP and DSMC results of nitrogen shock wave at different Mach numbers for nitrogen gas. (a)Ma = 1.53; (b)Ma = 4.0; (c)Ma = 5.0; (d)Ma = 7.0. The x-coordinate is normalized by ℓ. The symbols are DSMC results from Ref. [78].

3.4.2 Flow Passing a Flat Plate

Following the experiment conducted by Tsuboi and Matsumoto [115], the hypersonic rarefied gas flow over a flat plate is simulated using UGKWP for nitrogen gas. The case is run 34, where the nozzle exit Mach number is Ma = 4.89, the nozzle exit pressure is P_e = 2.12Pa, the stagnation pressure is P_0 = 983Pa

and the nozzle exit temperature is $T_e = 116$K. The stagnation temperature is $T_0 = 670$K, which is used as a reference temperature to determine the viscosity coefficient,

$$\mu = \mu_{ref} \left(\frac{T_t}{T_0} \right)^{\omega}.$$

The reference viscosity is defined as

$$\mu_{ref} = \frac{5\sqrt{2\pi R T_{ref}}}{16} \rho_{ref} l_{mfp},$$

where $\rho_{ref} = 6.15 \times 10^{-5}$kg m $^{-3}$ is the reference density, $l_{mfp} = 0.78$mm is the mean free path and $T_{ref} = 116$K is the reference temperature. The flat plate has a constant wall temperature of 290K and the diffusive boundary condition is adopted at the plate. In this case, the relaxation collision number Z_r is set to be 3.5.

In this study, 59×39 grid points are used above the plate and 44×25 grid points are used below the plate, with the same configuration as that used in UGKS [78]. The contours of density, equilibrium temperature, rotational temperature and translational temperature are shown in Fig. 3.2. The temperature distribution along the vertical line above the flat plate at $x = 5$mm and $x = 20$mm are shown in Fig. 3.3, which show good agreement with the experiment measurements.

3.4.3 Flow Passing a Sphere

The three dimensional case is about Ma = 4.25 nitrogen gas flow passing through a sphere at Kn = 0.031 and Kn = 0.121 in the transition regime. The radius of sphere is 10^{-3}m and the surface mesh of the sphere is divided into 6 blocks with 16×16 mesh points in each block with a minimum surface spacing 6.255×10^{-5}m. Diffusive wall boundary condition with a constant temperature $T_w =$

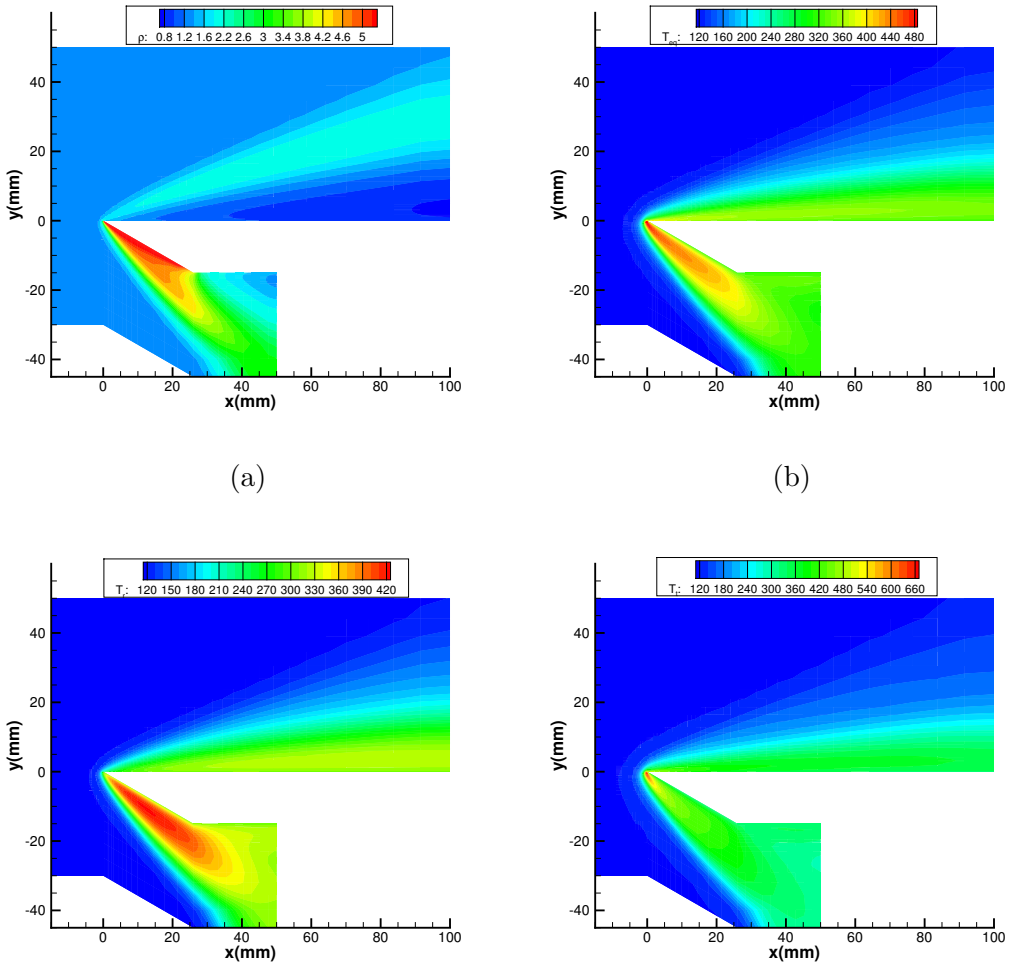

Figure 3.2: (a)Density and (b)temperature (c)rotational temperature (d) translational temperature contour for the hypersonic flow passing a flat plate

302K is imposed on the surface. The computational domain is composed of 29700 hexahedra with growth rate 1.1 and smallest cell height 5×10^{-5} m. The inflow is diatomic nitrogen gas with molecular mass $m = 4.65 \times 10^{-26}$kg and diameter $d = 4.17 \times 10^{-10}$m. The upstream flow temperature is set to be $T_\infty = 65$K. The reference viscosity is given by the variable hard sphere (VHS) model with $\omega = 0.74$.

For the case of Kn = 0.031, the time-averaging starts from 2500 steps and con-

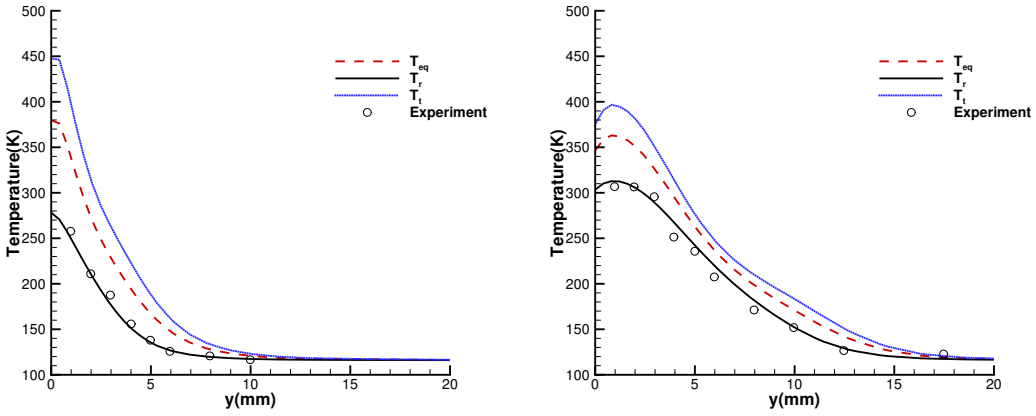

Figure 3.3: Temperature profiles along vertical lines at (a) x = 5mm and (b) x = 20 mm. The experiment results [115] are shown in symbol, and the UGKWP solutions are shown in line.

tinues for 13000 steps with an initial field computed by 1000 steps GKS. The total computation takes 13500 time steps, and runs on a workstation with (Dual CPU) Intel Xeon Platinum 8168 at 2.70 GHz with 48 cores. The distribution of density, velocity, temperature, and rotational temperature are shown in Fig. 3.4.

For the case of Kn = 0.121, the time-averaging starts from 2500 steps and continues for 17000 steps with an initial field computed by 1000 steps GKS. The distribution of density, velocity, temperature, and rotational temperature are shown in Fig. 3.5. Figure 3.6 shows the relative error in drag coefficient (Air) given by UGKWP and experiments [116].

Both UGKS and UGKWP can obtain satisfactory drag coefficients compared with the experimental data. However, the computational efficiency is greatly improved by the UGKWP method.The detail comparison of the computational cost between UGKWP method and the implicit UGKS [6] is shown in Table 3.1.

Apart from the above two cases, a hypersonic case with Ma = 10 and Kn = 0.01

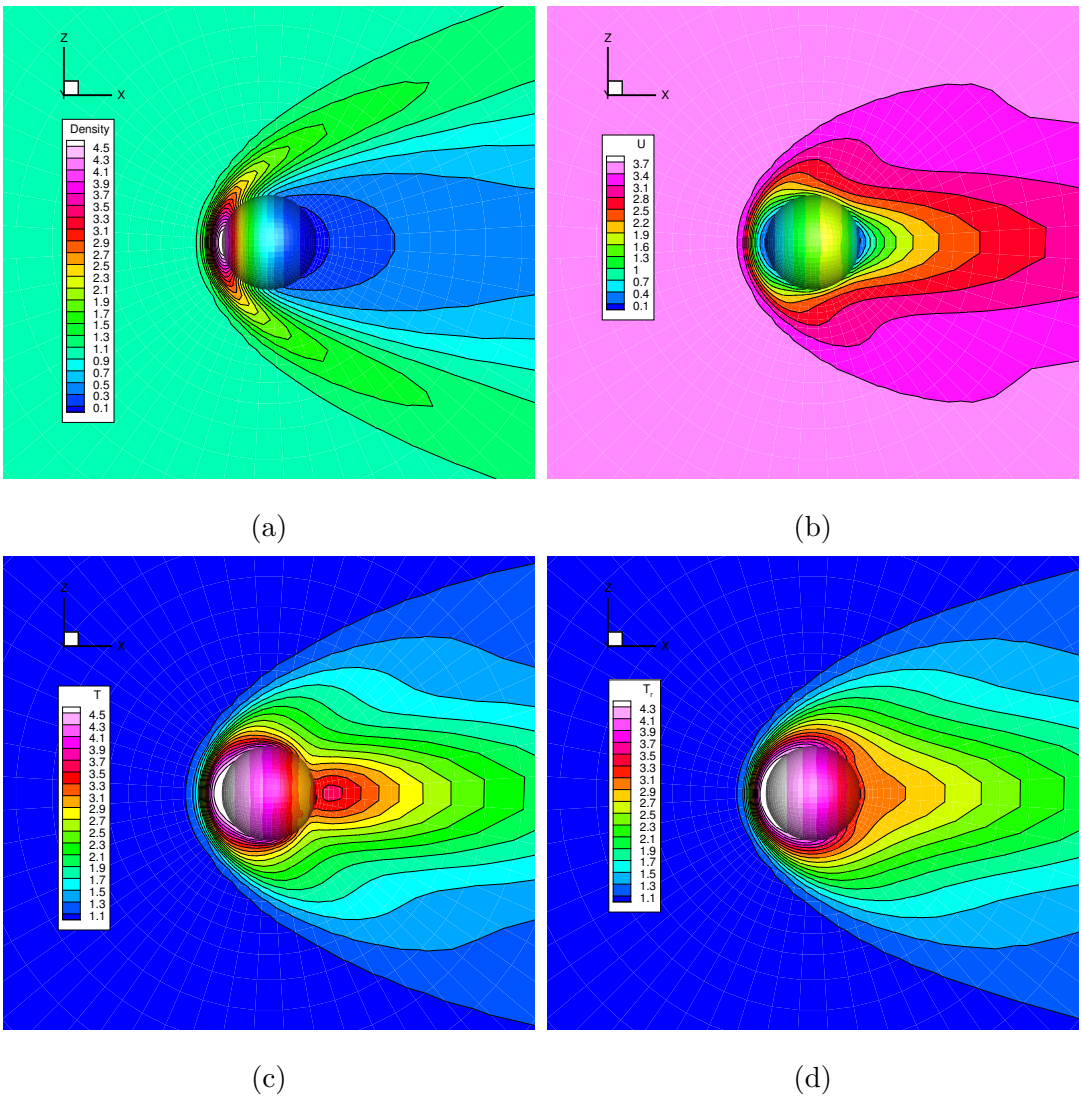

(a) (b)

(c) (d)

Figure 3.4: (a)Density and (b)x direction velocity (c)temperature (d) rotational temperature contour for Kn = 0.031 and Ma = 4.25.

Ma_∞	Kn_∞	Time of Implicit UGKS	Time of UGKWP(Nitrogen)	Time ratio $\frac{\text{UGKS}}{\text{UGKWP}}$
4.25	0.121	265.6 hours	32 hours	8.3
4.25	0.031	265.6 hours	3.1 hours	85.7

Table 3.1: Comparison of the computational cost between UGKWP method and the implicit UGKS in 48 cores.

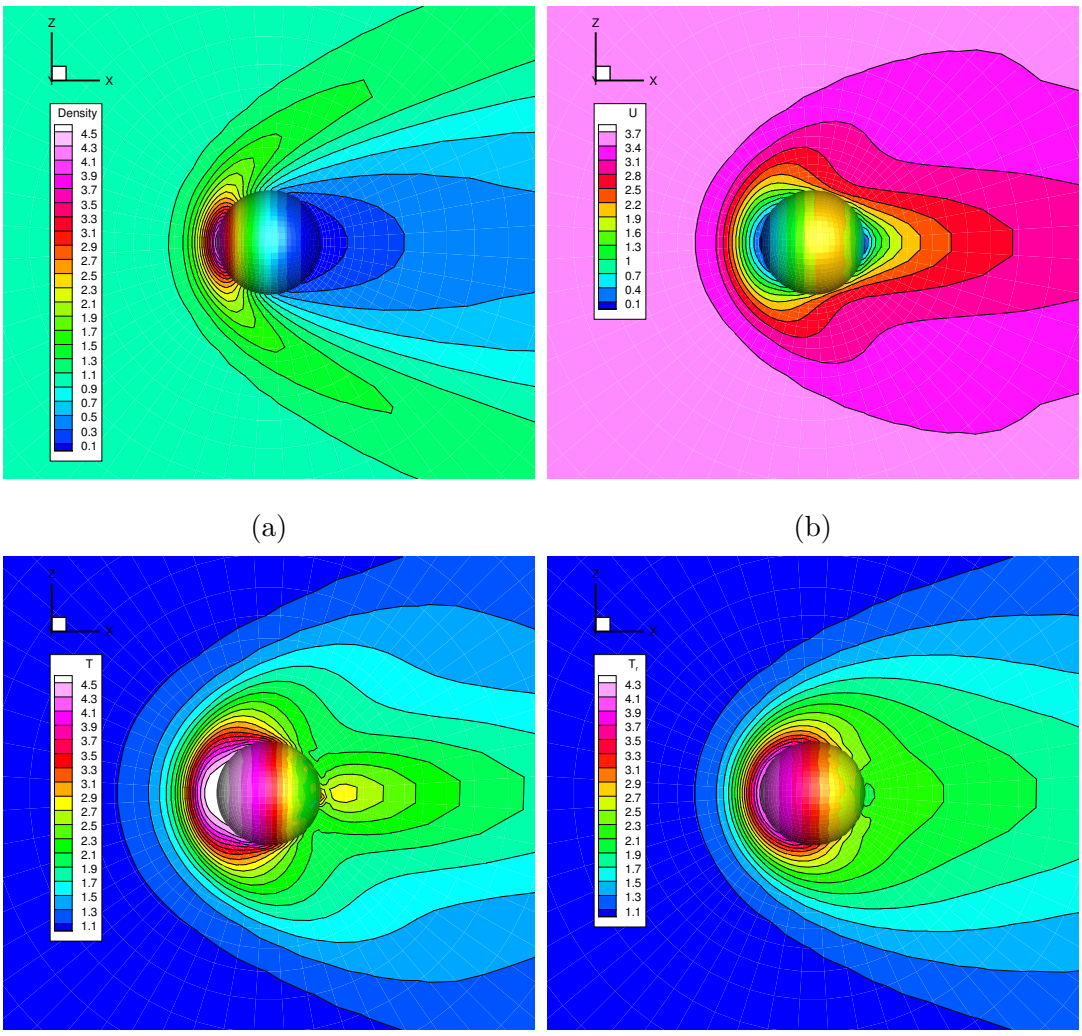

Figure 3.5: (a)Density and (b)x direction velocity (c)temperature (d) rotational temperature contour for Kn = 0.121 and Ma = 4.25.

is also calculated. In order to calculate this hypersonic case, the computational cost for the UGKS will become unaffordable since it needs a huge discrete velocity space to get an accurate solution. For the UGKWP method, the computation for Mach 10 case needs only 1.46 hour with a personal 48 cores workstation. The distribution of density, velocity, temperature, and rotational temperature are shown in Fig. 3.7. The drag coefficient is also shown in Table 3.2.

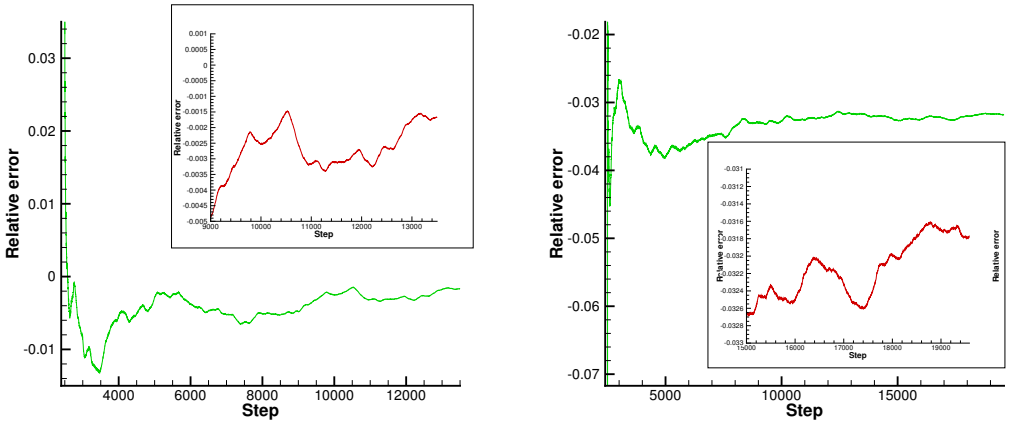

(a) (b)

Figure 3.6: Relative error of the drag coefficient at Kn = 0.031 (left) and Kn = 0.121 (right).

Ma_∞	Kn_∞	Experiment(Air)	UGKWP(Nitrogen)		UGKS(Nitrogen)	
			Drag coefficient	Relative error	Drag coefficient	Relative error
4.25	0.121	1.69	1.636 ± 0.0005	$-3.21\% \pm 0.03\%$	1.694	-0.27%
4.25	0.031	1.35	1.346 ± 0.0007	$-0.25\% \pm 0.05\%$	1.355	-0.39%
10	0.01	-	1.215 ± 0.0001	-	-	-

Table 3.2: Comparison of the drag coefficients

3.5 Conclusion

In this chapter, the unified gas-kinetic wave-particle method has been developed for diatomic gas, where the Rykov model is used for the molecular collision term with the exchange of translational and rotational energy. The UGKWP for diatomic gas has been validated in many test cases. Reasonable agreements have been obtained among UGKWP solutions, DSMC results, and experimental measurements.

Moreover, following the same strategy in current chapter, one can easily extend

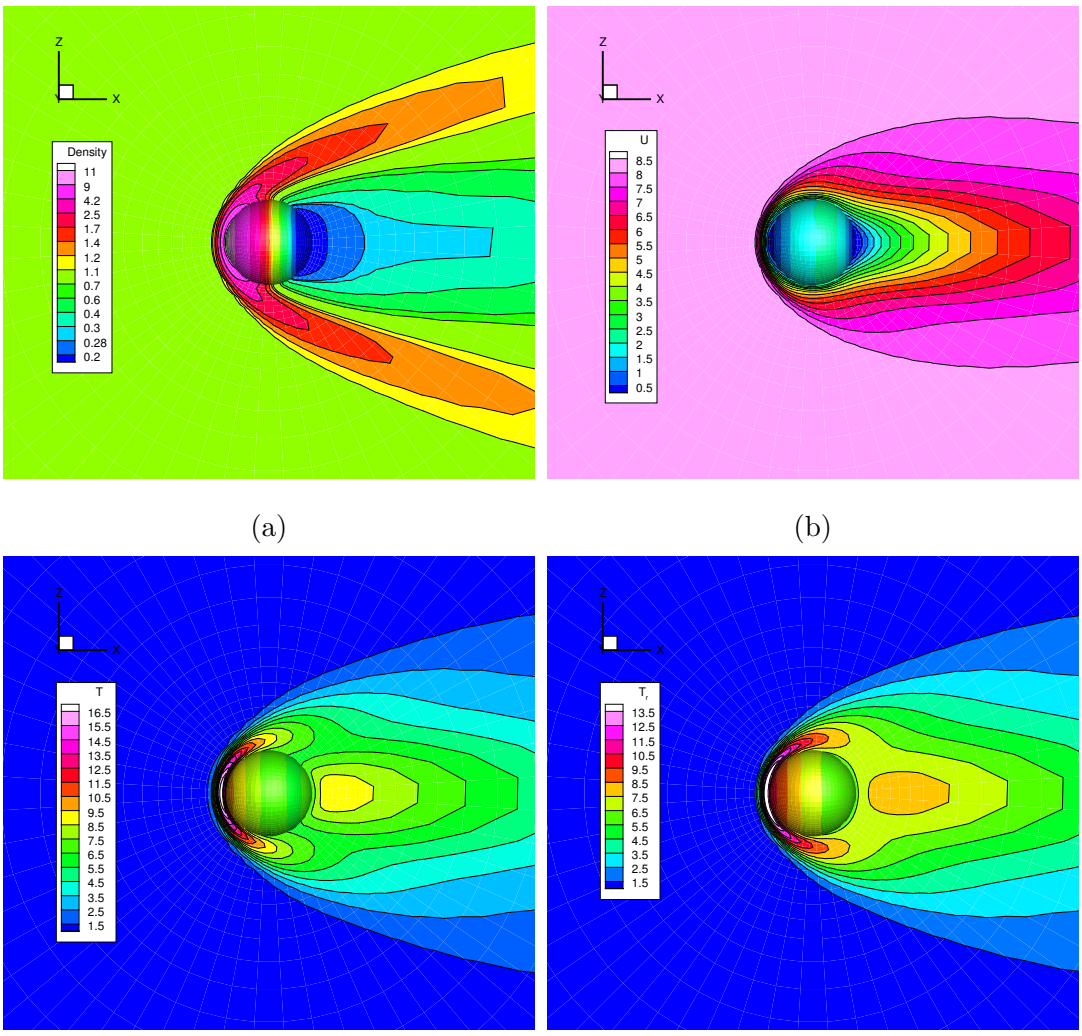

(a) (b)

(c) (d)

Figure 3.7: (a)Density and (b)x direction velocity (c)temperature (d) rotational temperature contour for Kn = 0.01 and Ma = 10.

the current scheme to vibration by adding

$$\frac{2}{m}\frac{\lambda_v^{K_v/2}}{\Gamma(K_v/2)}\left(\frac{2\epsilon_v}{m}\right)^{K_v/2-1} e^{-\lambda_v \frac{2\epsilon_v}{m}} \tag{3.44}$$

to the end of Eqs. (3.6) and (3.7).

Chapter 4

Further Development of Unified Gas-kinetic Wave-particle Method

This chapter is arranged as follows. Section 4.1 stress the motivation and the possibility for the further development of the UGKWP method. Section 4.2 reviews the kinetic model equation-based multiscale UGKWP method and presents the calculation of particle collision time according to particle velocity. Section 4.3 tests the UGKWP in shock structure calculations for diatomic gases and flow passing through a cylinder at high Mach numbers. The last section is the conclusion.

4.1 Motivation

The evolution of particle and wave in UGKWP is controlled by the integral solution of the kinetic relaxation model. Even though, accurate solutions can be obtained from UGKWP in all flow regimes, especially in the near continuum

and continuum regimes, there are still some discrepancies in the solution in the highly non-equilibrium flow regime, such as the temperature distribution inside shock layer at high Mach number. The reason for the difference is mainly coming from the single relaxation time approximation for all speed particles in the kinetic model equation, while the physical relaxation time varies according particle velocity, as expressed in the Boltzmann collision term and the DSMC.

In fact, according to basic kinetic theory, the particle collision time τ is directly related to the particle mean free path ℓ and particle velocity $|\mathbf{u}|$, such as $\tau = \ell/|\mathbf{u}|$. Due to the wave-particle decomposition in UGKWP, in the highly rarefied regime, the flow evolution in UGKWP is mainly controlled by particles. Therefore, the collision time of particle transport in UGKWP can be simply modified according to particle velocity. Since this only affects the free transport distance of individual particle, the mass, momentum, and energy of the system are fully conserved. This direct modeling on the particle transport greatly improves the performance of UGKWP for the rarefied flow solution, where excellent results can be obtained and matched with the Boltzmann or DSMC solutions.

The direct modeling on the determination of particle collision time improves the physical foundation of UGKWP and goes beyond the single relaxation kinetic model equation. Multiple relaxation time according to particle velocity can be directly modeled and implemented in the scheme. In the near continuum regime, the particles in UGKWP will disappear and a Navier-Stokes flow solver with all correct transport coefficients is recovered in the continuum flow regime.

4.2 Methodology

Note that the Boltzmann Equation (2.1) can be formulated as

$$\frac{\partial f}{\partial t} + \mathbf{u} \cdot \nabla_{\mathbf{x}} f = Q(f, f) = \nu(f^{+} - f). \tag{4.1}$$

Here ν is the collision frequency, Q^+ is the inverse collision integral,

$$Q^+ = \int_{\mathcal{S}^2} \mathcal{B}(|\mathbf{g}|, \mathbf{\Omega}) f(\mathbf{u}') f(\mathbf{u}'_*) \, \mathrm{d}\mathbf{\Omega} \, \mathrm{d}\mathbf{u}_*, \tag{4.2}$$

$$\nu = \int_{\mathcal{S}^2} \mathcal{B}(|\mathbf{g}|, \mathbf{\Omega}) f(\mathbf{u}) \, \mathrm{d}\mathbf{\Omega} \, \mathrm{d}\mathbf{u}_*, \quad f^+ = \frac{Q^+}{\nu}. \tag{4.3}$$

In above equation, the collision frequency $\nu(\mathbf{u})$ depends on the particle velocity, except that the Maxwellian molecule's differential cross-section σ is inversely proportional to the relative velocity $\mathbf{g}$ of the colliding pair.

In the kinetic relaxation model for the evolution of gas distribution function f

$$\frac{\partial f}{\partial t} + \mathbf{u} \cdot \nabla_{\mathbf{x}} f = \frac{M - f}{\tau}, \tag{4.4}$$

where the equilibrium state M is given differently in the BGK [31], ES [32], Shakhov models [33] for monatomic gases, and Rykov model [112] for diatomic gases.

Recall that to obtain the integral solution of relaxation Eq. (4.4),

$$f(t, \mathbf{x}, \mathbf{u}, \boldsymbol{\xi}) = \frac{1}{\tau} \int_0^t e^{-(t-t')/\tau} M(t', \mathbf{x}', \mathbf{u}, \boldsymbol{\xi}) \, \mathrm{d}t' + e^{-t/\tau} f_0(\mathbf{x} - \mathbf{u}t), \tag{4.5}$$

the local relaxation time τ is assumed to be a local constant and is independent of particle velocity $\mathbf{u}$. Moreover, comparing relaxation Eq. (4.4) with Boltzmann Equation (4.1), in highly rarefied regime, the equilibrium state M in the relaxation model would deviate from the Boltzmann counterpart f^+.

In traditional DVM-type methods, it is very hard to define a particle velocity-dependent relaxation time $\tau(\mathbf{u})$ with the complete satisfaction of conservation from the collision term. In stochastic particle methods, the real individuality of particle movement makes it easy determine particle collision according to its velocity. In the wave-particle formulation, the use of particle for the capturing of non-equilibrium transport also helps to include realistic physical process.

The UGKWP updates both the macroscopic flow variables and the gas distribution function in the presence of particles. Specifically, the macroscopic variables will be updated in a conservative form

$$\mathbf{W}_i^{n+1} = \mathbf{W}_i^n - \frac{1}{|\Omega_i|}\sum_{j\in N(i)} \mathbf{F}_{ij}^{eq}|S_{ij}| - \frac{1}{|\Omega_i|}\sum_{j\in N(i)} \mathbf{F}_{ij}^{fr,h}|S_{ij}| + \frac{\mathbf{F}_i^{fr,p}}{|\Omega_i|}. \tag{4.6}$$

One of the outstanding features of UGKWP is that the initial gas distribution function f_0 is composed of collisional particle and collisionless particle in the evolution process within a time step Δt. The flux in $\mathbf{F}^{fr,h}$ from the collisional particle can be evaluated analytically. The collisionless particle number reduces as $\exp(-\Delta t/\tau)$. In the continuum flow regime, all particles in f_0 will become collisional particles and the UGKWP becomes a standard NS solver for the update $\mathbf{W}$ only.

The particle evolution follows the same integral solution of the kinetic model equation,

$$f(t,\mathbf{x},\mathbf{u},\boldsymbol{\xi}) = (1-e^{-t/\tau})M^+(t,\mathbf{x},\mathbf{u},\boldsymbol{\xi}) + e^{-t/\tau}f_0(\mathbf{x}-\mathbf{u}t,\mathbf{u},\boldsymbol{\xi}). \tag{4.7}$$

The above M^+ is named as the hydrodynamic distribution function with analytical formulation, i.e., the wave formulation of the gas distribution function. The initial particle distribution f_0 has a probability of $e^{-t/\tau}$ for free streaming and a probability of $(1-e^{-t/\tau})$ for colliding with other particles, and the post-collision distribution follows the distribution $M^+(t,\mathbf{x},\mathbf{u},\boldsymbol{\xi})$.

In a numerical time step from t^n to t^{n+1}, all simulating particles in UGKWP method can be categorized into two groups: the **collisionless particle** P^f and the **collisional particle** P^c. And all the particles will take free streaming for a period of t_k^f,

$$\mathbf{x}_k^* = \mathbf{x}_k^n + \mathbf{u}_k t_k^f. \tag{4.8}$$

The net free streaming flow of cell i within a time step Δt can be calculated by

counting all particles passing through the cell interface, which can be written as,

$$\mathbf{F}_i^{fr,p} = \sum_{k \in P_{\partial\Omega_i^+}} \mathbf{W}_{P_k} - \sum_{k \in P_{\partial\Omega_i^-}} \mathbf{W}_{P_k}. \tag{4.9}$$

The update of hydrodynamic flow variables originated from the eliminated particles are

$$\mathbf{W}_i^{n+1,h} = \mathbf{W}_i^{n+1} - \mathbf{W}_i^{n+1,p}, \tag{4.10}$$

where $\mathbf{W}_i^{n+1,p}$ is macroscopic flow variables of all remaining particles in the cell i, which can be evaluated by adding their mass, momentum, and energy together.

In UGKWP, the number of particles used in evolution depends on the cell Knudsen number $\mathrm{Kn}_c = \tau/\Delta t$ and takes a fraction of macroscopic variables $e^{-1/\mathrm{Kn}_c}\mathbf{W}$ inside each control volume. In the continuum flow regime with $\Delta t \gg \tau$, the particle will gradually disappear and the UGKWP will become a gas-kinteic scheme for the Navier-Stokes equations [63].

The above UGKWP is based on the single relaxation kinetic model. Even though the viscosity and heat conduction coefficients can be correctly defined through the Shakhov or Rykov models, all particles have the same relaxation time τ which is used in the determination of free steaming time of the particle in UGKWP.

In physical reality, the particle mean free path ℓ has a clear definition, such as the hard sphere model [40],

$$\ell = \frac{16}{5}\left(\frac{m}{2\pi k_B T}\right)^{1/2}\frac{\mu}{\rho}. \tag{4.11}$$

And the particle collision time is related to the particle relative velocity $|\mathbf{g}|$, such as $\ell/|\mathbf{g}|$.

In order to incorporate this physical reality, a direct modeling on the modification of particle transport in UGKWP is to get a more reliable particle collision time for those particles with a relative high velocity. The newly modeled relaxation

time $\tau^* = \tau^*(\mathbf{u})$ can depend on the particle velocity and has the form

$$\tau_* = \begin{cases} \tau & \text{if } |\mathbf{u} - \mathbf{U}| \leq 5\sigma \\ \frac{1}{1+0.1*|\mathbf{u}-\mathbf{U}|/\sigma}\tau & \text{if } |\mathbf{u} - \mathbf{U}| > 5\sigma \end{cases} \tag{4.12}$$

where $\sigma = \sqrt{RT}$ is the variance in Gaussian distribution.

For the particle, the free streaming time is determined by

$$t^f = \min(-\tau_* \ln(\eta), \Delta t). \tag{4.13}$$

For high speed particles, the relative collision time will be reduced according to the particle velocity. For other particles, the free steaming time remains the same, which has been taken into account properly by the kinetic relaxation model, such as recovering the viscosity and heat conduction coefficients.

The above modification of particle collision time will not affect the conservation of the scheme. For a specific particle, its mass, momentum, and energy will remain the same, and the only difference is about the distance it travels. The modification of particle free streaming time can be done directly in the UGKWP. For the DVM-based UGKS, it is very hard to modify the collision time at a particular particle velocity and keep the conservation.

However, compared with the Boltzmann equation (4.1), since we only model the relaxation time and left the equilibrium state M unchanged in Eq. (4.4). The compatibility condition (2.20) of collision term, which is mainly used to determine the spatial and time evolution of equilibriums states, is not fully satisfied in the UGKWP-τ^*, and its effect on the solution of rarefied flow is reduced significantly due to the absence of wave contribution.

All examples in the next section are computed with the above modified UGKWP-τ_*. The idea of τ_* modification in UGKWP has the physical similarity with the previous effort [117] of generalizing the Chapman-Enskog expansion for non-equilibrium flow study.

4.3 Numerical Results

In this section, the modified UGKWP will be tested in both 1D shock structure and 2D flow passing through cylinder case at different Mach and Knudsen numbers.

4.3.1 Nitrogen Gas Shock Structure

Since the 1950s, shock structure computation has played an essential role in validating kinetic theory and numerical schemes in non-equilibrium flow studies [118]. The internal structure of a normal shock wave is one of the simplest and most fundamental non-equilibrium gas dynamic phenomena that may be exploited for model validation. This is due to mostly two factors. First, the shock wave depicts a flow situation that is far from thermodynamic equilibrium. Second, shock wave phenomena is unique once the upstream and downstream are determined by the Rankine–Hugoniot relations, and it permits the separation of fluid dynamics from boundary condition.

In order to validate the flow physics from the newly modified UGKWP, the shock structures at different Mach numbers for diatomic gases will be calculated. The density and temperature distributions will be presented and compared with the reference solutions of DSMC.

In the following calculations, the viscous coefficient is given by,

$$\mu = \mu_{ref} \left(\frac{T}{T_0} \right)^{\omega}, \tag{4.14}$$

with the reference viscosity

$$\mu_{ref} = \frac{15\sqrt{\pi}}{2(5-2\omega)(7-2\omega)} \frac{\ell}{L}, \tag{4.15}$$

where L is the characteristic length, ω is the index for viscosity coefficient.

The diatomic gas UGKWP method is presented in Chapter 3. For diatomic gas, besides the translational relaxation, the rotational relaxation is included as well. The relaxation time between the rotational and translation energy exchange is determined by the rotational collision number Z_r. For the nitrogen gas, the viscous coefficient follows Eqs. (4.14) and (4.15) with the temperature dependent index $\omega = 0.74$.

In this calculation, the reference length is the upstream mean free path, and the computational domain is [-25,25] with 100 cells.The rotational collision number used in the UGKWP is $Z_r = 2.4$. The normalized temperature and density comparison between UGKWP and DSMC at Ma $= 1.53, 4.0, 5.0, 7.0$ are plotted in Fig. 4.1. With the modification of particle collision time, the UGKWP avoids the early temperature rising problem and presents good agreement with the DSMC result. In comparison with the Rykov model-based UGKS results [78], significant improvement has been observed.

4.3.2 Flow Passing a Circular Cylinder

In order to further validate the newly modified UGKWP method in the high speed rarefied flow regime, the flow of argon gas passing through a circular cylinder at different Mach numbers is calculated. Two Mach numbers Ma = 10 and 20 with the Knudsen number Kn = 0.1 will be tested. The Knudsen number is defined as the ratio of the mean free path over the cylinder radius.

The radius of the cylinder is given by $R = 0.01$m. For Ma = 10, the incoming argon gas has a velocity $U_\infty = 3077.587$m/s, the temperature $T_\infty = 273$K, molecular number density $n_\infty = 1.2944 \times 10^{21}/\text{m}^3$, and the reference viscosity $\mu_\infty = 2.117 \times 10^{-5}\text{N} \cdot \text{s/m}^2$. The viscosity is calculated by Eq. (4.14) with $\omega = 0.81$. The cylinder has constant surface temperature $T_w = 273K$, and diffusive boundary condition is adopted here. For Ma = 20, the only change is

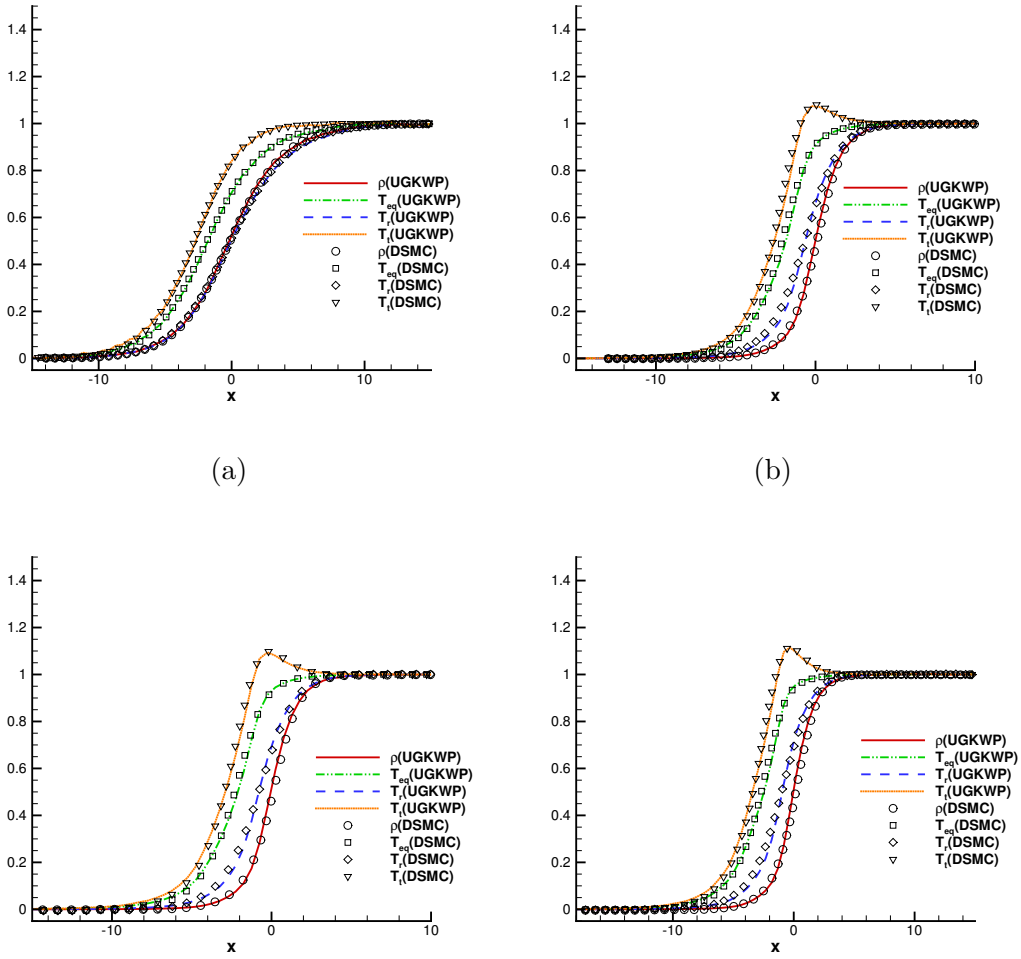

Figure 4.1: Comparison of UGKWP and DSMC results of nitrogen shock wave at different Mach numbers for nitrogen gas. (a)Ma = 1.53; (b)Ma = 4.0; (c)Ma = 5.0; (d)Ma = 7.0. The x-coordinate is normalized by ℓ. The symbols are DSMC results from Ref. [78].

the incoming velocity with a value of $U_\infty = 6155.174$m/s.

For both cases, the simulation results from UGKWP are compared the solutions of the DSMC and the UGKS-Shakhov [119]. For Ma = 10 case, Fig. 4.2 shows the density, x-velocity, and temperature along the central symmetric line in front of the stagnation point, where both UGKWP and UGKS-Shakhov solutions agree with the DSMC solutions, except that the temperature in UGKS-Shakhov solutions rises a little bit earlier. The comparison of the heat flux, shear stress, and pressure along the surface of the cylinder are shown in Fig. 4.3, which have good agreement with DSMC solution.

For Ma = 20 case, the results are plotted in Figs. 4.4 and 4.5. As shown in Fig. 4.4, the differences in temperature distributions from the UGKS-Shakhov and the DSMC are much more obvious than that in the Ma = 10 case, where the results from the modified UGKWP have good agreement with the DSMC solution, especially for the pressure and heat flux distributions along the surface of the cylinder.

4.4 Conclusion

In this chapter, a newly modified UGKWP method has been proposed for modeling and computation of non-equilibrium flow. The main idea is to adjust particle collision time according particle velocity, which is more consistent with the physical reality rather than the single relaxation kinetic model. The modeling in UGKWP is beyond the traditional BGK-type kinetic models.

With the implementation of particle velocity-dependent collision time, the non-equilibrium solution can be captured accurately, such as the shock structure calculations. Based on the simulation results, no obvious discrepancy between the UGKWP and DSMC results can be observed. Intrinsically, the DSMC colli-

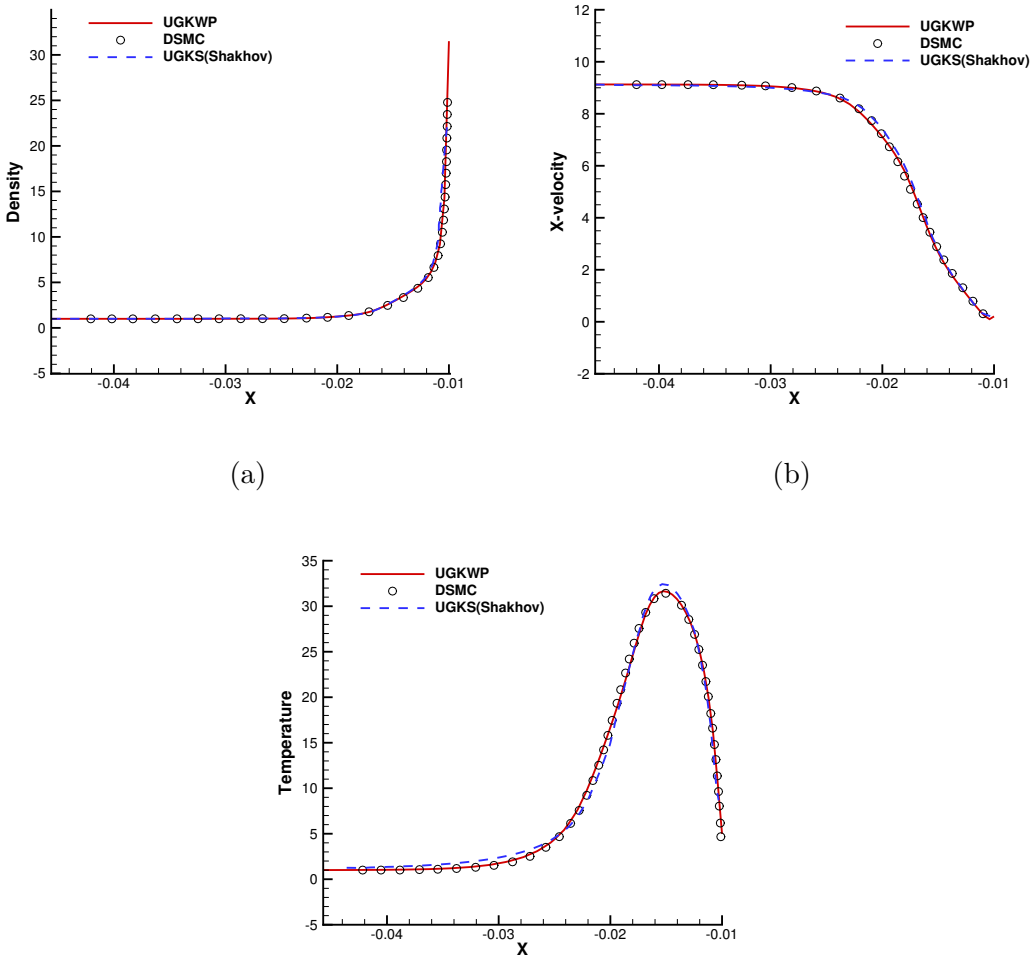

(a) (b)

(c)

Figure 4.2: Flow distributions for argon gas along the central symmetric line in front of the stagnation point at Ma = 10 and Kn = 0.1.

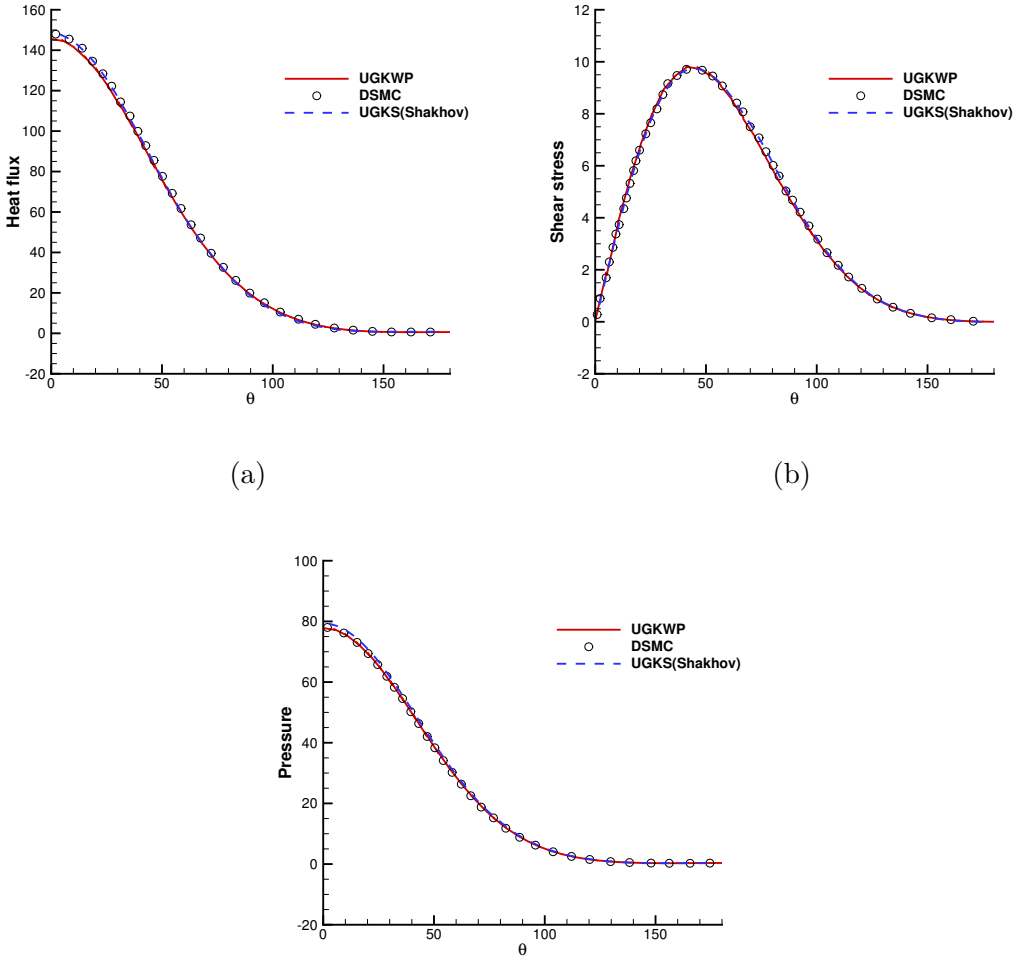

(a) (b)

(c)

Figure 4.3: Surface quantities along the surface of the cylinder for argon gas at Ma = 10 and Kn = 0.1.

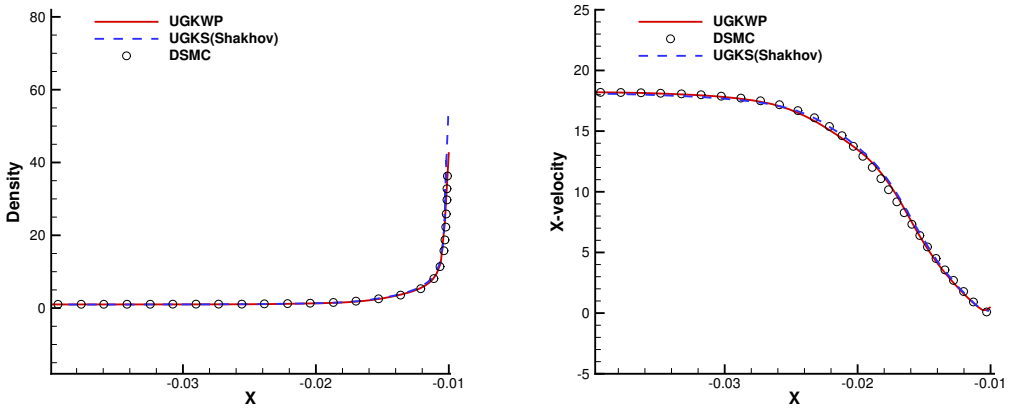

(a)

(b)

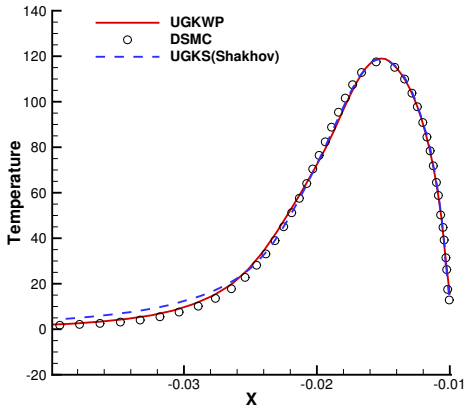

(c)

Figure 4.4: Flow distributions for argon gas along the central symmetric line in front of the stagnation point at Ma = 20 and Kn = 0.1.

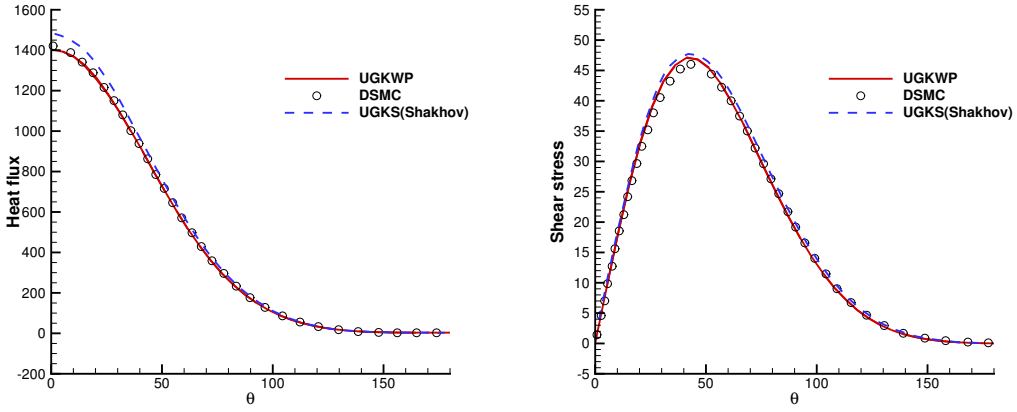

(a)

(b)

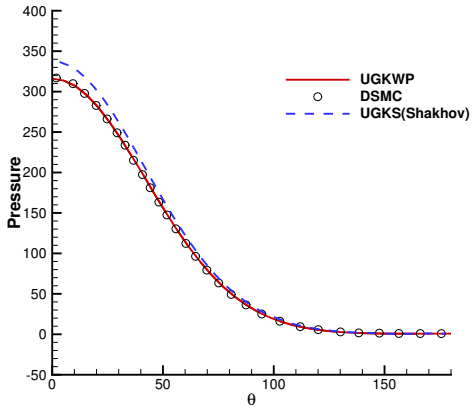

(c)

Figure 4.5: Surface quantities along the surface of the cylinder for argon gas at Ma = 20 and Kn = 0.1.

sion rate is determined by the relative particle velocity, which has the similarity with the modification of collision time according to particle velocity here. Since the dynamic effect from most particles around the average velocity has been taken into account in the kinetic relaxation model, only the collision time for these particles with extremely high speed needs to be modified.

Under such a modeling, the UGKWP method is still fully conservative. The only modification is the distance travelled by the very high speed particle. The additional work introduced in the modification of collision time doesn't increase any computational cost of UGKWP. In the continuum flow regime, the UGKWP will automatically recover the gas-kinetic scheme for the Navier-Stokes solutions with correct transport coefficients, while the distribution function has analytical Chapman-Enskog formulation. For the flow simulation with the co-existing multiple flow regimes, the UGKWP method can achieve high efficiency and present very accurate physical solution in all flow regimes.

Chapter 5

Conclusion and Future Work

5.1 Conclusion

This thesis concentrates on the construction and modeling of the unified gas-kinetic wave-particle method on three dimensional unstructured mesh for the simulation of monatomic and diatomic gas in all flow regimes.

The UGKWP solver is an outstanding multiscale solver, which is able to simulate the flow dynamics in all flow regimes with an efficient and unified approach. Based on the direct modeling principle, the gas distribution function in UGKWP is composed of discrete particle and wave instead of DVM approach in the UGKS. In the coupled evolution of particle and wave, an analytical expression can be obtained for the wave counterpart. At the same time, cell's Knudsen number-based weighting functions, i.e., $\exp(-\Delta t/\tau)$ and $(1-\exp(-\Delta t/\tau))$, are dynamically adapted to take account of the contributions from particle and wave in different regimes. As a result, the UGKWP becomes a particle method in the highly rarefied regime $\Delta t \leq \tau$, and gets back to a NS solver, i.e., the gas-kinetic scheme, in the continuum flow regime $\Delta t \gg \tau$. A seamless smooth transition between particle and hydrodynamic method is obtained in UGKWP. The UGKWP has

the unified preserving (UP) property to the NS solution in the continuum limit without restricting the cell size to be less than the particle mean free path.

The UGKWP has multiple efficiency preserving property for a multiscale flow problem, such as the simulation of hypersonic flow passing through a flying vehicle in near space flight with 5 to 6 orders of magnitude difference in the local Knudsen number. The calculation for a 3D problem at high speed and different Knudsen numbers can be conducted by UGKWP with a personal workstation.

In addition, the rotational mode of diatomic gas is built into the UGKWP with the adoption of Rykov relaxation model. Numerical tests from 1D shock structure to 3D hypersonic flow passing a sphere have been used to validate the capacity of UGKWP in capturing the non-equilibrium phenomena of energy exchange between transnational and rotational modes in different regimes. To further improve the accuracy of the current UGKWP in the rarefied regime, the single relaxation time of stochastic particle is modified physically according to particle velocity, especially for these particles with extremely higher velocity. This direct modification of particle collision time solves the early temperature rising problem in shock structure calculation, which exists in solutions from almost all single relaxation time kinetic model equations.

The development of UGKWP from a 2D to a 3D calculation needs great effort to solve all problems related to the complex geometry, reconstruction, multidimensional flux construction in its wave-particle decomposition, particle tracking, and parallelization. This thesis solves all these problems successfully and develops a 3D code in practical engineering applications.

5.2 Future Work

The future work will focus on the refinement, analysis, and extension of UGKWP method. On the one hand, the current UGKWP code can be further optimized to make it more efficient and comprehensive. It is expected that the dynamic load balancing implementation can enhance the parallel efficiency in rarefied regime considerably as in conventional DSMC implementation. Moreover, coalescing of small weight particles can also save the memory substantially in the rarefied regime. Besides, the improved sampling technique can be employed to moderate the noise for low-speed or small temperature variance simulations. The development of implicit UGKWP method is also attractive. Even in the continuum regime, once a small cell size is used, the corresponding time step Δt can become very small and a large weighting function $e^{-\Delta t/\tau}$ will still keep particles. The UGKWP may be further developed by using local time for the flow evolution.

On the other hand, rigorous analysis of the UGKWP method under unified preserving framework [38] would be an interesting topic. Investigation on the modeling of modified relaxation time τ_* can be further conducted. The emerging of machine learning might offer us useful tool for the determination of relaxation time τ_* and sampling particles from the equilibrium state M. Practical engineering simulations often encounter high speed and high temperature flow, which require further modeling of multiple species as well as other complex physical processes, such as vibration, ionization, and chemical reactions.

Bibliography

[1] J. Park, S. Baek, J. Kim, DSMC analysis of the interaction between thruster plume and satellite components, in: 40th AIAA Aerospace Sciences Meeting & Exhibit, 2002, p. 794.

[2] T. J. Scanlon, C. White, M. K. Borg, R. C. Palharini, E. Farbar, I. D. Boyd, J. M. Reese, R. E. Brown, Open-source direct simulation Monte Carlo chemistry modeling for hypersonic flows, AIAA journal 53 (6) (2015) 1670–1680.

[3] V. Kolobov, R. Arslanbekov, V. V. Aristov, A. Frolova, S. A. Zabelok, Unified solver for rarefied and continuum flows with adaptive mesh and algorithm refinement, Journal of Computational Physics 223 (2) (2007) 589–608.

[4] H.-S. Tsien, Superaerodynamics, mechanics of rarefied gases, Journal of the Aeronautical Sciences 13 (12) (1946) 653–664.

[5] S. Chapman, T. G. Cowling, D. Burnett, The mathematical theory of non-uniform gases: an account of the kinetic theory of viscosity, thermal conduction and diffusion in gases, Cambridge university press, 1990.

[6] D. Jiang, M. Mao, J. Li, X. Deng, An implicit parallel UGKS solver for flows covering various regimes, Advances in Aerodynamics 1 (1) (2019) 8.

[7] H. Grad, On the kinetic theory of rarefied gases, Communications on pure and applied mathematics 2 (4) (1949) 331–407.

[8] H. Struchtrup, M. Torrilhon, Regularization of Grad's 13 moment equations: Derivation and linear analysis, Physics of Fluids 15 (9) (2003) 2668–2680.

[9] R. Myong, A generalized hydrodynamic computational model for rarefied and microscale diatomic gas flows, Journal of Computational Physics 195 (2) (2004) 655–676.

[10] C. Chu, Kinetic-theoretic description of the formation of a shock wave, The Physics of Fluids 8 (1) (1965) 12–22.

[11] J. Yang, J.-c. Huang, Rarefied flow computations using nonlinear model Boltzmann equations, Journal of Computational Physics 120 (2) (1995) 323–339.

[12] L. Mieussens, Discrete-velocity models and numerical schemes for the Boltzmann-BGK equation in plane and axisymmetric geometries, Journal of Computational Physics 162 (2) (2000) 429–466.

[13] F. Tcheremissine, Direct numerical solution of the Boltzmann equation, Tech. rep., DTIC Document (2005).

[14] V. Kolobov, R. Arslanbekov, V. Aristov, A. Frolova, S. Zabelok, Unified solver for rarefied and continuum flows with adaptive mesh and algorithm refinement, J. Comput. Phys. 223 (2) (2007) 589–608.

[15] Z.-H. Li, H.-X. Zhang, Gas-kinetic numerical studies of three-dimensional complex flows on spacecraft re-entry, Journal of Computational Physics 228 (4) (2009) 1116–1138.

[16] K. Xu, J.-C. Huang, A unified gas-kinetic scheme for continuum and rarefied flows, Journal of Computational Physics 229 (20) (2010) 7747–7764.

[17] V. V. Aristov, Direct methods for solving the Boltzmann equation and study of nonequilibrium flows, Vol. 60, Springer Science & Business Media, 2012.

[18] T. Xiong, G. Russo, J.-M. Qiu, Conservative multi-dimensional semi-Lagrangian finite difference scheme: stability and applications to the kinetic and fluid simulations, Journal of Scientific Computing 79 (2) (2019) 1241–1270.

[19] S. Y. Cho, S. Boscarino, G. Russo, S.-B. Yun, Conservative semi-Lagrangian schemes for kinetic equations Part II: Applications, Journal of Computational Physics 436 (2021) 110281.

[20] B. Dubroca, L. Mieussens, A conservative and entropic discrete-velocity model for rarefied polyatomic gases, in: ESAIM: Proceedings, Vol. 10, EDP Sciences, 2001, pp. 127–139.

[21] R. Chen, R. Agarwal, F. Tcheremissine, Computation of hypersonic flow of a diatomic gas in rotational nonequilibrium past a blunt body using the generalized Boltzmann equation, in: AIP Conference Proceedings, Vol. 1084, American Institute of Physics, 2008, pp. 476–482.

[22] G. Dimarco, L. Pareschi, Numerical methods for kinetic equations, Acta Numerica 23 (2014) 369–520.

[23] L. Wu, J. Zhang, J. M. Reese, Y. Zhang, A fast spectral method for the Boltzmann equation for monatomic gas mixtures, Journal of Computational Physics 298 (2015) 602–621.

[24] V. Titarev, M. Dumbser, S. Utyuzhnikov, Construction and comparison of parallel implicit kinetic solvers in three spatial dimensions, Journal of Computational Physics 256 (2014) 17–33.

[25] Z. Guo, K. Xu, R. Wang, Discrete unified gas kinetic scheme for all Knudsen number flows: Low-speed isothermal case, Physical Review E 88 (3) (2013) 033305.

[26] Z. Guo, R. Wang, K. Xu, Discrete unified gas kinetic scheme for all Knudsen number flows. II. Thermal compressible case, Physical Review E 91 (3) (2015) 033313.

[27] Y. Zhu, C. Zhong, K. Xu, Unified gas-kinetic scheme with multigrid convergence for rarefied flow study, Physics of Fluids 29 (9) (2017) 096102.

[28] Y. Zhu, C. Zhong, K. Xu, An implicit unified gas-kinetic scheme for unsteady flow in all Knudsen regimes, Journal of Computational Physics 386 (2019) 190–217.

[29] Z.-H. Li, A.-P. Peng, Q. Ma, L.-N. Dang, X.-W. Tang, X.-Z. Sun, Gas-kinetic unified algorithm for computable modeling of Boltzmann equation and application to aerothermodynamics for falling disintegration of uncontrolled Tiangong-no. 1 spacecraft, Advances in Aerodynamics 1 (1) (2019) 1–21.

[30] W. Su, L. Zhu, P. Wang, Y. Zhang, L. Wu, Can we find steady-state solutions to multiscale rarefied gas flows within dozens of iterations?, Journal of Computational Physics 407 (2020) 109245.

[31] P. L. Bhatnagar, E. P. Gross, M. Krook, A model for collision processes in gases. I. Small amplitude processes in charged and neutral one-component systems, Physical review 94 (3) (1954) 511.

[32] L. H. Holway Jr, New statistical models for kinetic theory: methods of construction, The physics of fluids 9 (9) (1966) 1658–1673.

[33] E. Shakhov, Generalization of the Krook kinetic relaxation equation, Fluid dynamics 3 (5) (1968) 95–96.

[34] L. Zhu, S. Chen, Z. Guo, dugksFoam: An open source OpenFOAM solver for the Boltzmann model equation, Computer Physics Communications 213 (2017) 155–164.

[35] K. Xu, Direct modeling for computational fluid dynamics: construction and application of unified gas-kinetic schemes, Vol. 4, World Scientific, 2014.

[36] S. Jin, Efficient asymptotic-preserving (AP) schemes for some multiscale kinetic equations, SIAM Journal on Scientific Computing 21 (2) (1999) 441–454.

[37] Z. Guo, J. Li, K. Xu, On unified preserving properties of kinetic schemes, arXiv preprint arXiv:1909.04923 (2019).

[38] Z. Guo, J. Li, K. Xu, On unified preserving properties of kinetic schemes, arXiv:1909.04923v6 [math.NA] (2021).

[39] G. Bird, Approach to translational equilibrium in a rigid sphere gas, The Physics of Fluids 6 (10) (1963) 1518–1519.

[40] G. A. Bird, J. Brady, Molecular gas dynamics and the direct simulation of gas flows, Vol. 5, Clarendon press Oxford, 1994.

[41] M. Pfeiffer, P. Nizenkov, A. Mirza, S. Fasoulas, Direct simulation Monte Carlo modeling of relaxation processes in polyatomic gases, Physics of Fluids 28 (2) (2016) 027103.

[42] S. Stefanov, On the basic concepts of the direct simulation Monte Carlo method, Physics of Fluids 31 (6) (2019) 067104.

[43] L. Pareschi, G. Russo, Asymptotic preserving Monte Carlo methods for the Boltzmann equation, Transport Theory and Statistical Physics 29 (3-5) (2000) 415–430.

[44] W. Ren, H. Liu, S. Jin, An asymptotic-preserving Monte Carlo method for the Boltzmann equation, Journal of Computational Physics 276 (2014) 380–404.

[45] G. Dimarco, L. Pareschi, G. Samaey, Asymptotic-preserving Monte Carlo methods for transport equations in the diffusive limit, SIAM Journal on Scientific Computing 40 (1) (2018) A504–A528.

[46] J. Fan, C. Shen, Statistical simulation of low-speed rarefied gas flows, Journal of Computational Physics 167 (2) (2001) 393–412.

[47] T. M. Homolle, N. G. Hadjiconstantinou, A low-variance deviational simulation Monte Carlo for the Boltzmann equation, Journal of Computational Physics 226 (2) (2007) 2341–2358.

[48] P. Degond, G. Dimarco, L. Pareschi, The moment-guided Monte Carlo method, International Journal for Numerical Methods in Fluids 67 (2) (2011) 189–213.

[49] M. Gallis, J. Torczynski, The application of the BGK model in particle simulations, in: 34th Thermophysics Conference, 2000, p. 2360.

[50] F. Fei, J. Zhang, J. Li, Z. Liu, A unified stochastic particle Bhatnagar-Gross-Krook method for multiscale gas flows, Journal of Computational Physics 400 (2020) 108972.

[51] O. Tumuklu, Z. Li, D. A. Levin, Particle ellipsoidal statistical Bhatnagar–Gross–Krook approach for simulation of hypersonic shocks, AIAA journal 54 (12) (2016) 3701–3716.

[52] P. Jenny, M. Torrilhon, S. Heinz, A solution algorithm for the fluid dynamic equations based on a stochastic model for molecular motion, Journal of computational physics 229 (4) (2010) 1077–1098.

[53] M. H. Gorji, M. Torrilhon, P. Jenny, Fokker–Planck model for computational studies of monatomic rarefied gas flows, Journal of fluid mechanics 680 (2011) 574–601.

[54] M. A. Gallis, Stochastic PArallel Rarefied-gas Time-accurate Analyzer., Tech. rep., Sandia National Lab.(SNL-NM), Albuquerque, NM (United States) (2015).

[55] T. Scanlon, E. Roohi, C. White, M. Darbandi, J. Reese, An open source, parallel DSMC code for rarefied gas flows in arbitrary geometries, Computers & Fluids 39 (10) (2010) 2078–2089.

[56] C. White, M. K. Borg, T. J. Scanlon, S. M. Longshaw, B. John, D. Emerson, J. M. Reese, dsmcFoam+: An OpenFOAM based direct simulation Monte Carlo solver, Computer Physics Communications 224 (2018) 22–43.

[57] H. G. Weller, G. Tabor, H. Jasak, C. Fureby, A tensorial approach to computational continuum mechanics using object-oriented techniques, Computers in physics 12 (6) (1998) 620–631.

[58] C. J. Greenshields, OpenFOAM - The Open Source CFD Toolbox-User Guide, OpenFOAM Foundation Ltd 2 (0) (2015).

[59] The OpenFOAM Foundation, Openfoam, [Online; accessed 12-January-2020] (2020).
URL `https://openfoam.org/`

[60] S. Dietrich, I. D. Boyd, Scalar and parallel optimized implementation of the direct simulation Monte Carlo method, Journal of Computational Physics 126 (2) (1996) 328–342.

[61] M. Ivanov, G. Markelov, S. Gimelshein, Statistical simulation of reactive rarefied flows-numerical approach and applications, in: 7th AIAA/ASME Joint Thermophysics and Heat Transfer Conference, 1998, p. 2669.

[62] G. LeBeau, A parallel implementation of the direct simulation Monte Carlo method, Computer methods in applied mechanics and engineering 174 (3-4) (1999) 319–337.

[63] K. Xu, A gas-kinetic BGK scheme for the Navier–Stokes equations and its connection with artificial dissipation and Godunov method, Journal of Computational Physics 171 (1) (2001) 289–335.

[64] Q. Sun, I. D. Boyd, G. V. Candler, A hybrid continuum/particle approach for modeling subsonic, rarefied gas flows, Journal of Computational Physics 194 (1) (2004) 256–277.

[65] T. E. Schwartzentruber, I. D. Boyd, A hybrid particle-continuum method applied to shock waves, Journal of Computational Physics 215 (2) (2006) 402–416.

[66] P. Degond, G. Dimarco, L. Mieussens, A multiscale kinetic–fluid solver with dynamic localization of kinetic effects, Journal of Computational Physics 229 (13) (2010) 4907–4933.

[67] F. Filbet, T. Rey, A hierarchy of hybrid numerical methods for multiscale kinetic equations, SIAM Journal on Scientific Computing 37 (3) (2015) A1218–A1247.

[68] J.-C. Huang, K. Xu, P. Yu, A unified gas-kinetic scheme for continuum and rarefied flows II: multi-dimensional cases, Communications in Computational Physics 12 (3) (2012) 662–690.

[69] C. Liu, K. Xu, Q. Sun, Q. Cai, A unified gas-kinetic scheme for continuum and rarefied flows IV: Full Boltzmann and model equations, Journal of Computational Physics 314 (2016) 305–340.

[70] W. Sun, S. Jiang, K. Xu, S. Li, An asymptotic preserving unified gas kinetic scheme for frequency-dependent radiative transfer equations, Journal of Computational Physics 302 (2015) 222–238.

[71] T. Shuang, S. Wenjun, W. Junxia, N. Guoxi, A parallel unified gas kinetic scheme for three-dimensional multi-group neutron transport, Journal of Computational Physics 391 (2019) 37–58.

[72] S. Tan, W. Sun, K. Xu, J. Wei, G. Ni, Time Implicit Unified Gas Kinetic Scheme for 3D Multi-Group Neutron Transport Simulation, Communications in Computational Physics 28 (3) (2020) 1189–1218.

[73] C. Liu, Z. Wang, K. Xu, A unified gas-kinetic scheme for continuum and rarefied flows VI: Dilute disperse gas-particle multiphase system, Journal of Computational Physics 386 (2019) 264–295.

[74] T. Xiao, K. Xu, Q. Cai, A unified gas-kinetic scheme for multiscale and multicomponent flow transport, Applied Mathematics and Mechanics 40 (3) (2019) 355–372.

[75] Z. Wang, H. Yan, Unified gas-kinetic scheme for the monodisperse gas-particle flow and its application in the shock-driven multiphase instability, International Journal of Multiphase Flow 119 (2019) 95–107.

[76] C. Liu, K. Xu, A unified gas kinetic scheme for continuum and rarefied flows V: multiscale and multi-component plasma transport, Communications in Computational Physics 22 (5) (2017) 1175–1223.

[77] D. Pan, C. Zhong, C. Zhuo, W. Tan, A unified gas kinetic scheme for transport and collision effects in plasma, Applied Sciences 8 (5) (2018) 746.

[78] S. Liu, P. Yu, K. Xu, C. Zhong, Unified gas-kinetic scheme for diatomic molecular simulations in all flow regimes, Journal of Computational Physics 259 (2014) 96–113.

[79] Z. Wang, H. Yan, Q. Li, K. Xu, Unified gas-kinetic scheme for diatomic molecular flow with translational, rotational, and vibrational modes, Journal of Computational Physics 350 (2017) 237–259.

[80] S. Chen, K. Xu, C. Lee, Q. Cai, A unified gas kinetic scheme with moving mesh and velocity space adaptation, Journal of Computational Physics 231 (20) (2012) 6643–6664.

[81] J. Chen, S. Liu, Y. Wang, C. Zhong, Conserved discrete unified gas-kinetic scheme with unstructured discrete velocity space, Physical Review E 100 (4) (2019) 043305.

[82] S. Chen, C. Zhang, L. Zhu, Z. Guo, A unified implicit scheme for kinetic model equations. Part I. Memory reduction technique, Science bulletin 62 (2) (2017) 119–129.

[83] L. Yang, C. Shu, W. Yang, J. Wu, An implicit scheme with memory reduction technique for steady state solutions of DVBE in all flow regimes, Physics of Fluids 30 (4) (2018) 040901.

[84] Y. Zhu, C. Zhong, K. Xu, Implicit unified gas-kinetic scheme for steady state solutions in all flow regimes, Journal of Computational Physics 315 (2016) 16–38.

[85] Y. Zhu, C. Zhong, K. Xu, Unified gas-kinetic scheme with multigrid convergence for rarefied flow study, Physics of Fluids 29 (9) (2017) 096102.

[86] Y. Zhu, C. Zhong, K. Xu, An Implicit Unified Gas-kinetic Scheme for Unsteady Flow in All Knudsen Regimes, arXiv preprint arXiv:1801.02022 (2018).

[87] Y. Zhu, C. Zhong, K. Xu, GKS and UGKS for High-Speed Flows, Aerospace 8 (5) (2021) 141.

[88] C. Liu, Y. Zhu, K. Xu, Unified gas-kinetic wave-particle methods I: Continuum and rarefied gas flow, Journal of Computational Physics 401 (2020) 108977.

[89] Y. Zhu, C. Liu, C. Zhong, K. Xu, Unified gas-kinetic wave-particle methods. II. Multiscale simulation on unstructured mesh, Physics of Fluids 31 (6) (2019) 067105.

[90] X. Xu, Y. Chen, C. Liu, Z. Li, K. Xu, Unified gas-kinetic wave-particle methods V: diatomic molecular flow, Journal of Computational Physics 442 (2021) 110496.

[91] W. Li, C. Liu, Y. Zhu, J. Zhang, K. Xu, Unified gas-kinetic wave-particle methods iii: Multiscale photon transport, Journal of Computational Physics 408 (2020) 109280.

[92] C. Liu, K. Xu, Unified gas-kinetic wave-particle methods IV: Multi-species Gas Mixture and Plasma Transport, arXiv:2009.06261 (2020).

[93] Y. Zhu, C. Zhong, K. Xu, Ray Effect in Rarefied Flow Simulation, Journal of Computational Physics (2020) 109751.

[94] C. Cercignani, The Boltzmann equation and its applications, in: The Boltzmann equation and its applications, Springer, 1988, pp. 40–103.

[95] I. D. Boyd, T. E. Schwartzentruber, Nonequilibrium Gas Dynamics and Molecular Simulation, Vol. 42, Cambridge University Press, 2017.

[96] L. Holway, Kinetic theory of shock structure using an ellipsoidal distribution function, Rarefied gas dynamics 1 (1966) 193–215.

[97] K. Koura, H. Matsumoto, Variable soft sphere molecular model for inverse-power-law or Lennard-Jones potential, Physics of fluids A: fluid dynamics 3 (10) (1991) 2459–2465.

[98] V. Venkatakrishnan, Convergence to steady state solutions of the Euler equations on unstructured grids with limiters, Journal of computational physics 118 (1) (1995) 120–130.

[99] T. Barth, D. Jespersen, The design and application of upwind schemes on unstructured meshes, in: 27th Aerospace sciences meeting, 1989, p. 366.

[100] P. Vijayan, Y. Kallinderis, A 3D finite-volume scheme for the Euler equations on adaptive tetrahedral grids, Journal of Computational Physics 113 (2) (1994) 249–267.

[101] G. Marsaglia, T. A. Bray, A convenient method for generating normal variables, SIAM review 6 (3) (1964) 260–264.

[102] R. E. Caflisch, et al., Monte Carlo and quasi-Monte Carlo methods, Acta numerica 1998 (1998) 1–49.

[103] K. H. Prendergast, K. Xu, Numerical hydrodynamics from gas-kinetic theory, Journal of Computational Physics 109 (1) (1993) 53–66.

[104] L. L. Baker, N. G. Hadjiconstantinou, Variance reduction for Monte Carlo solutions of the Boltzmann equation, Physics of Fluids 17 (5) (2005) 051703.

[105] L. Zhu, P. Wang, S. Chen, Z. Guo, Y. Zhang, GPU acceleration of an iterative scheme for gas-kinetic model equations with memory reduction techniques, Computer Physics Communications 245 (2019) 106861.

[106] K. Xu, J.-C. Huang, An improved unified gas-kinetic scheme and the study of shock structures, IMA Journal of Applied Mathematics 76 (5) (2011) 698–711.

[107] A. J. Lofthouse, L. C. Scalabrin, I. D. Boyd, Velocity slip and temperature jump in hypersonic aerothermodynamics, Journal of thermophysics and heat transfer 22 (1) (2008) 38–49.

[108] C. Shen, Rarefied gas dynamics: fundamentals, simulations and micro flows, Springer Science & Business Media, 2006.

[109] V. Rykov, A model kinetic equation for a gas with rotational degrees of freedom, Fluid Dynamics 10 (6) (1975) 959–966.

[110] L. Wu, C. White, T. J. Scanlon, J. M. Reese, Y. Zhang, A kinetic model of the Boltzmann equation for non-vibrating polyatomic gases, Journal of Fluid Mechanics 763 (2015) 24–50.

[111] C. W. Chang, G. Uhlenbeck, Transport phenomena in polyatomic molecules, CM-681 (University of Michigan, 1951) (1951).

[112] V. Rykov, V. Skobelkin, Macroscopic description of the motions of a gas with rotational degrees of freedom, Fluid Dynamics 13 (1) (1978) 144–147.

[113] K. Xu, X. He, C. Cai, Multiple temperature kinetic model and gas-kinetic method for hypersonic non-equilibrium flow computations, Journal of computational physics 227 (14) (2008) 6779–6794.

[114] G. May, B. Srinivasan, A. Jameson, An improved gas-kinetic BGK finite-volume method for three-dimensional transonic flow, Journal of Computational Physics 220 (2) (2007) 856–878.

[115] N. Tsuboi, Y. Matsumoto, Experimental and numerical study of hypersonic rarefied gas flow over flat plates, AIAA journal 43 (6) (2005) 1243–1255.

[116] W. JF, Drag Coefficients of Spheres in Hypersonic Non-Continuum Flow, Tech. Rep. AD739250, von Karman Institute for Fluid Dynamics (1971).

[117] K. Xu, Regularization of the Chapman–Enskog expansion and its description of shock structure, Physics of Fluids 14 (4) (2002) L17–L20.

[118] G. Bird, Aspects of the structure of strong shock waves, The Physics of Fluids 13 (5) (1970) 1172–1177.

[119] P.-b. Yu, A unified gas kinetic scheme for all Knudsen number flows, Ph.D., The Hong Kong University of Science and Technology, Clear Water Bay, Kowloon, Hong Kong, pages: b1251528 (2013). doi:10.14711/thesis-b1251528.
URL http://lbezone.ust.hk/bib/b1251528